Symmetrybreaking

Aarøe, Morten

Publication date:
2009

Document Version
Early version, also known as pre-print

Symmetrybreaking
in superconducting phase transitions

Ph.D dissertation at DTU Physics

April 1st 2009

Nano•DTU
Center for Nanoteknologi på DTU

Morten Aarøe

Symmetry breaking in phase transitions

Abstract

It was predicted by Kibble and Zurek, that fast phase transitions in systems with degenerate ground states would produce topological defects. Although their work was initially focused on cosmological phase transitions, it was soon realized, that solid-state analogues existed. This opened the possibility of creating solid-state experiments and get results applicable to cosmological phase transitions.

While different groups with several different approaches have tried to experimentally verify the critical scaling behavior of topological defect production in solid-state systems, the results have been far from convincing. In this project, the focus has been on designing, producing and using experimental setups focused on defect production in solid state systems. The system of choice is the annular Josephson junction, but the single superconducting ring has been used as an analogue as well.

The results from the annular Josephson junction confirms critical scaling behavior of the probability of producing single fluxons with quench time, τ_Q. The critical exponent found is $\sigma_{AJTJ} = 0.5 \pm 5\%$. No scaling results have yet been obtained from the single superconducting ring experiments, but initial tests are promising.

In addition to testing Kibble-Zurek theory, a major part of the project has been dedicated to measuring and modeling Josephson junctions of various geometries in out-of-plane fields. It was shown, that by careful design, the sensitivity of junctions to magnetic field direction could be modified. A theoretical model was found to explain this behavior, which was verified by experiments.

Dansk resumé

Kibble og Zurek forudsagde, at hurtige faseovergange i systemer med degenererede grundtilstande, ville resultere i en produktion af topologiske defekter. Selv om deres tidlige arbejde var fokuseret på kosmologiske faseovergange, blev det hurtig klart, at faststoffysiske analoger kunne findes. Dette skabte mulighed for at lave faststoffysiske eksperimenter og fortolke deres resultater i en kosmologisk kontekst.

Selv om forskellige grupper med diverse forskellige systemer har prøvet at eftervise Kibble og Zureks ideer eksperimentelt, har det vist sig meget svært at demonstrere kritisk skalering af antallet af defekter i faststofsystemer, og de hidtidige resultater har været langt fra overbevisende. Dette projekt har været fokuseret på at designe, producere og bruge eksperimentelle metoder og opstillinger til at måle defekt produktion i faststofsystemer. Det mest anvendte system har været den annulære Josephson diode, men den isolerede superledende ring er også blevet brugt som analog til de kosmologiske systemer.

Resultaterne fra de annulære Josephson dioder efterviser, at sandsynligheden for at producere enkelte fluxoner skalerer nedkølingstiden, τ_Q. Den kritiske eksponent blev målt til at være $\sigma_{AJTJ} = 0.5 \pm 5\%$. Ingen troværdige Kibble-Zurek eksperimenter er indtil videre blevet gjort på opstillingerne, der indvolverer isolerede superledende ringe, men resultaterne af de indledende tests virker lovende.

Ud over at efterprøve Kibble-Zurek teorien er en stor del af projektet brugt på at måle og modellere Josephson dioder af forskellig geometri i magnetiske felter. Det blev vist, at man ved gennemtænkt design af diode- og elektrode-geometrien kan producere dioder med vidt forskellig følsomhed over for retningen af det påtrykte magnetiske felt. En teoretisk model blev opstillet, der forklarede disse resultater, og modellens forudsigelser blev eftervist eksperimentelt.

Thanks and acknowledgements

Here I would like to thank, in random order, people who have helped make this project possible, easier, more fun - or all of the above. As always, the workshop never ceases to amaze me in their ability to produce the strangest contraptions to extreme precision. Without their effort, very little of the projects in this group would be possible. Similarly, our resident fix-it-all electronics genius Birger seems to be the last person alive, who can fix our magnificent analogue electronics equipment when it breaks down - within days if not hours. Mogens Samuelsen deserves credit for being the one person you can go to with a theoretical problem and expect to leave with it solved, if not by him directly, then by some form of telepathy. Conny Hougaard from DTU Danchip should also be thanked for trying to teach me laboratory manners and tricks in the cleanroom. My project supervisor, Jesper Mygind, deserves a special thanks for being a guide more than a boss and for many stimulating discussions - even if it resulted in days of thinking and modeling to prove one of us wrong. I have also enjoyed many, many hours working with Prof. Roberto Monaco in the laboratory and exchanging ideas. Similarly, the effort of a single theorist in a group of experimentalists should not go unappreciated. Thank you to Prof. Ray Rivers from Imperial College for sharing his insight in the theory and for being one of the few theorists who sincerely attempts to close the gap between theorists and experimentalists.

The lunch-club also deserves thanks for being a place to exchange food and ideas in random order and fashion. The other students in my group have also been a positive influence as we have all learned, that the fastest way to improve something is to have someone else take it apart - with a screwdriver or a comment in the lab. Especially Mads, with whom I have shared many discussions, superconducting samples and pool-games, was a positive influence in the group. Jonathan Silman from Israel was a guest in the group for some months and deserves much credit for starting some theoretical thinking. Likewise from Israel, Prof. Jakob Levitan always contributed much positive energy and enthusiasm, and is still working for a closer cooperation with DTU Physics. Prof. Marcus Aspelmeyer visited DTU and showed us completely new implications and applications of microcantilevers and optics, and inspired my to part of the optical setup designed for the single ring experiment.

Finally, my girlfriend Signe, without whom this project might have been completed faster, but left myself much less interesting. She is my top reason for smiling - and for leaving the lab early.

Contents

Foreword

This work was performed at DTU Physics at the Technical University of Denmark (DTU) in Lyngby, Denmark. This dissertation is part of the required work to obtain a ph.d degree. The supervisor of the project is Dr. Jesper Mygind of DTU Physics. Major parts of the work was performed in collaboration with Prof. Roberto Monaco of the University of Salerno, Dr. Ray Rivers of Imperial College in London and Dr. Valery Koshelets of the Institute of Radio Engineering and Electronics (IREE) in Moscow. The project was fully financed by a DTU ph.d stipend awarded to the author in 2006.

In the beginning of the project our main goal was to finish the polishing of an existing annular Josephson junction setup, designed with Kibble-Zurek measurements in mind. However, a number of problems were discovered with magnetic pollution in the sample holder, so we decided to built a new, improved sample holder from scratch. This also significantly increased the ease-of-use of the experimental setup in terms of sample management and preparation. Another important work was to create a fully automated system for running the experiment without user-intervention and analyzing the results.

It was always the end goal of the project to pursue a new experimental setup, capable of detecting Kibble-Zurek defect production in a different system. To meet this goal, we started design work on the simple superconducting ring experiment. It ended up involving a lot of technology work, both by integrating processes from different microfabrication cleanrooms, and process development for producing the very soft cantilevers needed for the experiment. Although we have not yet managed to get to the point of running Kibble-Zurek experiments on the microcantilever setup, a spin-off of this project, using the same samples have already proven its ability to detect Kibble-Zurek defect production.

This dissertation is divided into several chapters. In the Introduction, I will try to set the stage for using solid-state experiments as cosmological analogues. In the Theory chapter, a quick introduction to the theory of Kibble-Zurek defect production will be given, as well as the developed theory for defect production in systems with pre-broken symmetry. The theoretical parts of the work on Josephson junctions in oblique fields can also be found here, as well as a simple description of the field-reduction seen in a solenoid enclosed in a superconducting shield. In the chapter Experimental methods, the experimental background for the project is described. Both the procedures used for measurements, and the limitations of the experimental setup is discussed in this chapter. In the Results chapter, the main results of the project are shown before being evaluated in the Discussion chapter. Finally concluding remarks and outlook on possible further experiments are given in the Conclusion.

In the appendices technical details on the equipment and software is given, along with any detailed derivations that was found too big to include in the text itself.

When figures have been published elsewhere, a citation is given to the appropriate journal paper.

1 Introduction

Most of our knowledge about the Universe beyond our own planet is obtained through the study of radiation from far objects. This is only possible as far as the Universe is transparent in some path of the radiation between the object and the detector. Therefore the fact, that the Universe remained opaque until it reached an age of approximately 300.000 years, severely limits the knowledge of the early Universe. The problem is important, as the seeds to galaxy formation, and maybe indeed the fundamental forces, was created before the Universe became transparent[1]. The only source of information about what happened before this time is the state of the observable Universe. Therefore, stable objects that could have survived from before the transition are of great importance to the understanding of the early Universe. One class of objects, that should be both observable and be stable enough to last into the transparent phase of the Universe, are so-called topological defects. They are extremely stable objects, as they are created as a result of a phase transition at an earlier time, where the Universe was warmer, and cannot be destroyed unless by heating to the same temperature or mutual annihilation. An artists view of the history of the Universe can be seen in Fig. 1.1[2].

The fundamental problem is how something, that started out in a very symmetric, homogeneous state, ended up in a quite heterogeneous and symmetry-broken state - without external symmetry-breaking influences. This problem assumes that (a)the Universe was maximally sym-

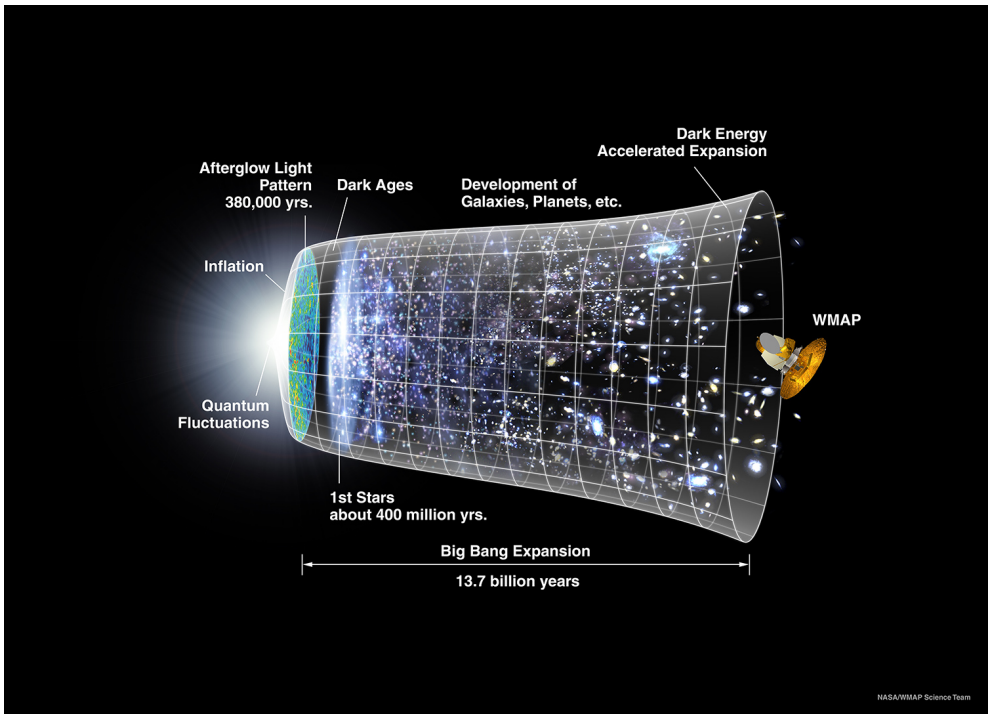

Figure 1.1: Artists view of the history of the Universe. Reproduced from NASA WMAP website with permission.

metric at the birth of the Universe/The Big Bang, and (b) that the Universe is an isolated system in which no external influences play a role. The very fact that galaxies exist is evidence of a broken symmetry, when compared to the homogeneous distribution of matter assumed just after The Big Bang. Other examples are the cosmic microwave anisotropy and the apparent asymmetry between matter and anti-matter in the visible Universe.

In a pioneering paper, Kibble proposed[1, 3] a simple method for estimating the production of topological defects in the early Universe. The applied model was so universal, that Zurek later[4, 5] applied it to different solid-state systems with little modification, thus establishing an analogy between the early Universe and the physics of solid-state systems. In principle, this provides the coupling to allow using experiments on solid-state systems to estimate topological defect production in the early Universe. As such, the obtained results can be used to falsify theories on the physics of the early Universe by providing an indication of how many and which type of defects should be visible through observation.

Later several groups performed experiments on defect production in various solid-state systems after fast quenches(rapid cooling). The initial experiments were on liquid crystals[6] and He^4[7, 8] with varying results. Experiments have also been done on high-T_c YBCO films[9], arrays of low-T_c superconducting rings[10] and superfluid He^3[11, 12]. The combined results of these have been somewhat confusing and sometimes self-contradictory owing to particular details of the systems, lack of available quench times or a physical problems with the setup. In none of these cases have robust Kibble-Zurek scaling been shown. For a review see [13].

During that time, experiments were done at DTU Physics (then the Department of Physics at DTU) in collaboration with the University of Salerno, on measuring Josephson fluxon dynamics. One of the main experimental difficulties of studying the dynamics of Josephson fluxons were to create them and afterwards keep them from disappearing before experiments could be done. The last problem was solved by using annular Josephson junctions, in which there is no ends for the fluxon to disappear through. The study of the first problem became the start of the group's entry into Kibble-Zurek research.

Later, in the beginning of this Ph.D project, the design of alternate experimental setups started. They were meant for testing the Kibble-Zurek scenario in a different setting, thus demonstrating its universality. The demonstration of Kibble-Zurek defect production in another system would also be a strong support of both the findings of the first experimental setup, and the theory as a whole. The most obvious choice, given the experience of the group, was to look at simple superconducting rings. The second half of this project was dedicated to planning, designing and producing the necessary equipment for Kibble-Zurek measurements on isolated superconducting rings.

During the project, it was realized, that the systems' dependence on the direction magnetic field was also very important. Therefore an excursion into the realm of Josephson junctions in oblique fields was performed. This laid the groundwork for a theory of interaction of oblique magnetic fields with Josephson junctions of various geometries. This work is important for the Kibble-Zurek measurements done in this project, but has much wider applications. It stresses the importance of magnetic field alignment in *all* experiments involving overlapping layers of superconductors, such as Josephson junctions, and might even be used to design superconducting circuits for detecting the direction of a magnetic field, rather than simply its magnitude.

2 Theory

In this part of the dissertation, the theoretical background of the project will be covered. As this project is mostly experimentally oriented, the theoretical description will be brief and phenomenological. For details and more elaborate derivations of the enclosed material, references are given as appropriate.

2.1 Phase transitions

The phase of a system, is defined as an area in the parameter space describing the system in which all the the physical properties of the system are essentially uniform. By this definition, a phase transition occurs when some property of the system changes as one or more parameters are changed. Depending on the nature of the property change, the phase transition is assigned a number called the order of the phase transition. If the change in properties is discontinuous, it is called a first order phase transition, and if it is N times differentiable, it is called an (N+1)-order phase transition.

Phase transitions in general, is a huge and rather complex part of thermodynamics and statistical physics, and a more detailed discussion is not necessary to describe the effects measured in this work. For the present, it is sufficient to note, that in a second-order (or higher) phase transition, there is no latent heat involved. Essentially, this means that the energy difference between the two phases goes smoothly to zero as the system nears the phase transition. This is important, as the related heat transport would otherwise increase the time required to complete the phase transition.

It also has profound consequences for the presence of fluctuations, which plays an important role in the non-equilibrium phase transitions, the rest of this dissertation is devoted to. When close enough (in parameter space) to a phase transition, the energy difference between the two phases get so small, that thermal fluctuations are enough to generate drops of the unstable phase. The size distribution of the drops are a function of the distance to the phase transition. These drops are the seeds, or *protodomains*[1], of the domains seen after the transition. The ordered phase becomes stable as the temperature drops further, through T_c, as this is now the ground state of the system. Thus, it becomes energetically favorable for the protodomains to expand. Since it is a second order phase transition, the only limiting factor in the speed of this expansion is the maximum velocity of information, which is system dependent (second sound in superfluid LHe, Swihart velocity in Josephson junctions, speed of light in the universe, etc). This expansion continues until each domain reaches its neighbor domains, and the entire volume is subdivided into a number of domains, each in the ground state initially held by the protodomain.

Here, the order parameter, describing the ordered phase, will be denoted ψ. Below some critical temperature, T_c, ψ has an expectation value $<\psi>\neq 0$. For the systems considered here, we have $\psi = \rho_0 e^{-i\phi}$.

As the protodomains are essentially fluctuations, and no long-range interactions exist between domains in the systems of interest to this work (unlike ferromagnets), each protodomain selects the ground state from the available ground state manifold(see section 2.2.2) at random. The size

of the protodomains must initially be on the order of the correlation length of the system, denoted $\xi(T)$ and have a mean lifetime denoted $\tau(T)$.

In general, any parameter in phase space can be used to navigate the system through phase space to the transition, but typically temperature is used as a controlling parameter, although other groups have used other parameters[14, 15].

2.2 Symmetry and how to break it

Generally speaking, the concept of symmetry comes from the idea of *transformations*. A symmetry is a property of a system, that means that under certain transformations, some property of the system is unchanged or *invariant*, according to a particular measurement. Common examples of transformations could be rotations, reflections and translations of the coordinate system of measurements, but also gauge transformations can be the origin of symmetries.

Many types of symmetries are possible, when describing physical systems, and it is beyond the scope of this work to give a detailed description. However, as symmetry breaking is an essential part of the theoretical background for the measurements done, a few illustrative examples will be given in this section.

Typically, symmetries are thought of as a geometric property, rather than a mathematical concept. In order to maintain, as far as possible, the connection to the commonly appreciated use of symmetry, geometric equivalents will be given to the symmetries described below.

2.2.1 Examples of symmetries

Reflection symmetry, or inversion symmetry, is used to describe a system, which is unchanged when reflected in a point, line or plane. Mathematically, this is equivalent to flipping the sign of an uneven number of coordinates, called a *parity transformation*. An example can be seen in Fig. 2.1(a), which could describe the potential of a DC-SQUID magnetometer with one half flux quantum through the superconducting loop. In this case, the system has 2 degenerate ground states at the minima of the curve, $M = \{\pm\rho\}$ (which in the case of a DC-SQUID magnetometer means that two distinct circulating currents are allowed in the ground state). A geometrical equivalent is shown in Fig. 2.1(b).

Rotation symmetry describes a symmetry under rotation, which can be either continuous or discrete. A circle is a continuously rotationally symmetric object, where a square is a 4-fold discretely symmetric object under rotation. Continuous rotational symmetry is a common constituent of spontaneous symmetry breaking, both on the cosmological scale, solid-state systems[5] and even mechanical systems. The so-called mexican hat potential drawn in Fig. 2.1(c) is characteristic of second-order phase transitions described using Ginzburg-Landau theory. Here, the system has a continuum of degenerate ground states, $M = S$, corresponding to the circle at the bottom of the valley of the hat. Two rotationally symmetrical geometries are shown superimposed in Fig. 2.1(d). The square has a 4-fold rotational symmetry, where the circle has continuous rotational symmetry. Of course, the combination of the two has only the symmetry properties that both possess. Incidentally, this figure also has several reflection symmetries.

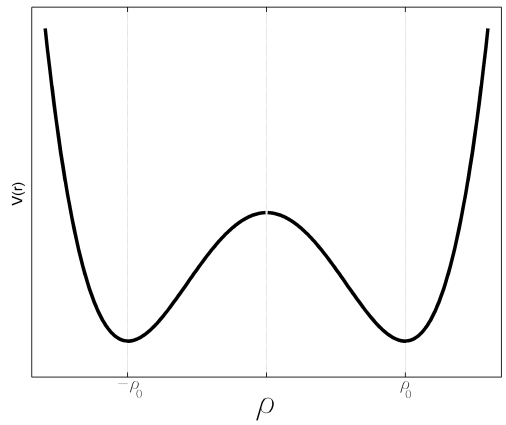

(a) Reflection symmetric potential

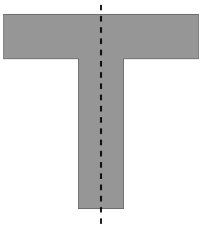

(b) Reflection symmetric geometry

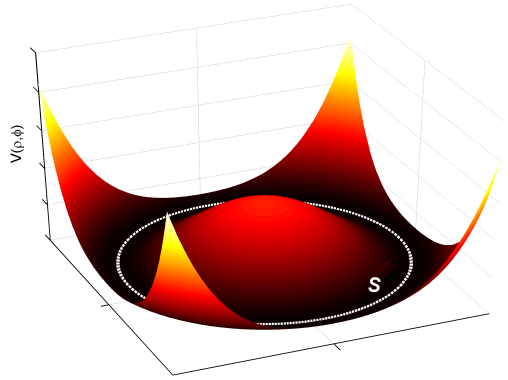

(c) Rotationally symmetric potential

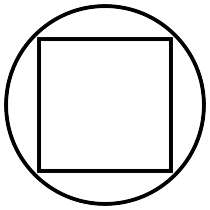

(d) Rotationally symmetric geometry

Figure 2.1: Examples of symmetries.

2.2.2 Topological defects

When a phase transition is completed in finite time, causality requires that parts of the system sufficiently far from each other must go through the phase transition independently. After the transition, the system has a manifold of degenerate ground states, denoted M. As seen in Fig. 2.1, M is a result of the symmetry of the potential[1], and might contain only a single point.

If a system undergoing a phase transition in a (short) finite time, has a degenerate ground state manifold, M, with more than one element in it, a spontaneous symmetry breaking can occur. If the system is also larger than the distance phase information can cover during the time of the phase transition, the result will generally be that the system is subdivided into smaller domains, in which the ground state has been chosen independent of each other. As an idealization, it is

assumed, that the result is a volume subdivided into N regions in which the order parameter is constant in the chosen ground state, $\psi_n, n \in \{1, 2, \ldots, N\}$. These domains are initially bounded by discontinuous jumps between domains.

Depending on the topology of M several scenarios are possible when looking at the interface between two domains. In case M is disjoint, two neighboring domains might have no continuous path connecting them in M, and so an area, not in M must separate them. Physically this means, that the boundary between the two domains cannot be in one of the ground states of the system, and that there is no way to remove it from the system. Because it is topologically stabilized, this is called a topological defect. As it has a dimensionality of one less than the domain it is called a *wall* defect.

If a continuous path exists in M connecting the two selected ground states, the interface will have a finite width, in which the order parameter adapts smoothly, by following the path in M. In general, the assumption is that this path will be chosen in accordance with the geodesic rule, when more paths are available. This means, that the shortest path in phase space is always chosen, which corresponds to choosing the path based on minimization of gradient energy. There has been some debate about the validity of this assumption[16, 17], but experiments seem to agree with the predictions arising from it.

In any case, it is always possible to connect two domains without leaving M, and therefore no area is left outside of M. However, if three domains meet at an edge, each with a distinct ground state (of which all are continuously connected in M), it is possible to create a closed path on M which goes from ψ_1 to ψ_2 over ψ_3 and then back to ψ_1. Here ψ_n is the expectation value for ψ, $< \psi >$ in domain number n. If this closed path can be continuously deformed in M to a point, the three domains can combine leaving no unordered phase. On the other hand, if the closed path cannot be continuously deformed to a point, the line along the edge must have a core of unordered phase to mediate the ordered domains. This type of topological defect is called a *string*, and is the source of measurements in the present work.

A third type of defect, the *monopole*, can occur if the topology of M is even more complicated, but as this is not the case for the present work, the reader is referred to [1] for a treatment of this case.

2.2.3 Spontaneous symmetry breaking

Symmetry breaking is the case where a system in a state, which possesses a certain symmetry, is changed into a different state, which has a lower symmetry. An example is that of a virgin ferromagnet with no average magnetic moment, which is magnetized in a particular direction for the first time, thus removing the rotational symmetry of the system.

Spontaneous symmetry breaking is the, perhaps unintuitive, case of symmetry breaking without the presence of an asymmetric cause. In the ferromagnet example, the magnetizing field is an asymmetric cause, and as such is is not surprising to find the resulting system being asymmetric as well. Spontaneous symmetry breaking occurs when a state becomes unstable, and has several new ground states, to go to, of which some or all have a lesser degree of symmetry.

An example of a potential, which could describe this, is shown in Fig. 2.2. This potential could describe a system consisting of a light ring, with a mass attached to it at some point of the perimeter. If this ring is put vertically on a frictionless substrate and rotated along its diameter,

the ground state position of the mass (at the bottom at zero rotation velocity) becomes unstable. It breaks up into two separate ground states, in which the mass is either to the right or left of the part of the ring touching the ground. The different curves in Fig. 2.2 correspond to different rotation speeds. This can be seen as a simple example of mechanical, spontaneous symmetry breaking.

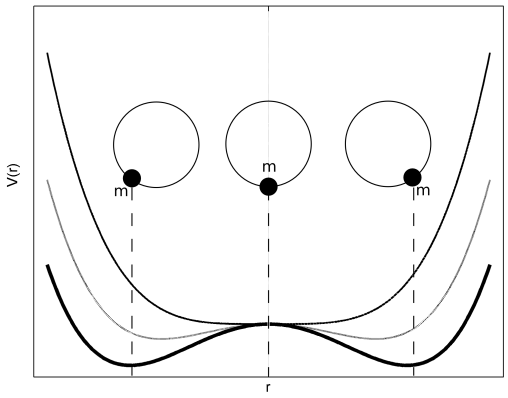

Figure 2.2: The evolution of an example potential during a spontaneous symmetry breaking, and its mechanical analogue.

2.2.4 From domains to defects

The previous sections dealt with symmetry breaking and topological defects by invoking the domain model. In this section, the link between domain structure and defects will be established as well as providing a starting point for extending the standard Kibble-Zurek model to systems with an already broken symmetry[18]. As the systems under consideration in this work are one-dimensional, this section will assume, that domains are essentially aligned in a ring of circumference, C, with no structure in the remaining two spatial dimensions. This assumption is only valid as long as the dimensions of the system in those two directions are both smaller than the minimum correlation length obtained by using the available quench rates in experiments.

Using the simplest possible model, which is also employed in [1], it is assumed that the phase transition divides the ring into N domains, in each of which the phase, ϕ, of the order parameter is constant. N is a function of the quench time, τ_Q, and thus of the cooling rate, as described in section 2.4. Furthermore, the domains are causally disconnected, and therefore choose their respective phases, ϕ_n, independently. Furthermore, the geodesic rule is applied, meaning that when two domains meet, the wavefunctions connect using the shortest possible path in phase.

Because the system is periodic, the cumulative phase change around the ring must be equal to an integer number multiplied by 2π. Let $G_N(\Delta\phi)$ be the probability that the change in phase ϕ is $\Delta\phi$ after N domain boundaries. For each domain boundary, the independence of phase choice, requires that

$$G_1(\Delta\phi) = \begin{cases} \frac{1}{2\pi} & \text{for } -\pi < \Delta\phi < \pi \\ 0 & \text{otherwise} \end{cases} \tag{2.1}$$

Increasing N, $G_N(\Delta\phi)$ is determined as a continuous random walk, by $N-1$ self-convolutions of G_1

$$G_N = \underbrace{G_1 * \ldots * G_1}_{N-1 \text{ times}} . \tag{2.2}$$

Using the geodesic rule for the final step in phase to close the ring, the probability of ending with a cumulative phase change of $2m\pi$ is

$$f_m(N) = \int_{-\pi+2m\pi}^{\pi+2m\pi} d\Phi G_N(\Phi) = 2\pi G_{N+1}(2m\pi) . \tag{2.3}$$

This result correlates the number of domains, N, expected from Kibble-Zurek theory, to the probability of generating a specific number of defects, m. However, as this is only applicable for integer number of domains $N = C/\bar{\xi}$, it needs to be generalized. For large N it is simple, as the self-convolutions quickly converge to a Gaussian distribution

$$G_N(\Phi) = \frac{1}{\sqrt{2\pi\sigma_N^2}} e^{\frac{\Phi^2}{2\sigma_N^2}} , \tag{2.4}$$

where

$$\sigma_N^2 = N\pi^2/3 . \tag{2.5}$$

The last choice is made so the discrete domain and Gaussian distribution results coincide for large N. To properly incorporate non-integer values of N for $N = C/\bar{\xi}$ it is necessary to give up the independent sector model completely, and in stead look at a continuous variable with Gaussian correlations. However, the result of this slightly complicated operation is strikingly similar, qualitatively and quantitatively, to the above, even in the low-N limit. A comparison between the independent sector model, the Gaussian approximation to it, and the Gaussian correlation calculation, can be seen in Fig. 2.3.

2.2.5 Kibble-Zurek in an already symmetry broken phase

An additional bonus to treating the phase transition in the way of Sec. 2.2.4 is that it can be easily extended to systems with pre-broken symmetries[18]. The simplest way to do this is to modify G_1 of Eq. (2.4) by allowing a non-zero average, which is dependent on the symmetry-breaking variable. In the case of superconducting rings and annular Josephson junctions, this is the magnetic field perpendicular to the ring, B. The average of G_1 is now set, so that the average number of defects is equal to one, when the magnetic flux density is equal to one magnetic flux quantum per ring area. This is equivalent to setting

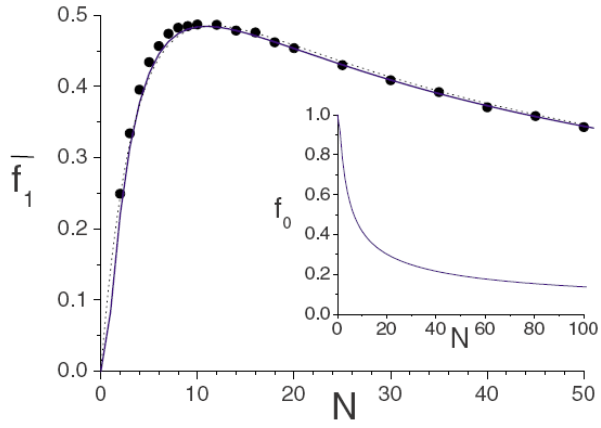

Figure 2.3: Comparison of the three approaches to finding the trapping probability of a single defect as a function of the number of domains. The three lines correspond to the independent sector model, the Gaussian approximation to it, and the Gaussian correlations model. They are indistinguishable except for $N < 2$. The inset shows the case of no trapping[18].

$$G_{N,\bar{n}}(\Phi) = \frac{1}{\sqrt{2\pi\sigma_N^2}} \exp - \frac{\left[\Phi - \bar{\Phi}(B)\right]^2}{2\sigma_N^2} \,, \tag{2.6}$$

where $\bar{\Phi}(B) = 2\pi\bar{n}(B)$, and

$$\bar{n}(B) = \frac{1}{2\pi}\Delta\phi = \frac{\varepsilon}{4\pi\hbar} eC^2 B \,, \tag{2.7}$$

where ε is a measure of the degree of symmetry breaking imposed by the field. For a single superconducting ring in a transverse field $\varepsilon = 1$ and for an annular Josephson junction it is dependent on geometry, though usually less than unity. The parameter, $\bar{n}$ is known as the *winding number*. In the case of an annular Josephson junction, ε is the fraction of the magnetic field leaking through the barrier plane[18]. In effect, $\bar{n}$ measures the number of defects, that would be seen if the Kibble-Zurek mechanism could be disregarded, and if the number was not restricted to integer values. It could be thought of as a weighted average. The theory makes predictions, that are experimentally testable. The shape of the probability of finding a single defect as a function of $\bar{n}(B)$ and number of domains, N is shown in Fig. 2.4. For a standard Kibble-Zurek mechanism experiment, measurements attempt to determine the curve formed by Fig. 2.4(b) and the plane defined by $\bar{n} = 0$.

Finally, the probability of finding m defects (fluxons) in the presence of an external magnetic field will be

$$f_m(N, \bar{n}) = \int_{-\pi+2m\pi}^{\pi+2m\pi} d\Phi G_{N,\bar{n}}(\Phi) \,. \tag{2.8}$$

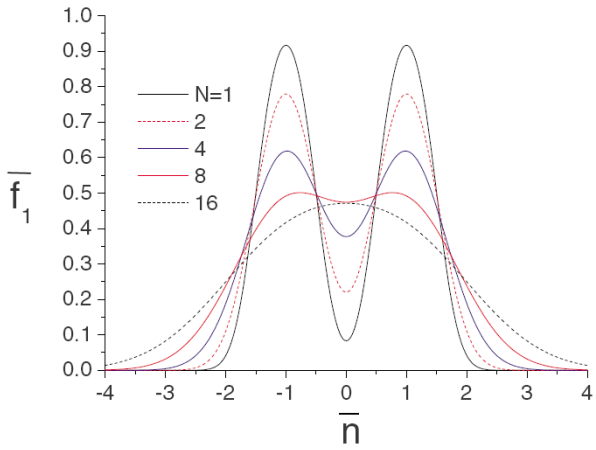

(a) Cuts at different values of N

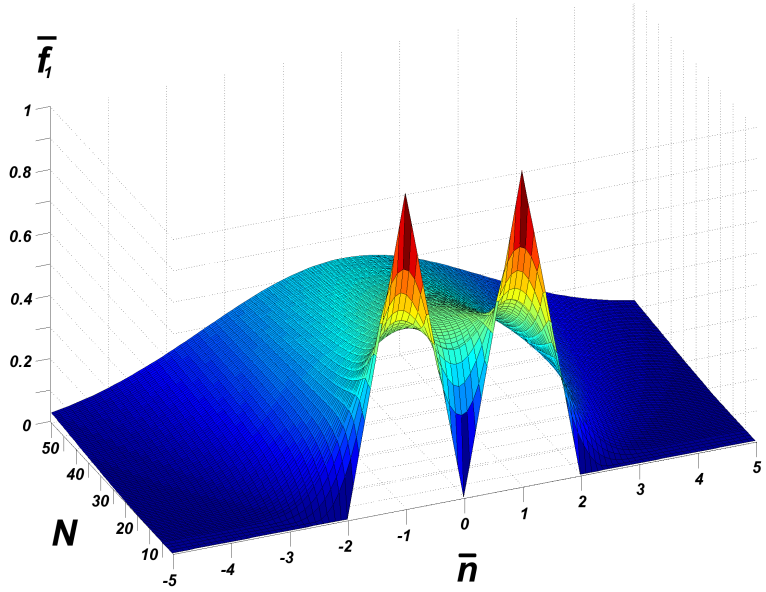

(b) Full plot

Figure 2.4: Plots of the predicted dependence of single-defect production as a function of number of domains, N, and induced defects, $\bar{n}$. In (a), cuts at different values of N is plotted on top of each other, and in (b) the full plot is shown. A typical Kibble-Zurek experiment will attempt to measure the cut in the plane defined by $\bar{n} = 0$. This cut is shown in Fig. 2.3[18].

The measured quantity is f_m for cases in which the sign of topological defects can be determined and $\bar{f}_m = f_m + f_{-m}$ for cases that can only determine the number of trapped defects.

2.3 Original theory

2.3.1 Kibble

In the original paper describing the precursor to what is now known as the Kibble-Zurek mechanism[1], Kibble modeled a rapid second-order phase transition of the early universe using a simplified Ginzburg-Landau theory. The idea was that fluctuations in the order parameter close to the critical temperature, T_c, would scramble the order parameter. The correlation length of the system, ξ, freezes in, when the thermal energy available is equal to the free energy associated with a fluctuation of scale ξ, which becomes larger away from T_c. Below this temperature, denoted T_{GL}, fluctuations still exist but can no longer modify the large scale domain structure.

In Fig. 2.5 this is illustrated as a jump directly to the leftmost column of the second row. After this, the initial domain structure is equilibrated by thermal fluctuations as long as the temperature is above T_{GL}, and at T_{GL} the structure can no longer be modified by the thermal fluctuations, and the domain structure freezes (row three).

The problem with this approach, when comparing to measurements, is that it exhibits no scaling behavior. The cooling rate enters the equations at no point, and as such, the domain structure should be similar for all experiments, and only decided by the system in question (or rather the dependence of the free energy of its fluctuations upon the temperature). One could attempt to fix this discrepancy by taking the time constant of domain formation into consideration. In this case, the average domain size will be the result of the finite cooling time racing against the finite equilibration time of domain sizes. Experiments have shown strong disagreement with the Ginzburg-Landau fluctuation relaxation mechanism of Kibble, but hinted that it may play a role for very slow cooling and/or systems in which T_{GL} is significantly lower than T_c, such as superfluid ^{4}He[19].

Later, this approach was further discredited in simulations by taking a cold system above T_{GL}, but below T_c and keeping it here for some time, thus allowing equilibration of the domain structure by Ginzburg-Landau fluctuations. However, after cooling again, the resulting defects were almost identical in all cases[20]. From this numerical experiment, it was also seen, that in order to erase the topological defects, it is necessary to heat the system significantly above the phase transition temperature.

Later, Kibble reformulated the theory to be limited by causality[3]. In this evolution, the limiting factor is the finite time of the phase transition combined with a finite speed of information. At its foundation lies the fact, that for a domain with a well-defined order parameter to grow, information needs to be transfered across the domain boundary. This limits the boundary velocity, from above, to the speed of information.

The speed of information is system dependent, from the speed of light in the universe over the speed of second sound in superfluid helium to the Swihart velocity of Josephson junctions. The speed of information can be a function of temperature, as is seen in particular in superconducting systems.

The adiabatic, or equilibrium, correlation length, $\xi_a(T)$, goes to infinity at $T = T_c$. It is possible to obtain the quasi-equilibrium domain boundary velocity during cooling by applying the chain rule

$$\frac{d\xi_a}{dt} = \frac{d\xi_a}{dT}\frac{dT}{dt} \,. \tag{2.9}$$

As ξ_a diverges at T_c and the cooling rate $\frac{dT}{dt}$ is finite, the value of the above expression will exceed the speed of information, c in the system, *regardless* of the magnitude or functional form of it, as long as it does not diverge at T_c, which would be unphysical. In general, the equilibrium correlation length divergence at the time, $t = 0$, when $T = T_c$ can be expressed as

$$\xi_a(t) = \xi_0 \left| \frac{t}{\tau_Q} \right|^{-\nu} , \tag{2.10}$$

where ξ_0 is the fundamental, zero-temperature length scale to be found from a microscopic theory of the system. The critical exponent ν describes the order of the divergence of the equilibrium (or adiabatic) scale close to the transition.

When the quasi-equilibrium value of the domain boundary velocity reaches the information velocity of the system, the domain size can no longer follow $\xi_a(T(t))$, but will in stead increase with speed $\bar{c}$. This period is called the impulse regime and ends when $\xi_a(T(t))$ decreases from infinity on the cold side of T_c. The time spent in the impulse regime is generally thought so small, that the contribution to the domain size from it ($d\xi_i = 2\bar{c}|\bar{t}|$) is assumed negligible. Here, $\bar{t}$ is the time at which the impulse regime starts. This is especially true for systems exhibiting critical slow-down of the information velocity as well, such as Josephson junctions and superconductors. The definition of $\bar{t}$ is the time at which

$$\frac{d\xi_a}{dt} = c \,, \tag{2.11}$$

where $\bar{c}$ is the speed of information.

After emerging back into the adiabatic regime on the cold side of the critical temperature, the domains, thus transfered from above T_c, are now the stable phase and will proceed to grow until they collide with their neighbors. It is assumed by Kibble that the scale of defect separation is the same as the scale of domain sizes at $\bar{t}$, ignoring factors of order unity.

The mathematical derivation for a superconducting ring using Kibble's causality approach can be found in appendix D.1.

2.3.2 Zurek

Zurek proposed a different approach[4, 5]. In stead of looking at the speed of information, he focused on the fluctuation relaxation time, $\tau(T)$, which is also a property of the particular system being studied. The relaxation time of fluctuations in the Ginzburg-Landau model, diverges similarly to the correlation length, but with a different exponent (see again appendix D.1).

Crudely, one can describe the relaxation time, as a measure for the lifetime of a domain. According to Zurek, the time at which the correlations freeze in, is determined by setting

$$\tau(T(\bar{t})) = \bar{t} \,, \tag{2.12}$$

where the $T(t = 0) = T_c$, that is the phase transition happens at $t = 0$. This corresponds to noting, that the domains present at the time $\bar{t}$ does not have time to disappear before reaching T_c. As for the correlation length, the divergence of the relaxation time close to T_c can be written as

$$\tau(t) = \tau_0 \left| \frac{t}{\tau_Q} \right|^{-\gamma}, \tag{2.13}$$

where γ is the critical exponent related to the relaxation time and τ_0 is the fundamental timescale set by the microscopic dynamics of the system in question.

After T_c the domains are in the stable state, and thus expand at the maximum rate allowed by the system, until they hit their neighbouring domains. It can be shown, that the causality approach of Zurek[5] is equivalent[21] to that of Kibble in [3].

In the illustration, Fig. 2.5, both the Kibble causal approach and this one, correspond to finding $\bar{t}$ from the chosen criterium, and then proceeding vertically down the column. In setting $\bar{t} \propto \sqrt{\tau_Q}$, the system critical exponents are implicitly selected. This particular choice is valid for superconductors[5] and some Josephson junctions[22, 23, 24].

What the illustration shows, is that depending on the value of $\bar{t}$, the size of domains going into the impulse regime varies. They are transported across the impulse regime approximately unchanged (row two) and then grow until they reach their neighbors (row three). Of course, after this epoch, there is further equilibration of the domain boundaries - they will generally collapse to single boundaries of width $\xi_a(T)$, for energetic reasons, even if they are topologically restricted from disappearing completely.

2.3.3 Hindmarsh and Rajantie

It is worth mentioning, that another process of symmetry breaking during phase transitions has been suggested by Hindmarsh and Rajantie[25]. It is relevant for systems going through their phase transition with significantly slower cooling rates than those appropriate for Kibble-Zurek theory. The main idea of the Hindmarsh-Rajantie mechanism is that fluctuations of the magnetic field can be frozen in as well as fluctuations of the order parameter.

The scaling of the Hindmarsh-Rajantie mechanism is also different; it predicts a scaling exponent equal to one half that of the Kibble-Zurek mechanism. It is not quite clear at which cooling rates the Hindmarsh-Rajantie mechanism will start being important, but it is only important for superconducting rings, rather than annular Josephson junctions. In any case, no change in scaling exponents for slow quenches was seen in the course of measurements on annular Josephson junctions.

Hindmarsh and Rajantie themselves state, that the only reasonable way to investigate this mechanism is to look at spatial correlation between created defects/anti-defects, rather than simply measuring the sum of defects produced.

2.3.4 Thermal gradients

The phase transitions discussed here are all causally limited. When attempting to implement this in real world experimental setups, thermal gradients are unavoidable. If the system is put together in such a way, that the temperature front moves slower than than the relevant speed of

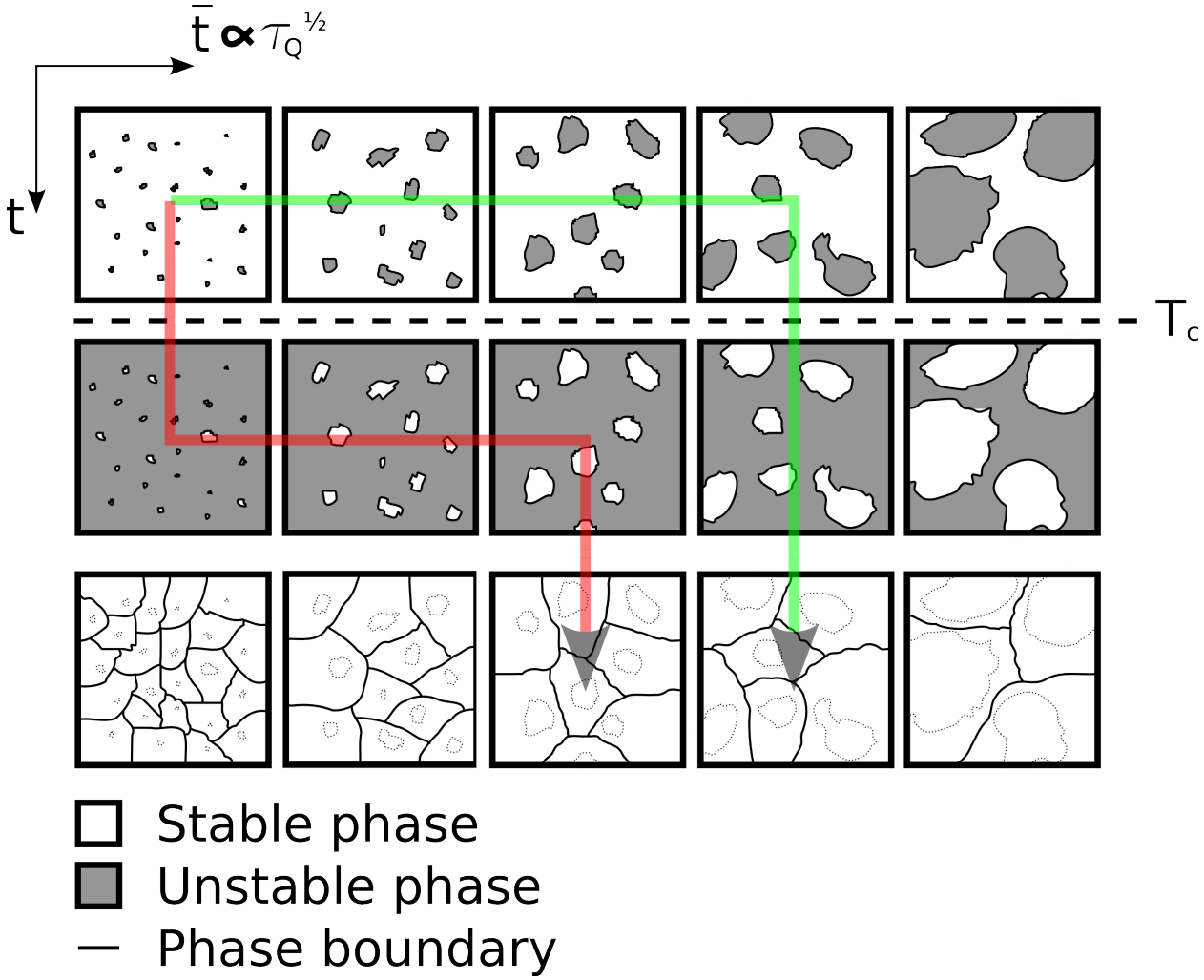

Figure 2.5: Graphical illustration of different approaches to modeling phase transitions.

information, it will be the heat transport, that limits the progression of the phase transition rather than the speed of information.

Therefore it is important to make an assessment as to how large thermal gradients can be accepted without interfering with the causal nature of the phase transition. To do this, it is necessary to determine a characteristic velocity of the propagating temperature front. The time scale of the temperature change is set by the quench time, τ_Q. The characteristic length scale, λ, of temperature change is[26]

$$\frac{1}{\lambda} = \frac{|\nabla T|}{T_c} \,. \tag{2.14}$$

From this, the characteristic velocity of the temperature front is

$$v_T = \frac{\lambda}{\tau_Q} = \frac{\left|\frac{dT}{dt}\right|}{|\nabla T|} \,, \tag{2.15}$$

where both derivatives are evaluated at $T = T_c$. It is clear, that when $v_T \gg c(\bar{t})$ the phase transition is governed simply by causality, as argued by the Kibble-Zurek description. When $v_T < \bar{c}(\bar{t})$ the limiting factor to ordering is the thermal front. According to [26], defect formation will still occur, but will be suppressed. The effect of the slowly moving temperature front is to effectively increase the value of $\bar{\xi}$. The critical value of characteristic temperature front velocity, v_{T_c}, separating the causal regime from the heat transport regime is set by the speed of information in the system $\bar{c}$

$$v_{T_c} \approx \bar{c} \approx \frac{\xi_a(\bar{t})}{\bar{t}} \approx c_0 \left(\frac{\tau_0}{\tau_Q}\right)^{\sigma} \,. \tag{2.16}$$

If the actual value of v_T is below this threshold, production of defects will be suppressed by a factor of $v_T/\bar{c}$[26]. However, according to numerical simulations by - among others - Zurek, the change is even more drastic, showing almost zero defect production when $v_T < v_{T_c}$[27], depending on modeling parameters.

2.4 Solid-state systems

Zurek[5] suggested using solid-state systems undergoing rapid phase transitions as analogues to cosmological phase transitions. The common denominator for these systems is the application of the Ginzburg-Landau theory to describe their phase transitions close to the phase boundary.

The foundation is the similarity of the potential contribution to the free energy close to the phase transition[5]

$$V(\psi) = \alpha(T - T_c)\left|\psi\right|^2 + \frac{1}{2}\beta\left|\psi\right|^4 \,, \tag{2.17}$$

where ψ is the order parameter of the system. This potential contribution is approximately satisfied in superfluid He, and emerges as a limiting case of BCS theory close to T_c[28] for superconductors. Thus, for superconductors the above potential is not just a phenomenological description, but a microscopically justifiable approximation of the BCS theory close to T_c. Essentially, Eq.

(2.17) can be thought of as a series expansion of the energy of the superconducting order parameter close to T_c, where $|\psi| \to 0$[29]. When looking at Eq. (2.17), it is obvious, that it is only stable if $\beta > 0$. Furthermore, at the transition temperature, α must pass through zero from above, as the minimum in the potential for $\alpha > 0$ is for $|\psi| = 0$. Finally, very close to T_c, $\alpha(T)$ can be Taylor series expanded around $T \approx T_c$, but below, to

$$\alpha \approx -\alpha' \left(1 - \frac{T}{T_c}\right). \tag{2.18}$$

The order parameter in a superconducting system can be interpreted as a collective wave function for the Cooper pairs. All experiments done in this project is made with superconducting systems.

In measurements, the probability of finding a single defect, $\bar{f}_1$, is determined as a function of cooling rate, or τ_Q. The two are related by

$$\left.\frac{dT}{dt}\right|_{T=T_c} = -\frac{T_c}{\tau_Q}. \tag{2.19}$$

The value of τ_Q should be thought of as a characteristic time related to the cooling cycle, but not an approximation to the actual time spent in the impulse regime. Using this definition,

$$\alpha \approx -\alpha' \left(\frac{t}{\tau_Q}\right). \tag{2.20}$$

The time spent in the impulse regime is a real measure of the time it takes to implement the phase transition, and is on the order of $2\bar{t}$. The relation between the microscopic relaxation time, τ_0, the characteristic cooling time, τ_Q, and the phase transition time is

$$\tau_0 \ll \bar{t} = (\tau_0 \nu)^{\frac{1}{\gamma+1}} \tau_Q^{\frac{\gamma}{\gamma+1}} \ll \tau_Q. \tag{2.21}$$

The average size of domains, $\bar{\xi}$ is

$$\bar{\xi} = \xi_a(\bar{t}) = \xi_0 \left(\frac{\tau_Q}{\tau_0}\right)^{\frac{\nu}{1+\gamma}}. \tag{2.22}$$

For reference, the critical exponent is denoted σ

$$\sigma = \frac{\nu}{1+\gamma}. \tag{2.23}$$

2.4.1 Annular Josephson junctions

The main results of this project have been obtained using annular Josephson junctions for studying the phase transition. The theoretical groundwork connecting the Kibble-Zurek mechanism to Josephson junctions was done in [22] and will be briefly described below.

The topological defects in Josephson junctions are called fluxons. Physically, they are magnetic flux lines penetrating the insulating layer between the two superconducting electrodes. In a simple linear Josephson junction, a fluxon would be topologically staple inside the junction, but could disappear out the ends. As this is a fairly high-probability process, it happens on a timescale on

the order of a few times the junction length divided by the Swihart velocity ($\approx$ 50ps). This could be reduced by having very reflective ends of the junction, but would still be at least similar to $\bar{t}$, essentially allowing the generated defects to disappear as fast as they would be generated.

To stabilize the defect, an annular junction is formed in the so-called Lyngby geometry, see 3.3. This creates another topological stability, by requiring the flux line in free space, associated with the fluxon, to pass through one of the two superconducting rings, thus trapping it perpetually.

General theory

In order to establish the analogy with the Kibble-Zurek mechanism, it is necessary to identify the main components: the correlation length and the relaxation time or the speed of information. The correlation length in a Josephson junction is easily identified as the Josephson penetration depth, λ_j, since this is the typical length scale over which the Josephson phase can change. As opposed to, for instance, superconductors, there is no obvious choice for the relaxation time of fluctuations in the Josephson junction. However, speed of information is reasonably identified with the Swihart[30] velocity in the junction. The Swihart velocity is essentially the velocity for electromagnetic radiation propagating between the electrodes. To a good approximation, the transmission is dispersionless, so the added problem of deciding whether the phase or group velocity should be used, is avoided. In any case, the important property is the scaling with temperature close to T_c, so even if the two were numerically different, it would only contribute to the final result with a prefactor, and not affect the scaling law obtained, unless the divergence properties were different as well.

Additional questions need to be answered in order to complete the Kibble-Zurek description of the annular Josephson junction. First of all, it is not possible to invoke any of the causality arguments mentioned in sections 2.3.1 and 2.3.2. The main problem is that above the phase transition of the superconductors, the Josephson phase is undefined, so no Josephson phase fluctuations can occur. Fortunately, nothing requires the application of the causal arguments above T_c - they may just as reasonably be applied after the phase transition. This approach is slightly less intuitive, but will be justified in the following.

During the superconducting phase transition of the individual rings at $T = T_c$, the Josephson phase starts appearing as the difference between the phases of the Cooper pair macroscopic wave function across the tunneling barrier. As the domains in the Cooper pair wave function are weakly coupled across the tunneling barrier, it is reasonable to expect a domain in one of the rings to 'infect' the twin area in the opposite ring with its choice phase. Close to the phase transition it is even reasonable to allow two twin domains to affect each others phases in such a way to reduce their Josephson phase, because the energy barrier between the degenerate ground states is exceedingly small. This picture is very similar to considering simply the Josephson phase as the order parameter in the phase transition. Below the transition temperature, the Josephson phase domains expand at the Swihart velocity, $\bar{c}$ until they reach their adiabatic velocity, after which the system evolves as if in equilibrium. This can be used to set a minimum value for $\bar{t}$, which is when $\bar{c}(t) = |d\xi_a(t)|/dt$. This is a lower bound, but is used as an order of magnitude estimation for $\bar{t}$[22].

Original description

In the most naive application of the above, the Swihart velocity and the Josephson correlation length at $\bar{t}$ is inserted[23, 24]. The Josephson penetration depth is

$$\lambda_J(T(t)) = \sqrt{\hbar/2e\mu_0 d_e(T(t))J_c(T(t))}\,, \tag{2.24}$$

where J_c is the critical current density and $d_e(t)$ is the magnetic thickness of the electrodes for DC fields. The magnetic thickness for constant magnetic fields is approximately constant close to the transition[31], so all of the temperature-dependence (and thus time-dependence) of the correlation length comes from J_c. For weak-coupling superconductors, the temperature dependence of J_c is given by the Ambegaokar-Baratoff equation[32]

$$J_c(t) = \frac{\pi}{2}\frac{\Delta(t)}{e\rho_N}\tanh\frac{\Delta(t)}{2k_BT(t)}\,. \tag{2.25}$$

Using this, the time dependence of λ_J close to the transition is

$$\lambda_J(t) = \xi_0\left(\frac{\tau_Q}{t}\right)^{\frac{1}{2}}\,. \tag{2.26}$$

The dependence of the swihart velocity[30] on temperature is described by

$$\bar{c}(t) = c_0\sqrt{\frac{d_{ox}}{\varepsilon_r d_i(t)}}\,, \tag{2.27}$$

where

$$d_i(t) = d_{ox}2\lambda_L(t)\coth\frac{d_s}{\lambda_L(t)} \approx \frac{\lambda_L^2(0)}{d_s}\frac{\tau_Q}{t}\,. \tag{2.28}$$

Combining Eq. (2.27) and (2.28), the scaling of the Swihart velocity becomes

$$\bar{c}(t) = c_0\left(\frac{t}{\tau_Q}\right)^{\frac{1}{2}} \tag{2.29}$$

Identifying equations (2.26) and (2.29) with equations (2.10) and (2.13), respectively, this corresponds to $\nu = \frac{1}{2}$ and $\gamma = 1$. From this, the critical scaling exponent of $\bar{\xi}$ is

$$\sigma = \frac{\nu}{1+\gamma} = \frac{1}{4} \tag{2.30}$$

Experimental results published in [23, 24] were ground-breaking in their broad range of cooling rates, but hampered by low statistical reliability, and a measurement system not designed for Kibble-Zurek measurements. The results fit the predictions from the simple theory above, and was seen as a verification of it. The reported scaling exponent was $\sigma = 0.27 \pm 0.02$, well in agreement with the exponent expected from theory.

Revised theory

Later experiments[33, 34], showed that the assumptions underlying the derivation of the scaling exponent, σ, were too simple. By using more detailed and realistic models of the temperature dependence of both the Swihart velocity and the correlation length, the theory was brought into agreement with new experimental data.

It is natural to begin the description of the revised theory by noting the places in which the first approach fails. Firstly, the Ambegaokar-Baratoff equation used in Eq. (2.25) is only valid for weak coupling superconductors, where the Josephson junctions used are based on Nb - a strong-coupling superconductor. For a strong-coupling superconductor, Eq. (2.25) is not necessarily true.

The Josephson junctions are fabricated by depositing Al on top of the bottom Nb electrode. Then the Al is partly oxidized, after which the Nb counter-electrode is deposited. This leaves a superconductor-normal metal-insulator-superconductor (SNIS) junction. Due to the proximity effect in the metal, the temperature-dependence of the critical current density is modified[35] to

$$J_c(t) = \alpha' J_c(0)\left(\frac{t}{\tau_Q}\right)^2 , \tag{2.31}$$

where α' is a constant depending intricately on the degree of proximity[34]. This means, that the correlation length, $\xi(T(t)) = \lambda_J(T(t))$, depends on temperature, like

$$\xi(T(t)) = \lambda_J(T(t)) = \left(\frac{t}{\xi_0 \tau_Q}\right)^{-1} , \tag{2.32}$$

rather than the square root scaling seen in Eq. (2.26) - equivalent to having $\nu_{rev} = 1$ in stead of $\nu_{org} = \frac{1}{2}$. In addition, in [24, 23] it was also assumed, that the Swihart velocity goes to zero at $T = T_c$. This is only approximately true, as the minimum velocity attained is not zero, but rather the normal-metal stripline limit $\bar{c}_{nn}$. As far as $\bar{c}_{nn} \ll \bar{c}(0)$ there is still approximate critical slowing down. Assuming that the temperature region, in which the Swihart velocity takes on its minimum value is larger than the impulse regime, the information velocity is now[33]

$$\bar{c} = \bar{c}_{nn} = \frac{2}{\delta}\sqrt{\frac{d_{ox} d_s}{\varepsilon \mu}} . \tag{2.33}$$

This depends very weakly on temperature, but does have a dependence on frequency through $\delta = \sqrt{\rho/\pi\mu f}$, ρ being the normal metal resistivity. According to [30], the temperature regime in which the velocity is constant is around 0.1% T_c. In order for the theory to be self-consistent, the time, Δt_{nn} spent with constant Swihart velocity, $c = \bar{c}_{nn}$ must be larger than $\bar{t}$ for all experimentally used τ_Q.

Using $\bar{c} = \bar{c}_{nn}$, the causal time, $\bar{t}$ as defined in Eq. (2.11), becomes[33]

$$\bar{t} = \sqrt{\frac{\xi_0 \tau_Q}{\bar{c}_{nn}}} = \sqrt{\tau_0 \tau_Q} , \tag{2.34}$$

where $\tau_0 = \xi_0/\bar{c}_{nn}$ [$\tau_0 = O(1\text{ns})$]. This corresponds to $\gamma = 1$. Thus, $\bar{t} \propto \sqrt{\tau_Q}$ and $\Delta t_{nn} = k\tau_Q$, where $k = 1 \cdot 10^{-3}$. The regime, in which the approximation holds is that in which

$$\Delta t_{nn} > \bar{t} \Rightarrow \tag{2.35}$$

$$\tau_Q > \frac{\tau_0}{k^2}\,. \tag{2.36}$$

For $k \approx 1 \times 10^{-3}$, this corresponds to $\tau_Q > 1\text{ms}$, which is the low limit of quench times in the performed experiments. For much lower values of τ_Q the scaling of the velocity should be similar to that of the original Josephson junction description. According to Eq. (2.23), the revised theory gives

$$\sigma = \frac{\nu}{1+\gamma} = \frac{1}{2} \tag{2.37}$$

2.4.2 Superconductors

Because of the direct applicability of Ginzburg-Landau theory to superconductors, the critical exponents can be extracted without problems. The equilibrium correlation length, ξ_a, and the relaxation time, τ, is defined from the time-dependent Ginzburg-Landau equation[29]

$$\xi_a^2(T) = \frac{\hbar^2}{2m^*|\alpha(T)|} \propto \frac{\tau_Q}{t} \tag{2.38}$$

$$\tau(T) = \frac{\pi\hbar}{8k_B(T-T_c)} \propto \frac{\tau_Q}{t} \tag{2.39}$$

Comparing to the general equations for diverging equilibrium correlation length and relaxation time, Eqs. (2.10) and (2.13), the critical exponents can be identified as $\nu = \frac{1}{2}$ and $\gamma = 1$. Using Eq. (2.22) this gives a prediction for superconductors of

$$\bar{\xi} \propto \tau_Q^{\frac{1}{4}} \tag{2.40}$$

When aligned in a one-dimensional system such as a ring, in the limit of large domains compared to the system size, the probability of trapping one fluxoid in the ring, $\bar{f}_1$, for $C \lesssim \bar{\xi}$ is[24]

$$f_1 \approx \frac{C}{\bar{\xi}} = C\tau_Q^{-\frac{1}{4}}\,, \tag{2.41}$$

which means, that for a superconducting ring described by the standard Ginzburg-Landau theory,

$$\sigma = \frac{1}{4} \tag{2.42}$$

2.5 Josephson junctions in oblique fields

Traditionally, magnetic fields applied to planar Josephson junctions, it has almost always been done in the plane of the junction. There are two obvious reasons for this: (1)demagnetization effects from the superconducting electrodes are difficult to take into account, and (2)according to the Josephson equation[36] the junction is insensitive to perpendicular fields

$$\nabla\phi = \frac{2\pi d_e \mu_0}{\Phi_0}\mathbf{H}\times\mathbf{n}\,, \tag{2.43}$$

where ϕ is the Josephson phase, d_e is the magnetic thickness, Φ_0 is the magnetic flux quantum, $\mathbf{H}$ is the magnetic field and $\mathbf{n}$ is a normal vector to the junction plane.

Naively, using a field slightly out of the plane of the junction will change the actual field in the junction, B_{JTJ} negligibly

$$B_{JTJ} = \hat{e}_{\parallel} B_a \cos\Delta\theta + \hat{e}_{\perp} B_a \sin\Delta\theta\,, \tag{2.44}$$

where B_a is the applied field strength, $\Delta\theta$ is the angle misalignment, and $\hat{e}_n$ is the unit vector in the n-direction. According to Eq. (2.43), the second term could be ignored, and the first one is only modified in second order of $\Delta\theta$.

However, this picture is too simple[37, 38, 39]. The main reason is, that depending on surrounding superconducting electrode configuration, the field actually in the junction can be significantly changed from that given in Eq. (2.44). Even in the simplest geometries, such as the overlap junction, this equation is violated.

The mechanism responsible for this, is the field induced in the junction area from screening currents in the electrodes. In [40, 41], the effects of a perpendicular magnetic field on the maximum critical current of Josephson junctions of various geometries, is investigated based on finite-element magnetostatic simulations. Here it is found, that more often than not, the perpendicular field component is more potent in modulating the maximum critical current, than an in-plane field of the same field strength.

In a new paper[42], it is shown, that the correct form of Eq. (2.44) for the junctions used in this project (Nb-Al-AlOx-Nb junctions) is

$$B_{JTJ} = B_a(\hat{e}_{\parallel}\alpha_{\parallel}\cos\Delta\theta + \hat{e}_{\perp}\alpha_{\perp}\sin\Delta\theta)\,, \tag{2.45}$$

where α_n is a prefactor, describing the sensitivity of this particular junction geometry to fields in the direction $\hat{e}_n$. Normally, $\alpha_{\parallel}$ is very close to unity, as only field focusing in the plane because of the junction electrodes have an effect on this. From the linearity of the Maxwell equations this is the most general form it can take. This comes from the fact, that any field in the junction must be the result of a superposition of the fields from an in-plane component and a perpendicular component. Using magnetostatic simulations, the field solution for the magnetic field is found in the junction area, and by integrating Eq. (2.43), the Josephson phase can be found everywhere in the junction. This gives $\phi = \phi(x,y) + \phi_0$ in the junction area, where ϕ_0 is an integration constant independent on position. The maximum critical current is found by maximizing

$$I_c = I_0\sqrt{\langle\sin\phi\rangle^2 + \langle\cos\phi\rangle^2}\,, \tag{2.46}$$

where

$$\langle \sin\phi \rangle = \int_{A_{JTJ}} \sin(\phi(x,y) + \phi_0) dS \ ,$$

with respect to the constant, ϕ_0. As the effect of the two orthogonal components can be calculated separately, and simply combined using the sensitivities, the junctions' response to a magnetic field at any angle can be found. In addition, if analytical approximations can be made to the field solutions found numerically, the analytical approximations to $I_c(B_a, \theta)$ is easily obtained by integration. The analytical approximations found in [42] are listed in Table 2.1. The corresponding junction geometries are shown in Fig. 2.6.

Geometry	$\phi_\parallel$	$\phi_\perp$
Overlap	$\bar{y}$	$\sin\bar{y}\frac{\cosh\beta\bar{x}}{\sinh\beta}$
Annular	$\sin\phi$	$\sin\phi + \delta\sin 3\phi$
Lyngby	$\sin\phi$	$\sin\phi$
Cross	$\bar{y}$	$\sin\bar{y}\frac{\sinh\beta\bar{x}}{\cosh\beta} + \sin\bar{x}\frac{\sinh\bar{y}/\beta}{\cosh 1/\beta}$

Table 2.1: Analytical approximations to the Josephson phase variations in perpendicular and in-plane fields. The parameter ϕ is the angular coordinate in a cylindrical coordinate system in the plane of the junctions, concentric with the annular junctions. The coordinates $\bar{x}$ and $\bar{y}$ are the normal coordinates, x and y, normalized to the junction geometry. Thus the junction area spans $\bar{x} = -1$ to $\bar{x} = 1$ and likewise for $\bar{y}$.

2.6 Coil in a superconducting shield

It is a common approach in cryogenic magnetic measurements[43], such as the ones of this project, to use superconducting magnetic shields. This is one of the simplest applications of the Meissner effect, which ensures, that no magnetic field penetrates the superconducting shield. A can-shaped shield can be used to create a volume, that is almost entirely insensitive to external magnetic fields.

In addition, active compensation or actuation of the magnetic field inside this volume can be achieved by placing a coil inside this volume. The shielded volume is often small, both for shielding reasons, and as a result of limited cryostat size. The size of coils are generally as large as possible, because of field homogeneity. This often results in field coils in relatively close proximity to the superconducting shield. It is not surprising, but often neglected, that the presence of a superconductor close to a field coil will strongly deform the generated field, and, thereby, the coil factor, C, defined as

$$B_i = CI_{coil} \ , \tag{2.47}$$

where B_i is the generated field in the center of the coil, and I_{coil} is the current in the coil.

By applying Ampere's law, it is possible to find an approximate analytical solution to the field problem, by using the infinitely long, thin solenoid in an ideal superconducting shield, as a model.

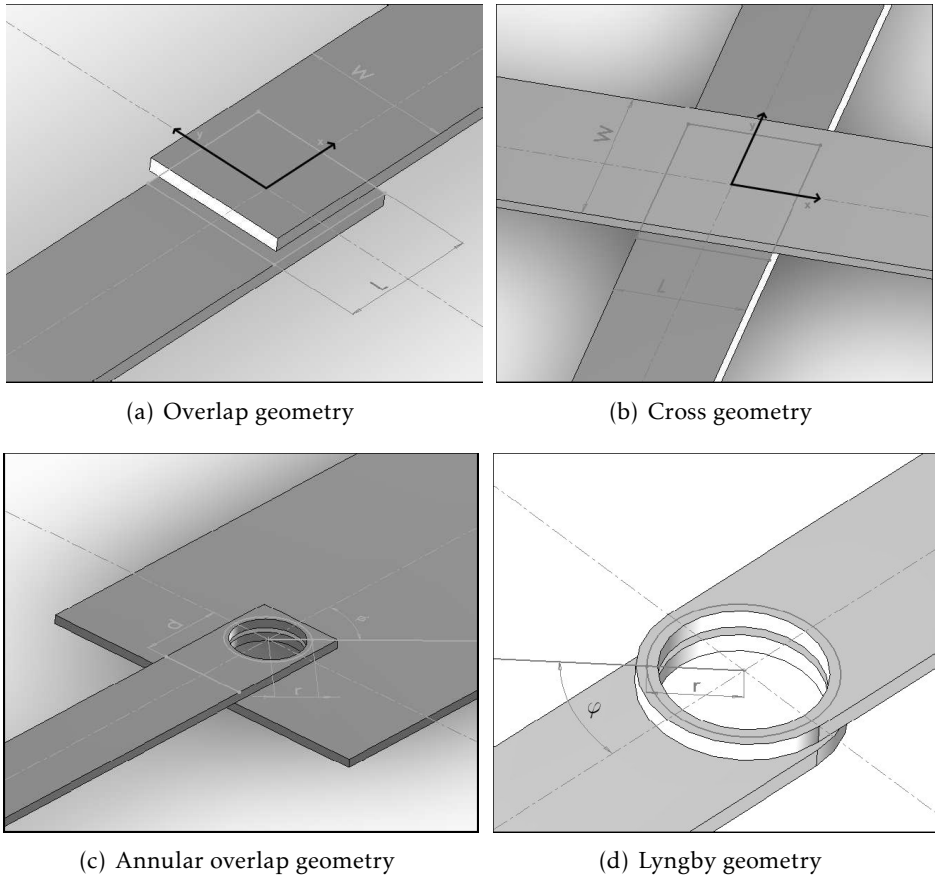

(a) Overlap geometry

(b) Cross geometry

(c) Annular overlap geometry

(d) Lyngby geometry

Figure 2.6: The geometries used in finite-element simulations of the influence of oblique magnetic fields on different types of junctions[42].

For the derivation and more details, see App. F. The result is that the field inside the coil enclosed in a magnetic shield is

$$\frac{B_i}{B_{i0}} = \frac{R^2 - r_{coil}^2}{R^2} = 1 - \left(\frac{r_{coil}}{R}\right)^2 , \tag{2.48}$$

where B_{i0} is the value for an unshielded coil, R is the inner radius of the superconducting shield, and r_{coil} is the radius of the (thin) coil.

The result above shows, that for a sample holder with coil, such as the one used in this project, enclosed in a tight-fitting superconducting shield, then the applied field to the sample area will be significantly smaller than expected. For the setup used for most of our experiments, the field reduction from this effect is on the order of 90%.

If strong fields are needed, and space is limited, a possible solution is to insert a thin sheet of high-permeability metal in the area between the coil and the superconducting shield. The effect of this is to insert a virtual vacuum for the magnetic field, and it has been shown that this heals the coil-factor to about 95% of the free-space value[44], see App. F.

3 Experimental methods

In this section experimental considerations of the project will be treated. A thorough analysis of the problems and the reasoning behind the solutions will be given. For alternative solutions and outlook on further experiments refer to Sec. 6.3.

3.1 Measurement challenges and goals

The goal of the measurements performed in this project is to detect topological defects produced in the fast quench of superconducting systems. During the project, two main courses of experimental work has been pursued - detecting fluxons generated in annular Josephson junctions and detecting fluxoids produced in superconducting rings. Each method has its own merits and challenges, but they share some common requirements based on the similarity of the systems and the Kibble-Zurek mechanism.

Generally, experiments consist of cooling a vacuum can with the sample holder and sample inside to the cryogenic base temperature (4.2K for LHe). From this base temperature, the sample is heated to significantly above the phase transition temperature and then allowed to cool through the transition passively. After this, the number of defects created is counted. The heating/cooling cycle is repeated for as many times as necessary to obtain the probability of defect production with reasonable statistical uncertainty.

3.1.1 Magnetically shielded environment

The symmetry breaking in both systems is magnetic in origin. Therefore it is essential to conduct measurements in a magnetically shielded volume, although progress has been made on Kibble-Zurek theory in a pre-broken symmetry, see Sec. 2.2.4 and [18]. The required level of shielding is determined by requiring that it should be significantly below the level required to induce trapping in the superconducting ring(s) of the system.

$$B_{ext} \ll \frac{\Phi_0}{\pi r^2} = \frac{h}{2e\pi r^2} , \tag{3.1}$$

where r is the radius of the ring. The largest rings in the experiments performed have a radius of approximately 300μm, which sets the limit

$$B_{ext} \ll 10\text{nT} .$$

This is a factor of approximately 4000 below the magnetic field of the Earth in Denmark. In addition, high-frequency fields can easily be imagined to have higher impact on the phase transition through resonances or magnetic correlation between different domains. The limit also illustrates, that all materials used in designing the sample holder must be nonmagnetic.

3.1.2 Electrical noise and bandwidth

As the setups used involve low-level voltage measurements, the electrical noise of the detection system is important. Typical voltages are in the μV range, so the total noise of the detection system must be significantly below this.

This sets limits on the shielding of all electrical components, filters, amplifiers and data acquisition system. The typical frequency of signals measured are from 0 to a few MHz, which defines the bandwidth. Most individual signals are confined to smaller bands within the total bandwidth, though.

3.1.3 Thermal response

Depending on the system and model chosen (see Chap. 2), the probability of finding defects is predicted to scale with the cooling rate with an exponent of (0.25-0.5). This means, that in order to see a doubling in trapping probability, the cooling rate must be increased by a factor of 4-8. Therefore, in order to see reliable scaling behavior, several decades of cooling rates must be available in the system.

As the measurements on the Kibble-Zurek defect production are almost invariably statistical of nature, there is a natural lower limit to the cooling rates. Cooling through an interval limited by $T_c \pm T_c/2$ should take no more than a few seconds for reliable statistics to be available, as at least several hundreds of repetitions are needed for each datapoint. Assuming a Poisson distribution of the defect production events, the standard deviation of the defect production probability is proportional to the square root of the number of defects produced. So if the probability is $f_1(\tau_Q)$, and the goal is to achieve a relative standard deviation on the probability equal to $\sigma_r = \sigma(\tau_Q)/f_1(\tau_Q)$,

$$N_e(\tau_Q) = \frac{1}{\sigma_r^2 f_1(\tau_Q)} \tag{3.2}$$

is the number of quenches necessary. For the reasonable values of $\sigma_r = 0.1$ and $f_1(\tau_Q = 0.01$, this means that a total of 10.000 quenches must be performed to generate one datapoint on the $f_1(\tau_Q)$ plot with a 10% relative standard deviation. For practical reasons, this is not acceptable for measurements with an individual duration above a few seconds.

Another important part of the thermal system is the uniformity of cooling. This problem is treated in Sec. 3.2.4.

3.1.4 Deformation during cooling

For optical detection and heating systems, it is important to avoid misalignment during the first cooling in the cryostat. Any misalignment will show up as systematic errors in measurements or thermal gradients in the system.

The problem arises for two reasons. One is that the cooling of the sample holder, and thus any optical mounts in it, will happen in a non-trivial order and with thermal gradients until cooling is complete. The other is that different materials have different integrated thermal contractions going from room temperature to the base temperature of 4.2K.

The first problem is almost entirely unavoidable, but fortunately also of little importance. The second problem is complicated, but can be alleviated by proper design rules. First of all, the main

structure of the sample holder must be made in as few pieces as possible, and all of them in the same material. Furthermore, when mounting the optical parts sensitive to misalignment that are also of different materials, one should also try to fix them so they contract towards a symmetry axis. Finally all materials with non-isotropic thermal expansion coefficients should be avoided.

Another important problem is the sample mounting. The sample needs to have electrical connections in a wide range of temperatures. This requires a system, that will maintain electrical connections while contracting. Additionally, the thermal connection between the sample and the sample holder must be reproducible between coolings from room temperature to 4.2K.

3.2 Quenching and thermometry

An essential part of any Kibble-Zurek experiment is the method of controlling the phase transition. As the measurements are statistically based, it is necessary to be able to produce almost identical phase transition parameters for a large number of repetitions. In addition, the parameters - and in particular, the rate of change in the controlling transition parameter - need to be measurable with great accuracy. In the projects involving superconducting systems, the only employed controlling parameter used is the temperature. As described in Sec. 3.1.3, the cooling rate needs to be varied over several orders of magnitude in order to obtains credible scaling results. This is an additional challenge to the thermometry solution chosen.

3.2.1 Heating

Controlled, repeatable heating of the sample is of great importance to the measurements. Even though defect production happens in the cooling phase of the thermal cycle, the basis of a uniform temperature and variable cooling rate is formed by the method of heating.

Resistive

The simplest method of heating in a cryogenic environment is to pass current through a resistor. The power as well as the total energy dissipated is well-defined, as is the position of dissipated heat. An additional benefit of resistive heating is the relatively large powers available.

An important factor in the cooling part of the cycle is uniform temperature. In order to obtain this using resistors, they must be placed in such a way, that any non-uniformity arising during the heating, must have equilibrated before cooling starts.

One obvious solution is to attach the resistor to a fairly large heat capacitance, and place the sample on the other side. This solution has been tested, and works very well, but is limited to slow cooling rates because of the large heat capacitance.

Another solution is to place multiple resistors with negligible heat capacity in a symmetrical way around the system being studied. This allows for very uniform heating without introducing the limitation of large heat capacities into the thermal system. This is the main work-horse of the heating system used in this project. It offers great versatility as well as repeatability, and measurements and simulations indicate, that any non-uniformity of the temperature in the heating phase is smoothed out before entering the cooling phase.

The main problem with resistive heating is the magnetic coupling to the superconducting sample. In order to minimize the heat capacity, the resistors are simply resistive wires evaporated directly onto the silicon sample along with the superconducting material. This places it in very close proximity to the magnetically sensitive system. In order to avoid induced magnetic fields in the experiments, the resistors must be physically disconnected during the cooling phase. The disconnection can be problematic, as the relays have a minimum switching time on the order of 10-20 ms. This sets a lower limit of heating pulse lengths for this system. In addition, the magnetic field from the heaters couples to the field-generating coil circuit. The coil circuit works as a damped oscillator, which means, that the magnetic field will oscillate for a short time after the heating is turned off. Thus, the system needs to be heated to a temperature so high above T_c, that the oscillation has time to die out before the phase transition.

The final design for the Josephson experiment includes 2 integrated 50Ω resistors on the sample placed in either end, as far from the superconducting areas as possible. The resistance have some dependence on temperature, so the specified resistance is that at 4.2K. At room temperature, the measured resistance is approximately 85Ω. For the single-ring experiment, only a single resistor is included on-chip for reasons of limited sample area. It is mostly meant as a fail-over, as the design goal is laser heating for these samples.

Laser

Another choice for heating could be radiation heating, the simplest of which being laser heating mediated by optical fibers. The obvious benefits of laser heating is very well-defined heating pulses, the option of extremely high power/low pulse width and continuous tuning of the heating power. More subtly, the laser heating has the advantage of being free of coupling to the field coil system. In addition, there are no electrical connections close to the sample, which reduces electrical noise, and its induced magnetic field.

Laser heating is, however, somewhat more complicated to incorporate into the current setup. It requires optical fibers to be drawn from the room temperature laser diode to the cryogenic sample. Optical fibers are not necessarily stable at cryogenic temperatures, and reduced transmission has been measured. The wavelength of the heating laser must also be chosen to match the sample absorption spectrum. It is very hard to get absorption in the niobium itself because of its reflectivity, but the silicon can be heated by choosing a suitable wavelength. Indirect, exchange-gas mediated heating could also be performed by laser heating an absorbing target in close proximity to the sample.

3.2.2 Thermometry

In the project, two main methods of thermometry have been used, depending on the relevant time scale of the heat signal. The germanium resistor is a calibrated thermometer from LakeShore Cryotronics (model GR-200A). It is used as the reference temperature of this system for slow quenches.

The goal of the thermometry part of the setup is to determine the cooling rate, as the sample cools through the superconducting phase transition temperature. This happens at $T_{c_{Nb}} = 9.2$K and $T_{c_{NbN}} \approx 13.4$K for Nb and NbN respectively. In case of very slow cooling, the germanium

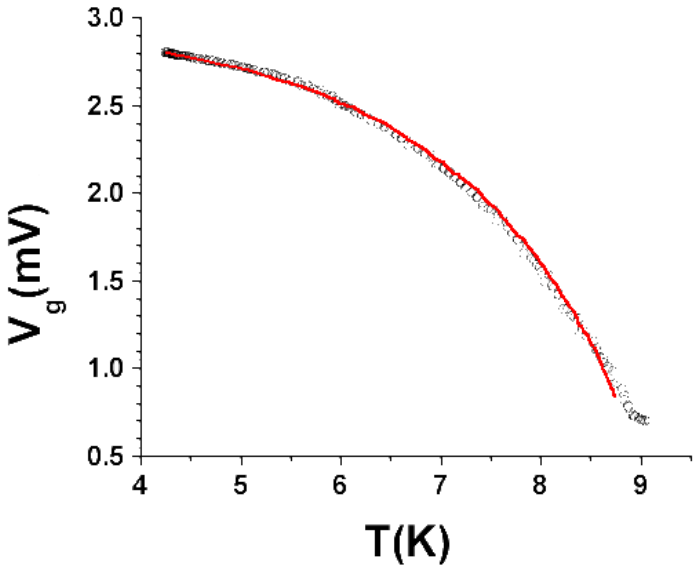

Figure 3.1: The temperature dependence of the gap voltage V_g. The open circles are the experimental datawith the junction biased at 25% of the total current jump at the gap voltage; the solid line is the prediction that follows from Eq. (3.3). The fit yields $T_c = 9.12 \pm 0.04$K and $V_g(T = 0) = 2.89 \pm 0.02mV$[24].

reference thermometer can give the temperature, and thereby its derivative, directly in the entire range of temperatures. However, for fast quenches, where the Josephson thermometer is needed, the temperature cannot be measured directly at the phase transition, as the Josephson effect is not established yet. In order to apply this method, a model for the temperature decay of the sample must be used to extrapolate back to the phase transition temperature.

Germanium resistor

For very long timescales, a calibrated solid-state germanium resistor is used. The germanium resistor consists of a piece of germanium with two leads in each end. The resistance, measured in a 4-point measurement to avoid the effect of contact resistance, is a strongly decreasing function of temperature in the temperature range used (3-20K). As a standard thermometer, this has also been used to calibrate the Josephson thermometer described below, and at the same time verify the Thouless equation[45] relating the gap-energy, Δ, and thereby the Josephson gap voltage, to the temperature. The measurements are shown in Fig. 3.1[24].

The main limitation of using this type of thermometer for Kibble-Zurek measurements on a small scale is the heat capacity associated with the thermometer and its mount. In order to ensure, that the temperature at the thermometer is the same as at the site of the sample, it is necessary to place the thermometer fairly close by, but still far enough from the heating to avoid

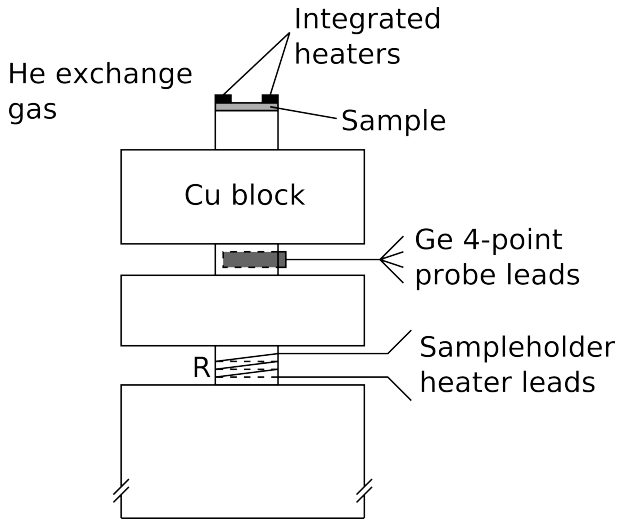

Figure 3.2: Schematic drawing of the heating system of the sample holder as well as the position of the thermometer.

thermal gradients across the thermometer. The mass of the germanium thermometer used in this setup (LakeShore GR-200A) is 395mg according to specifications[1]. In addition to this, is the thermal contact grease and metal mount needed to ensure good thermal contact. Optimistically, the total system could be as little as 1g in mass. In the setup used here, the mass of the sample holder with the thermometer mounted is in excess of 50g. When comparing this to the mass of the silicon sample of approximately 25μg, which is where the heat is dissipated, it is obvious, that thermal equilibrium at the phase transition is only attained for quite slow cooling rates. Experimentally, this is only achieved when using a heater mounted on the sample holder (see Fig. 3.2), rather than the integrated resistors on the sample itself. Comparing the readout of the germanium thermometer to the Josephson thermometer described below, they coincide only for quench times in excess of a few seconds.

Another important thing to note, when using the solid-state Ge thermometer, is that it must be disconnected at the time of phase transition. If this is not done, the bias current of the resistor will generate a (very small) magnetic field in the area or the system undergoing the phase transition, thus breaking the symmetry. Even worse, most digital multimeters, such as those used for determining the resistance of the Ge thermometer (in the case of this setup, HP 34401), will use pulsed measurements, implying that any generated magnetic fields will be of unpredictable magnitude and sign.

Josephson thermometer

The superconducting gap energy, Δ, and thus the gap voltage of a Josephson junction, is strongly dependent on temperature[45]

[1] http://www.lakeshore.com/temp/sen/gtrdts.html

$$\frac{\Delta(T)}{\Delta(0)} = \tanh \frac{\Delta(T)}{\Delta(0)} \frac{T_c}{T} \approx \left[1 - \frac{T}{T_c}^4\right]^{\frac{2}{3}} . \tag{3.3}$$

Comparing this with the calibration performed using a solid-state germanium resistor thermometer, one obtains the fit seen in Fig. 3.1. The measurements were done in fixed current-bias mode, with the bias current fixed at 20-25% of the total gap current jump on an Nb-Al/AlOx-Nb junction. From these measurements it is obvious, that the Josephson junction itself is a very sensitive thermometer at temperatures close to the transition temperature, which is where it is most needed for Kibble-Zurek experiments. Furthermore it can be seen, that at temperatures above 8.5K it is no longer useful for thermometry, as it saturates to a value determined by the normal-state resistance multiplied by the bias current.

The advantage of the Josephson junction thermometer compared to the solid-state thermometer is, that it is a localized thermometer, at the place the transition takes place, and also its very fast response. The temperature of the system is reflected in the gap voltage on a time scale limited only by the thermal relaxation of the sample itself. The detection of this voltage temporal response is almost entirely limited by the signal filtering of the amplifiers and data acquisition system attached to measure the voltage change. The sensitivity is determined by the noise of the detection system, which is dominated by the noise of the current supply for the constant current bias, as well as the voltage resolution of the data acquisitions system. Typically, this was done using a fast digital oscilloscope with a voltage accuracy of about 2μV directly attached to the voltage wires of the junction 4 point probe. This gives a maximum resolution on the temperature of

$$\delta T = \frac{dT}{dV_g} \delta V_g \approx 2\text{mK} .$$

A typical voltage response of the gap voltage of one of the Josephson junctions used as a function of time is shown in Fig. 3.3(a)[46], and the conversion using Eq. (3.3) to temperature in Fig. 3.3(b). As the Nb Josephson thermometer is only useful for $T < 8.5$K, it is necessary to extrapolate the temperature back to the transition temperature at 9.2K. To do this, a model of the thermal relaxation is needed. There are two available paths for heat out of the sample - the copper block to which it is attached, and the helium exchange gas around it. The simplest possible model for the heat transfer is an exponential decay of the temperature.

$$T(t) = T_b + (T_0 - T_b) e^{-\frac{\lambda_{He}+\lambda_{Cu}}{C} t} , \tag{3.4}$$

where T_0 is the temperature at the end of the heat pulse, T_b is the base temperature, λ_{He} and λ_{Cu} are the heat conductances to the helium exchange gas, and the copper block, respectively, and C is the heat capacity of the heated volume. Fitting the $T(t)$ data obtained from the $V_g(t)$ data using Eq. (3.3) to the form of Eq. (3.4), it is possible to extrapolate to $T = T_c$ and get the cooling rate at this point. As is seen in Fig. 3.3(b), the fit is exceptionally good, implying that the simple exponential decay models thermal relaxation in the system very well. Through varying the exchange gas pressure, it would be possible to find λ_{He} and λ_{Cu} individually, but as they are both uniform, although on opposite sides of the sample, and only the sum matters for thermometry purposes, it is not necessary.

3.2.3 Obtaining different cooling rates

In an exponential decay, the decay rate is simply proportional to the temperature gradient and the heat conductivity, while inversely proportional to the heat capacity. For the quench time, τ_Q this means

$$\tau_Q = T_c \left(\frac{dT}{dt}\bigg|_{T=T_c} \right)^{-1} \propto (T_c - T_b) \frac{\lambda_{He} + \lambda_{Cu}}{C} \,. \tag{3.5}$$

Looking at Eq. (3.5), one ought to wonder from where the experimentally available range of cooling rates comes. Naively, all the variables determining the cooling rate are determined by geometry, and as such should not be able to change appreciably without physical modification of the sample holder. Regardless, several decades of cooling rates have been obtained using this setup. At first glance this seems to be an indication, that the simple exponential decay approximation cannot be valid, but all experimentally obtained temperature curves, like in Fig. 3.3(b), fit extraordinarily well.

The only explanation consistent with the experimental facts of both exponential decay and a wide range of available quench times is that the value of $\frac{(T_c - T_a)}{C}$ can be changed by changing the heating parameters. This can be understood by comparing two different heating cycles, that deposit the same energy in the sample, but at different powers. It is assumed, that both cycles make the temperature rise above T_c. For a short, powerful heating pulse, the heat is dissipated so

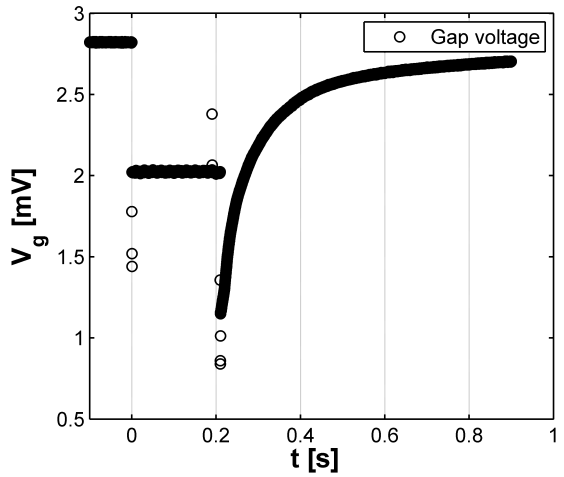

(a) Gap voltage as a function of time, $V_g(t)$

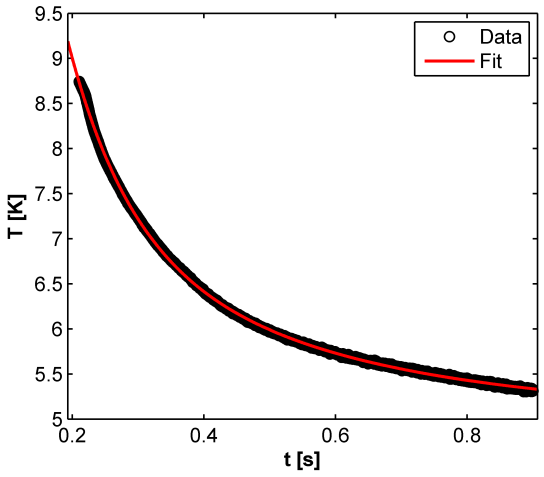

(b) The corresponding temperature as a function of time, $T(t)$

Figure 3.3: Typical measurement results of the Josephson thermometer. The measured quantity is the gap voltage, measured with a constant current bias at approximately 25% of the total current jump at the gap. For this particular measurement, the pulse width is 200ms, the pulse height is 2V and the fit yields $\tau_Q = 0.32$s. The data shown was obtained by Mads Rolf Kjær Jensen on cantilever-type samples, reproduced with permission.

quickly, that only the surface of the sample heats up. Very good heat conduction in the silicon of the sample at temperatures close to T_c quickly equilibrates the temperature in the entire sample, before the temperature falls below T_c (for a discussion of thermal gradients, see Sec. 3.2.4). After this, the heat leaves the sample in an exponential decay through the coupling to the copper block and the helium exchange gas. For a long, low-powered heating pulse, the heat is distributed in the sample, but also over time in the close neighborhood of the sample, until the heating period is over. After this, the entire heated volume must cool through its coupling to the surroundings. This means, that the relevant heat capacity is no longer the heat capacity of the sample itself, but rather of a larger volume, which can easily be orders of magnitude larger. In addition, the surrounding temperature for the sample is no longer the heat bath temperature of LHe (4.2K), but in stead some higher value corresponding to a heated neighborhood.

Another way of changing the cooling rate is to change the heat conductances, λ_n, in Eq. (3.5). The heat conductance to the copper block can be changed by adding thin layers of teflon(PTFE), which have a low heat conductance, between the sample and the copper block. This has the disadvantage of requiring reheating of the entire sample holder to change it. Another less invasive way is to change the helium exchange gas pressure in the cryoprobe. This will change the heat conductance of the gas, λ_{He}, and thereby the quench time, τ_Q. Such an experiment was done using the standard 500μm annular overlap junction as a thermometer, and varying the exchange gas pressure by controlling a valve on the pipe between the cryoprobe vacuum and a room-temperature helium gas balloon. The pressure was measured using a standard pressure meter close to the valve at room temperature. The result of this test is seen in Fig. 3.4. The quench time is varied by a factor of 5 by changing the exchange gas pressure from 0.03mbar to 30mbar, with the main change happening close to the lower limit. Above 30mbar no significant change is seen. As this change is very weak compared to the necessary orders of magnitude of change needed for Kibble-Zurek measurements and experimentally harder to adjust than the heating parameters, it was not exploited during measurements. For all measurements in this work, an exchange gas pressure of approximately 7mbar was maintained.

The exchange gas pressure in the cryoprobe was however used as an alternative thermometer during the initial cooling of the sample holder at the beginning of each series of measurements. The exchange gas pressure in the cryoprobe was adjusted to approximately 450mbar at room temperature before cooling, and was monitored during the cooling period of approximately one hour. This provides an easy, non-invasive, although non-linear, way of monitoring the temperature during the initial cooling of the cryoprobe. This is important, as no electrical connections can be allowed in this period to protect the superconducting shields from fields during their individual transitions. When the pressure reaches its 4.2K value of about 7mbar, the cooling is complete, and the electrical connections to the junctions can be tested before experiments commence.

3.2.4 Thermal gradients

As seen in Eq. (3.5), τ_Q is determined from the coupling to the environment through the heat conductances, and the heat capacity of the heated volume. However, as described in Sec. 2.3.4, an essential part of any experimental setup for Kibble-Zurek measurements, is ensuring that only very small thermal gradients are present across the system at the time of transition. According to Eq. (2.16), the maximum allowed thermal gradient for a Josephson junction experiment is given

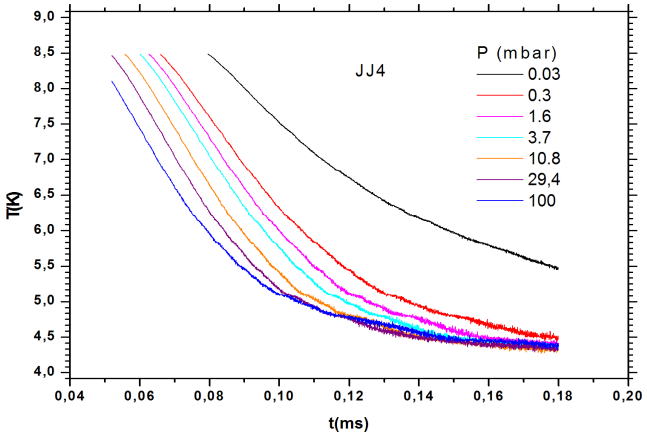

Figure 3.4: The temperature response of the sample with different exchange gas pressures. It is seen to be strongly dependent on the gas pressure at low pressures, but saturates at high pressures. The heating was done resistively and with identical voltage pulses. The cooling rate varies by a factor of approximately 5 in the range of pressures used.

by

$$|\nabla T| = \frac{\left|\frac{dT}{dt}\right|}{v_{T_c}} = \begin{cases} \frac{\left|\frac{T_c}{\tau_Q}\right|}{\bar{c}_{nn}} & \text{for revised JTJ theory} \\ c_0 \left[\frac{\tau_0}{\tau_Q}\right]^{\sigma} & \text{for GL-based theories ,} \end{cases} \tag{3.6}$$

where $\bar{c}_{nn}$ is the normal state wave phase velocity in the Josephson junction transmission line, and c_0 is the zero-temperature speed of information. According to [33], $\bar{c}_{nn} \approx 7 \times 10^3 m/s$, which corresponds to a maximum allowed thermal gradient on the order of 1 K/m. Using the Swihart velocity of the original description in Sec. 2.4.1, the value is decreased to 30 mK/m, and for a superconducting ring to about 1 mk/m. In the superconducting ring case, c_0 is set to the speed of light in vacuum, 3×10^8 m/s, as a worst-case estimation.

Simulations

Both experimental setups in this project are planar, so the most important thermal gradient to investigate is the one on the surface of the sample substrate. As both the thermal conductivity[2][47] and the heat capacity[3][48] of the Si substrate of the sample is strongly dependent on temperature in the temperature range of interest (see Fig. 3.5), and the dependence is nonlinear, the simplest way to investigate thermal gradients is to go to simulations. From Fig. 3.5 it can be seen, that thermal gradients will be an increasing problem with increasing phase transition temperatures, if using Si as a substrate, because the time constant of equilibration is approximately inversely proportional to the ratio λ_{Si}/c_p, which is also plotted.

[2]For data, see eg. Engineering Fundamentals, www.efunda.com
[3]http://hyperphysics.phy-astr.gsu.edu/hbase/solids/phonon.html

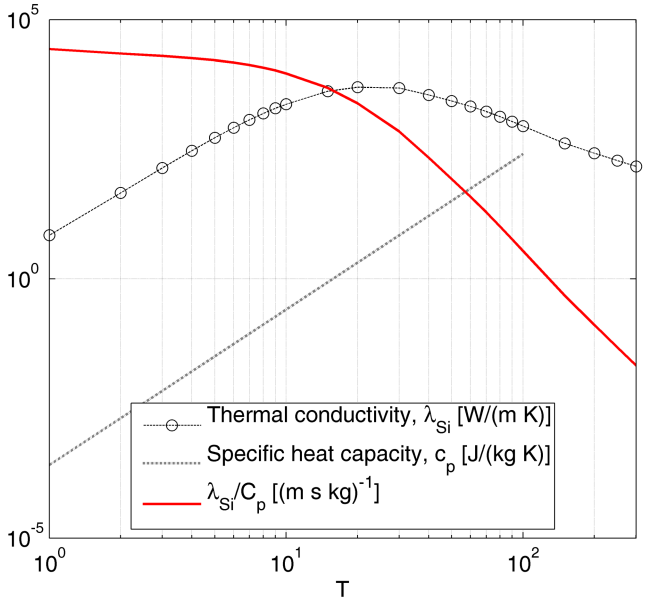

Figure 3.5: Material parameters of crystalline silicon at cryogenic temperatures. The heat capacity is found using the Debye model, and the thermal conductivity is tabulated. The time scale for equilibration of a system is proportional to the ratio given, but geometry must be factored in to give a real time. Note the logarithmic axes. Data from [47, 48].

The results presented in this section were obtained using Comsol Multiphysics, a commercial finite-element modeling package. The simplest approach to finding the minimum time required for the sample to equilibrate is to simulate a system consisting of only the isolated sample, where one half is heated to a higher temperature, eg. 30K, and the other is kept at base temperature. The first reasonable guess at a time scale of equilibration is simply the time constant of the approximately exponential decay towards the equilibrium value of the temperature in the two halves. The result of this fairly simple simulation is shown in Fig. 3.6(a). The time constants for the rising and falling parts of the sample are slightly different, but are both on the order of μs. This simulation ignores heat transfer away from the sample, which tends to increase uniformity of temperature, and could provide non-uniformity closer to equilibrium, depending on how well the surroundings can be modeled as a heat bath. Insofar as the time constant of the cooling of the entire sample in experiments is much greater than the time-constant of chip equilibration, the sample can be well approximated as being in thermal equilibrium with itself, and thus have negligible thermal gradients. The lowest attained τ_Q in experiments is slightly below 1 ms. A plot of the temperature (color-coded) 0.3μs after the start of the simulation is shown in 3.6(b). It is meant simply as an intuitive view, so the actual temperature scale has not been included for simplicity.
However, as the total system with the sample coupled to both the copper sample holder and the helium exchange gas is significantly more complicated, a simulation on the total solid system was performed as well. In order to simplify computations, the exchange gas cooling was ignored. In experiments, it has been shown that the exchange gas is not essential to performing experiments,

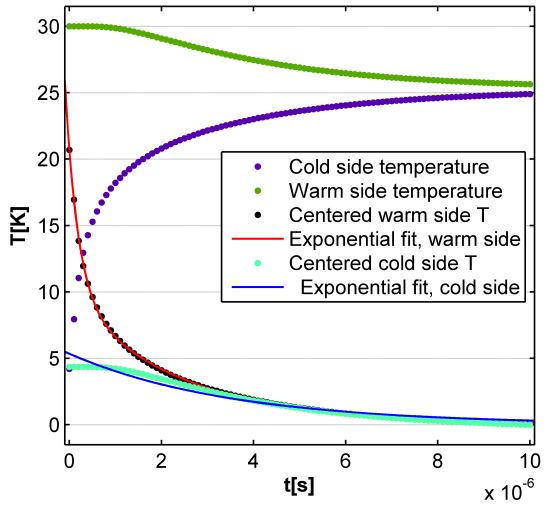

(a) The temperature as a function of time 0.2mm from each end of the sample.

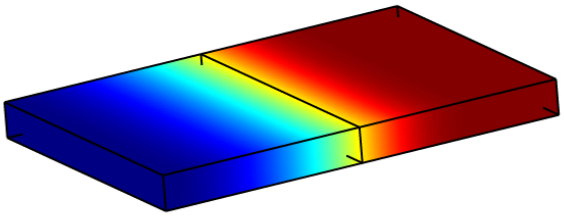

(b) Color-coded view of the sample 3μs after start of simulation. The warm end is 30K and the cold end is 4.2K.

Figure 3.6: Results of the simplest simulation approach to finding the equilibration time of the sample. In (a) the centered lines represent the same data, only having subtracted the final value and multiplying the lower branch with -1 to bring it into the same quadrant.

although it is impractical to avoid it entirely, and in any case, any exchange gas cooling will be uniform over the exposed area and thus tend to minimize thermal gradients. As such, this simulation should be thought of as a more realistic worst-case scenario, than the one above. In this simulation, the entire heating-cooling cycle is implemented, and the heating is modeled as resistive heating comparable to the ones found on the actual samples. The parameters for the simulation is the heating pulse height and width, thus providing an intuitive coupling to the experimental observations. The results of one run of this simulation are shown in Fig. 3.7. From the inset in Fig. 3.7(a) τ_Q can be estimated to be 10ms, and the thermal gradient present between the minium at the center of the chip and the maximum below the heating element to be approximately 3mK/m, which is close to the limits predicted by Eq. (3.6). The expectation from this simulation is, that the minimum τ_Q used in experiments is very close to the limit of the cooling setup in terms of providing low enough thermal gradients to not interfere with the phase transition dynamics.

The attainable range of cooling rates in the simulations were within the same order of magnitude. Therefore it must be concluded, that the simulated model system is still too simple to account for the full range of available quench times found in experiments. Possible candidates for the origin of the large range of quench times are the coupling of the sample to the copper sample holder, exchange gas interactions or a different heat conductivity to heat capacity ratio of the copper used in the sample holder. Regardless of the lack of the full range of quench times in the simulation, it seems to give a good picture of the system during cooling in the quench time ranges obtained. Here it fits with experimental data, and it can be used to estimate temperature gradients across the sample.

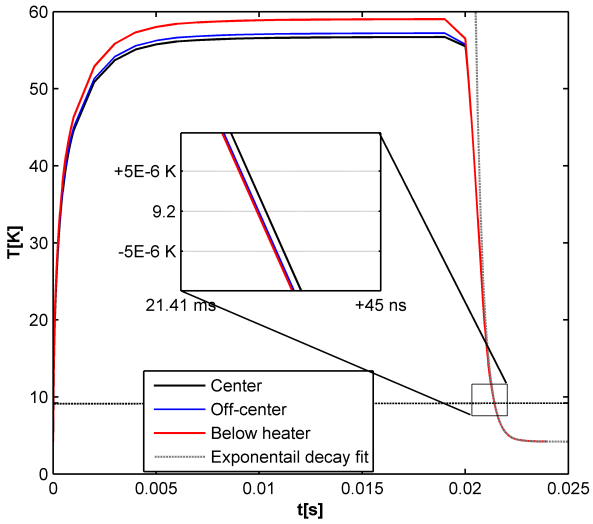

(a) The temperature at three points in the sample surface as a function of time for the total solid system simulation. The three points are in the center of the sample, just under the heater and halfway between the two. The inset shows the area close to the transition magnified.

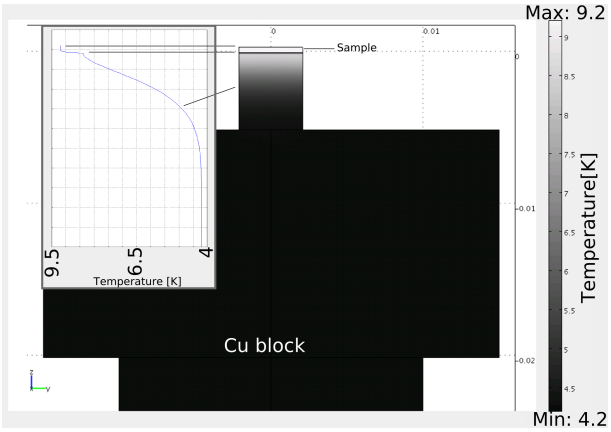

(b) Color-coded view of the top of the simulated sample holder at the transition time. The inset shows the temperature distribution on a line vertical from the sample center.

Figure 3.7: Graphical representation of the results of the 'full' simulation. The applied heating pulse is 4V in height and 20ms wide, and has been applied in parallel to the two heaters.

3.3 Josephson Junctions

The main results of this project has been obtained by thermally quenching Nb-Al/AlOx-Nb Josephson junctions. This section is dedicated to describing the experimental setup for detecting the topological defects in this system as well as similar, but alternative approaches.

3.3.1 Fluxons and the sine-Gordon equation

A *fluxon* is the topological defect in a Josephson junction structure. It is produced, when the integrated phase change over the some length of the junction is equal to 2π. Physically it describes a magnetic flux line containing a single flux quantum $\Phi_0 = h/2e$ through the Josephson junction's insulating layer, with its corresponding shielding current circulating around it. The size of a fluxon is limited from below by the junction critical current because the circulating shielding current around a flux quantum is fixed. From this, the size of a fluxon can be calculated, and this is called the Josephson correlation length, λ_J

$$\lambda_J = \sqrt{\frac{\hbar}{2eJ_c\mu_0(2\lambda_L + d_{ox})}} \tag{3.7}$$

In a Kibble-Zurek context, the fluxon is created by the causal bounds set on the system during a

fast cooling, but fluxons can have other origins, and its description predates application of Kibble-Zurek theory to solid-state systems by about 20 years. The simplest way of generating a fluxon is to simply apply a magnetic field perpendicular to a long (as compared to λ_J) Josephson junction and parallel to the film surface. In order to generate a fluxon in the junction, it is necessary to apply a magnetic field larger than threshold magnetic field of the junction, called the critical field of the junction[36], H_c

$$H_c = \sqrt{\frac{32\hbar J_c}{\pi e d_{ox}}}\,, \tag{3.8}$$

where J_c is the critical current density of the junction, e is the electron charge, and d_{ox} is the insulator thickness. However, this fluxon is not stable, and disappears as soon as the magnetic field is removed. Stable fluxons can be created by cooling an annular Josephson junction in a magnetic field, regardless of the cooling rate.

The reason, that the annular Josephson junction is a good system for testing the Kibble-Zurek mechanism, is twofold. First of all, the production technology of Josephson junctions is very mature (see 3.3.5), which leads to very uniform and reproducible junction parameters. Secondly, the fluxon carries a topological charge, and can therefore be counted explicitly.

Once the fluxon has been created, its dynamics is described by the sine-Gordon equation

$$\beta\phi_{xxt} + \phi_{xx} - \frac{1}{c_0}\phi_{tt} - \alpha\phi_t = \sin\phi\,, \tag{3.9}$$

where subscripts indicate partial derivatives, c_0 is the waveguide (Swihart) velocity[49, 50], α describes the dissipation due to quasiparticles, β is due to surface impedance[51] and ϕ is the Josephson phase. Please note, that α is not related to the α of the Ginzburg-Landau theory used in Chap. 2. It is so named by tradition, and so also here. Technically speaking, the pure sine-Gordon equation does not include the dissipative terms, and for most of the applications in this work it is disregarded because of the quality of the junctions.

If a tunneling current in the junction is present, this will exert a force on the fluxon through the Lorentz force, thus accelerating it. When ignoring the dissipative terms (setting $\alpha = \beta = 0$), the mass of a fluxon is equal to zero, and the friction disappears. As a result, the equilibrium velocity of the fluxon under force is c_0, and the acceleration time can be ignored.

3.3.2 Junction internal resonances

In addition to the sine-Gordon equation, the Josephson junction is governed by the Josephson relations[51]

$$V(t) = \frac{\hbar}{2e}\phi_t \tag{3.10}$$

$$I(t) = I_c \sin(\phi(t)) \tag{3.11}$$

where I_c is the critical current of the junction. From the first relation, it can be seen that a constant ϕ_t corresponds to a constant voltage. If a fluxon is subject to a Lorentz force by the application

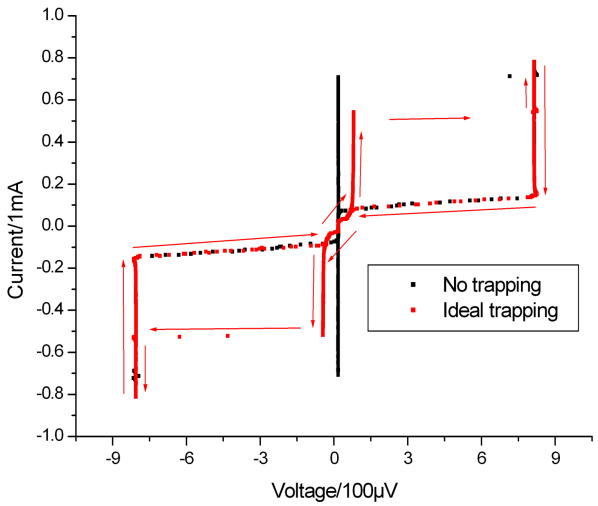

Figure 3.8: Plots of raw data for DC IV curves of an annular junction with no trapped fluxons (black) and one trapped fluxon (red). Note that the amplifier for the voltage saturates at approximately 800μV. The voltage of the step is approximately 65μV. The direction traversed in time is shown by arrows.

of a current through the junction, it will begin circulating around the junction. This results in a finite value for ϕ_t, which corresponds to a finite voltage across the junction. Insofar as the approximations in the preceding section of $\alpha = \beta = 0$ is correct, the resulting voltage will be constant as the limiting maximum speed of the fluxon is reached immediately, for arbitrarily small forces. The extent to which this is true, is an indication of the validity of the approximation. In Fig. 3.8, two obtained DC IV curves are plotted in the same coordinate system for comparison. One shows the normal case with no fluxons trapped, the other for one fluxon trapped. It is seen, that the approximation is quite well fulfilled, as the voltage of the steps in the red curve is almost independent on the current. The data in this plot was obtained using a current sweep with a frequency of approximately 1 Hz. The resistive part of the IV curve at large voltages is usually not probed, as it is irrelevant for the Kibble-Zurek related experiments. The small tail of the voltage steps towards the center is an indication that the motion is not frictionless and the fact that the critical current does not go to zero shows that there is some small fluxon pinning in play[52]. The friction is to be expected, simply from the fact that the IV curves are recorded at fairly high temperatures - approximately 6K. This is done to increase dissipation and thereby stabilize the voltage steps for recording. The dissipation is increased at higher temperatures because the quasiparticle density increases.

The internal resonances are very similar to zero-field steps in long linear Josephson junctions. They have also been described as the Fiske steps of long linear junctions with a self-supplied magnetic field[53]. In the literature, the internal resonances of annular junctions are called both Fiske steps, as they have the same voltage as a Fiske step in a long junction with length equal to

the circumference, and zero-field steps as they do not require the application of external fields to be visible[54].

From Fig 3.8 it is clear, that it is possible to detect the presence of a trapped fluxon by looking at the DC IV curve of the junction. Unfortunately, this method does not allow for discriminating fluxons from antifluxons. There are other ways of obtaining this discrimination in the system, however - see [41] and Sec. 3.3.3.

The predicted value for the step voltage can be found from using the reciprocal period of a fluxon circulating around the annulus as the frequency input to the Josephson relation, Eq. (3.10). This means setting $\phi_t = 2\pi\frac{\bar{c}}{C}$, where $\bar{c}$ can be found as

$$\bar{c}^2 = \frac{c^2}{\varepsilon_r(1 + 2\lambda_L/d_{ox})}\,, \tag{3.12}$$

where ε_r is the dielectric constant, λ_L is the London penetration depth, and d_{ox} is the oxide barrier thickness. For the 500μm annular overlap junctions with a single fluxon this makes $\phi_t \approx 4.5 \times 10^{11}\mathrm{s}^{-1}$, which means that the predicted voltage of the first zero-field step is

$$V_{ZFS1} = 140\mu V\,.$$

However, the relation is normally applied in reverse, to determine the Swihart velocity, $\bar{c}$, when the position of the step is know from experiments, as typically, the values of d_{ox}, λ and J_c are hard to control precisely during production. Therefore some deviation from the above should be expected.

3.3.3 Magnetic field dependence

In addition to detecting the resonance voltage steps, fluxons can be detected by looking at their effect on the dependence of the junction critical current on applied magnetic field. As described in Sec. 3.3.2, the introduction of a fluxon into a junction reduces the zero-field critical current to approximately zero. This is true, as long as the number of fluxons trapped is greater than zero. Furthermore, the location of the first maximum in the critical current as a function of applied field is set by the number of fluxons trapped[53]. This detection is, again, unable to distinguish between fluxons and anti-fluxons.

A variant of this technique adds the ability to distinguish these. If a transverse magnetic field is used, the induced screening currents will induce a parallel (to the junction electrodes) magnetic field threading the junction. The fluxon is essentially a magnetic dipole, and will be affected by a force trying to align it to this magnetic field. Thus to a first approximation, an applied field will tend to pin the fluxon to a specific point on the junction circumference, where the fluxon is aligned with the field. The strength of this pinning is proportional to the magnetic field strength at this point. The point at which the pinning force on the fluxon is equal to the Lorentz force of the applied current gives the critical current needed to break out the fluxon and push it onto the zero-field step dissipative movement. The pinning force is given by the gradient of the potential. So far, this is equally true for all junctions, and all magnetic field orientations, only limited by the assumption that the field is small - meaning small enough to not introduce fluxon-antifluxon pairs in the junction by itself. This limit is the critical field of the annular junction, and approximately coincides with the first maximum of the critical current when one fluxon is trapped.

If the junction geometry is reflection symmetrical, the induced magnetic field will also be symmetric, and so will the fluxon pinning potential at the equilibrium position. This is the case for the pure Lyngby geometry, as seen in the top right insert of Fig. 3.9. However, if the geometry has a reduced symmetry, the pinning potential could be different for the equilibrium position of the fluxon and the antifluxon, even for the same externally applied field. An example of this, is the geometry shown in the top left insert in Fig. 3.9. The corresponding radial magnetic flux density, obtained from magnetostatic simulations described in Sec. 2.5, are figured in the main plot as a function of angle. The angle is measured from the part of the annulus furthest into the bottom electrode for the annular geometry, and from one of the two points on the annulus on the center of the electrodes, for the Lyngby geometry. The result of different pinning potentials at the equilibrium positions of the fluxon and antifluxon is a difference in the measured critical current at a specific externally applied field strength. The magnetic fluxon pinning strength is proportional to the radial magnetic flux density from the external field.

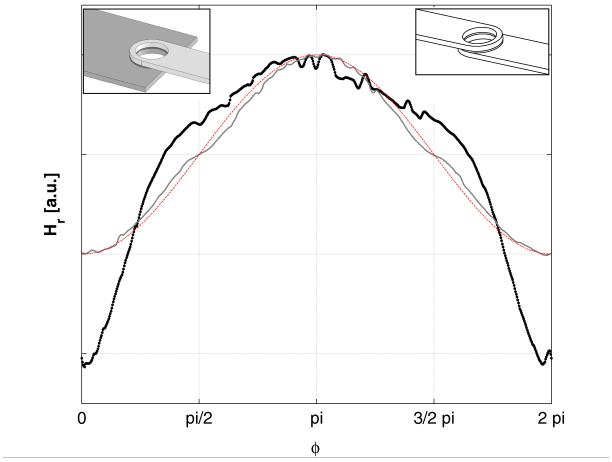

Figure 3.9: Two different annular junction geometries resulting in two different magnetic pinning potentials of fluxons. The plotted data is obtained from magnetostatic simulations. The annular overlap geometry to the top left corresponds to the thick black line, and the Lyngby geometry, corresponding to the gray line, is shown in the top right inset. For comparison, a simple cosine is drawn as well with a thin, dotted red line. The magnetic field scale has been normalized to the maximum value for comparison, as only the dependence on the angle ϕ is important.

If the field is reversed, the equilibrium points of the antifluxons become the equilibrium points of the fluxons, and vice versa. This means that if the antifluxon is strongly pinned at $H = H_{max_1}$, it will be more weakly pinned at $H = -H_{max_1}$. The result is a magnetic field dependence of the critical current, that is not symmetrical. It is obvious from Fig. 3.9, that the pinning is significantly stronger in the side of the annulus furthest into the bottom (rectangular) electrode, and thus an asymmetric dependence of the critical current on the applied external field is expected. From this asymmetry, it is possible to distinguish fluxons and antifluxons. The description is particularly intuitive for very long junctions in which fluxons are essentially point-like, and can be considered simply as a particle in a potential well. The prediction has also been done in a quantitative way

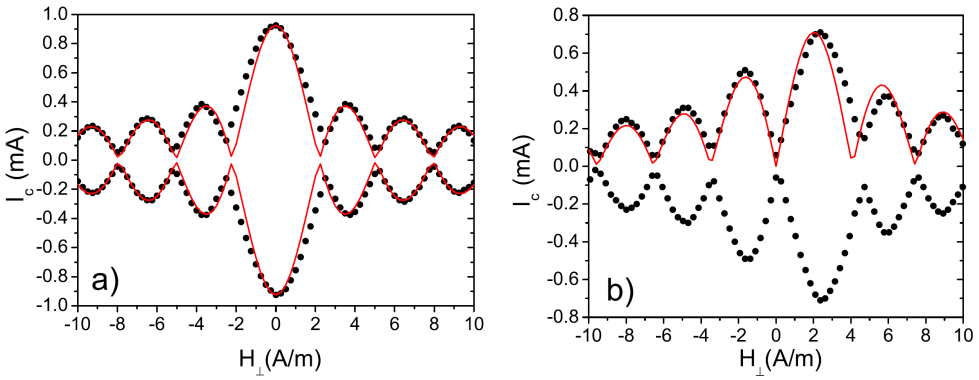

(a) No fluxon trapped (b) One fluxon trapped

Figure 3.10: The predicted and measured $I_c(H_\perp)$ dependence in an annular overlap Josephson junction. The prediction is made from magnetostatic simulations on the annular overlap geometry. The asymmetry is evident when one fluxon is trapped, and in the case of an antifluxon, the picture is simply mirrored around $H_\perp = 0$. Reproduced from [41]

from simulations[41] and compared to measurements in annular overlap junctions, and can be seen in Fig. 3.10.

Strictly speaking, a perpendicular field is not needed to have asymmetric fluxon magnetic pinning potentials in an annular junction. It is enough with a strongly non-uniform magnetic field aligned along the electrodes. However, the uniformity must be very strong indeed, to have significantly different magnetic flux density on different sides of a ring a few hundred μm across.

In [55] the authors also demonstrate an additional pinning mechanism of magnetic origin, that could be used to explain the observed fluxon-antifluxon differentiation, based on Abrikosov vortices trapped in junction electrodes. However, this mechanism is either limited to fast quenches (for trapping Abrikosov vortices by the Kibble-Zurek mechanism) or individual junctions (defects in the electrode produces pinning centers). In the first case, this should not be reproducible from quench to quench, as trapping is not dependent on space coordinate, and most importantly be very similar in the Lyngby and annular overlap geometries, which is not seen. In the second case, this effect relies on pinning centers produced by critical current density modulation because of barrier thickness variations, or on pinning centers because of magnetic micro defects. The first can be dismissed, as the effect is very small for low-current density junctions as the ones used in this project, and because the critical current dependency on magnetic field is very close to ideal. The second can be dismissed by showing the same effect in several samples and by looking at the residual critical current for an annular junction with one fluxon trapped. If the critical current is reduced to zero, any permanent, static pinning centers can be ruled out. All of the above discriminators are present in the data, and so the magnetic fluxon pinning as described this section seems the best explanation fitting the data.

The drawback to using this method for detecting fluxons, is that it is somewhat slower. As it requires the detection of a threshold value in current-biased mode, it is necessary to continuously modulate the bias current and detect at which point the voltage becomes greater than zero. This

needs to be done for every value of the magnitude of the applied magnetic field needed in the plot. If trapped flux in the films of the electrodes can be ignored and trapping probability is low (so multiple trappings are negligible), it should be possible with only three values of the magnetic field; $H_{appl} = [-H_{c1}, 0, H_{c1}]$. This is because the only available states of the annular junction are the ones shown in 3.10(a), 3.10(b) and 3.10(b) mirrored. The result of this is that the data acquisition time would be approximately increased by a factor of three, as effectively three different IV-curves would need to be obtained for each quench. This is only reasonable, as long as the junctions used exhibit the characteristic dependence of the critical current versus applied magnetic field, which is the case for fairly slow quenches, where Kibble-Zurek trapping in the films is suppressed.

3.3.4 Josephson junctions in oblique fields

Another feature under investigation in this project is the modulation of the critical current when subjected to magnetic fields in different directions. This is used as a measure to indicate the general sensitivity of the junction to a magnetic field in different directions. The interest of our group in this field was sprung by observations in our experiments, that the modulation of the trapping probability in annular Josephson junctions of the Lyngby geometry by a transverse magnetic field, was much faster but completely equivalent to that seen by an in-plane field[40].

From the theory of Sec. 2.5, it is expected that a junction with a particular geometry, will not be equally effected by magnetic fields in all directions. Depending on geometry, there will be angles in which the sum of the effects of the perpendicular component (with respect to the junction plane) and the parallel components can cancel almost completely[42].

To investigate this effect, a sample containing Josephson junctions of different geometries was mounted inside an existing sample holder with two orthogonal field coils. The field coils were mounted so one of them had its axis directly perpendicular to the sample surface, and the other was parallel to one of the sample sides, in-plane with the junctions. Combined, these coils can create a field in a plane spanned by the two axes of the field coils, see Fig. 3.11(b). The other in-plane component can be ignored without loss of generality[42]. In addition, it is only necessary to span 180 degrees, as the remaining 180 degrees can be spanned by applying a negative current through the coils.

The resulting setup is shown in Fig. 3.11(a). By sending current through the two field coils with different amplitudes, any angle in the plane of the drawing can be selected. The two coils generally have different coil factors, especially as their individual placement in relation to the magnetic shielding is different. The in-situ coil factor of each coil can be calibrated by using samples with junctions already characterized in a different setup in the transverse and in-plane directions. When the current through each coil and coil factors are known, the field direction and amplitude at the sample is fully defined.
Measurements are performed by selecting a direction of the magnetic field by selecting a ratio of the currents in the two coils, and then scanning the sum of the currents in a wide range. For each step, the IV characteristic is recorded. Afterwards a different angle is selected and the the process is repeated. This yields a full characterization of the critical current as a function of applied magnetic field amplitude and angle.

For small rectangular junctions in an in-plane field parallel to one of the electrode edges, the dependence of the critical current on the applied field magnitude is the simple Fraunhofer

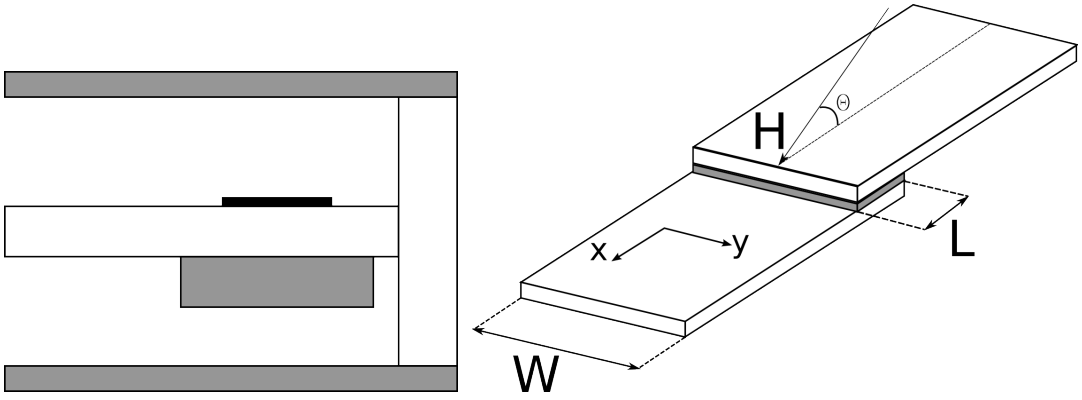

(a) Schematic of the sample holder for measuring the sensitivity of junctions to fields in different directions. The sample is black, the coils are gray, and the metal sample holder is white. The magnetic shield is not shown, but is a can outside the outer field coil. In the experimental setup, the sample holder is vertical and suspended from the left part of the metal depicted in the figure. Not to scale.

(b) Illustration of an overlap junction and the field directions available in the setup.

Figure 3.11: Schematic showing the sample holder and sample used for measuring the sensitivity of different junctions to applied magnetic fields in various directions.

pattern. The first zero corresponds to the first critical field of the junction, and can be used to characterize, among other things, the magnetic penetration depth of the electrodes. In order to measure the junction sensitivity, one could simply use the reciprocal of the first critical field as a measure.

However, when moving away from from the in-plane field or choosing different geometries, the dependence will generally change from the Fraunhofer pattern into something else. In order to be able to measure sensitivity as a function of angle, and maybe even between different geometries, a more general measure of sensitivity must be defined. In fact, for some junction geometries, there may not be a critical field at all. As a simple illustration, the critical current dependence on transverse magnetic field of a small cross junction is approximately of the form $I_c(H) \propto H^{-1}$[56], although it has been shown elsewhere[42] that for large fields, this changes into a H^{-2} dependence. By using a new value, Δ_R, rather than the first critical field as the foundation for the sensitivity, a generalized form can be found. Δ_R is defined as twice the field magnitude when the critical current has dropped by a factor of $2/\pi$ compared to its zero-field value. This rather curious choice of factor ensures that for junctions with a Fraunhofer pattern, $\Delta_R = H_{c1}$, while still being defined for arbitrary functions, $I_c(H)$[42]. A graphical illustration of the definition of Δ_R is shown in Fig. 3.12

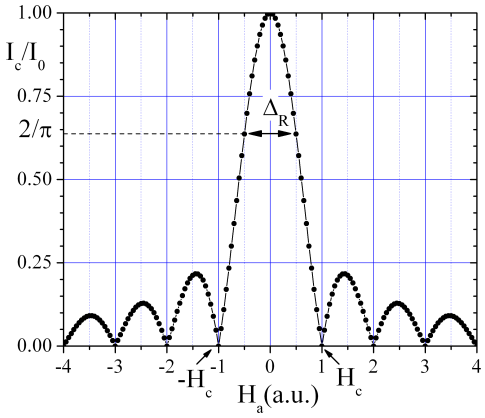

Figure 3.12: The definition of the inverse sensitivity Δ_R, as shown on a Fraunhofer pattern[42]

3.3.5 Production and effects on measurements

The samples used in this project are all based on the so-called tri-layer window junction production technology. It is based on Nb superconducting electrodes, but with a barrier made through the oxidation of a 5-20nm thick Al layer, a process first described in[57]. The process consists of several steps, which is summarily described in the following.

First, the entire Si wafer is blanket covered by RF sputtered Nb, typically 300nm in thickness. If needed, this step is preceded by deposition of an insulating layer such as silicon nitride. After this, a layer of Al in the range 5-20nm is sputtered, after which another layer of Nb between 80nm and 250nm in thickness. The junctions are defined photolithographically with a negative mask (junction areas covered by photoresist after development). The entire wafer is the subjected to either a SNAP (Selective Niobium Anodization Process) or SNEAP (Selective Niobium Anodization and Etching Process), which is a liquid anodization, which incorporates etching of the anodized Nb in one step (for the SNEAP process)[58]. The exposed areas are etched away either directly(SNEAP) or subsequently(SNAP). The entire wafer is then covered in 200nm of SiO_2 for insulation, after which the Nb wiring layer connecting to the counter-electrode is lithographically defined, using a positive mask. The exposed areas are covered in a few hundred nanometers of Nb after a short etch (iron milling or similar) to clean the counter-electrode surface to avoid the forming an additional junction.

The main advantage over alternative processing methods is the fact that all the junction-defining steps are done on the entire wafer at the same time, leaving all junctions on the wafer with almost identical properties, such as specific capacitance and critical current density. The junctions are also very well protected by anodic oxide and SiO_2, so they fare well in comparison to other junctions in terms of durability to exposure to room-air and repeated thermal cycling.

There are some technical requirements, that set some limits on the geometry that can be defined using this method. First of all, the superconducting Nb wiring layer is deposited in a blanket fashion, which is good for uniformity and step coverage, but results in some overhanging structure around the junction. The size of this is approximately 1 μm on each side because of tolerances

in the mask alignment. The region under this is called the *idle region*, and has some implications on the junction parameters. In particular it tends to slow down fluxon propagation[59].

Any junction made from a sandwich structure will also experience magnetic focusing. This is the effect of the electrodes expelling the magnetic field from their interiors to a depth approximately equal to λ_L. The effective magnetic thickness of the junction, d_e, is then

$$d_e = d_{ox} + 2\lambda_L \,,$$

where d_{ox} is the tunnel barrier thickness and the electrodes are assumed to have identical magnetic penetration. When a field is present in the plane parallel to the tunnel barrier it will have to bend to avoid the central regions of the electrode volume. This means, that the flux penetrating the junction region will be increased, by a factor determined by the ratio of the magnetic penetration depth to the total thickness of each electrode, see Fig. 3.13. Depending on the junction dimensions, the field induced by magnetic focusing may be non-uniform in the junction area because of field leakage in the perpendicular direction to the cross-section shown. Using typical parameters for tri-layer junctions, the field increase in the junction can be crudely estimated as an increase in effective cross-sectional area to the magnetic field

$$\frac{B_J}{B_0} \approx \frac{d_{ox} + t_1/2 + t_2/2}{d_{ox} + 2\lambda_L} \,, \tag{3.13}$$

where B_J and B_0 is the field with and without field focusing, respectively, and t_n is the thicknesses of the electrodes. Using thicknesses from above, including wiring layer, and Nb penetration depth of approximately 40nm, the field is seen to increase by a factor of approximately 4. However, this is probably a worst-case calculation as the penetration depth of RF sputtered Nb can be larger than the bulk value, and field leakage has been ignored.

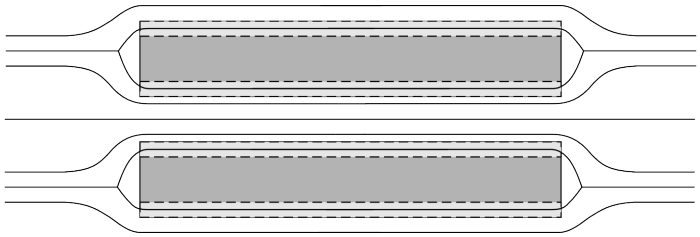

Figure 3.13: Schematic drawing illustrating the magnetic focusing effect. The light gray areas are λ_L thick, and the separation between the bottom of the top electrode and the top of the bottom electrode is d_{ox}. The field in the junction area is increased by the flux deflected away from the electrode banks and into the junction area

Finally, it is well-known, that the critical temperature of thin films of superconductors can vary from their bulk values[60]. Especially the wiring layer, which can be deposited by evaporation might have a lower critical temperature because of the deposition technique. The lowest critical temperature of the two electrodes can be measured by measuring the gap voltage as a function of the temperature found from a calibrated solid-state thermometer in thermal equilibrium with the sample. This data is fitted to the BCS theory predicted dependence of $\Delta(T)$, and the critical

temperature can be extracted. This measures the lowest of the two critical temperatures of the junction electrodes, as the junction no longer exhibits the Josephson effect above this value of the temperature. This was done, and the results are shown in Fig. 3.1 in Sec. 3.2.2. The fit yields a critical temperature for the junction of 9.12 ± 0.04 K, which fits well with predictions from [60] for the electrode thicknesses used in sample fabrication.

The electrical parameters of the Nb-Al/AlOx-Nb junctions used for the Josephson junction Kibble-Zurek measurements were identical. The critical current density was $J_c(0) \approx 60\text{A/cm}^2$ yielding a cold Josephson penetration depth of $\lambda_J(0) \approx 50\mu$m. The width of all junctions used for these measurements were 4μm with a total idle region width of 3μm. The layout for the type of sample used for all annular overlap Josephson junction Kibble-Zurek experiments is shown in Fig. 3.14(a). The sample geometry of the 1.5mm and 2.0mm Lyngby geometry samples are similar, only they are placed in parallel across the sample rather than in series along the length of the sample, as the annular overlap geometries. The sample layout in Fig. 3.14(b) is used for the single ring experiment with either SQUID or optomechanical readout.

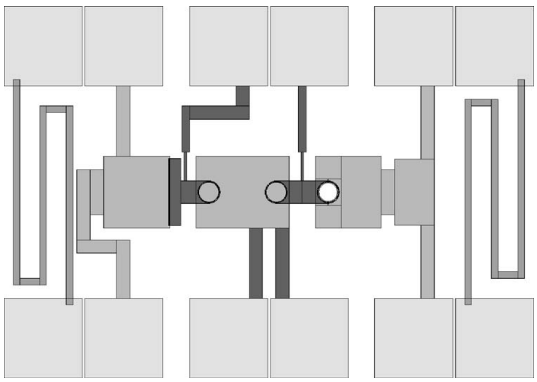

(a) Sample for Kibble-Zurek measurements on annular overlap junctions. From the left to the right, one long linear overlap, two JJ3 and one JJ4 type junctions are seen[33].

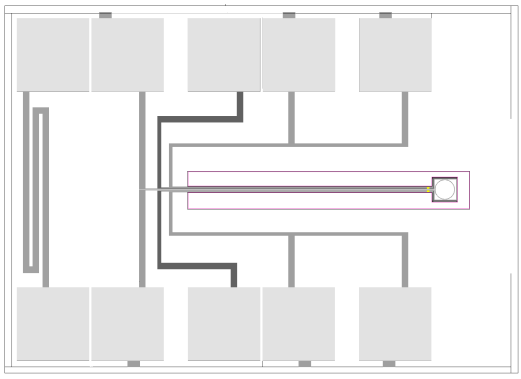

(b) Sample for Kibble-Zurek measurements on single ringe. The four cross junctions used as thermometers are placed on the island around the ring. This sample layout was used for the single ring SQUID measurements.

Figure 3.14: Examples of the sample layouts for the samples used in the project. The bottom electrode layer is a lighter shade of gray compared to the top wiring layer. On the far right and left, the two resistive meander heaters are shown, and on the top and bottom the two rows of gold contact pads are visible. The total sample size is 4.2mm × 3mm.

3.3.6 Annular junctions

Most of the Kibble-Zurek measurements in this project has been done with annular Josephson junctions of the annular overlap type. Typically, they have been of the Nb-Al/AlOx-Nb type, but Nb-Al/AlOx-NbN-Nb have been used as well. The motivation for this, and differences between the two will be described below. The all-Nb junctions are called symmetric, whereas the ones having both Nb and NbN electrodes are called asymmetric.

All junctions used are quasi-onedimensional meaning that for all experimental parameters, the width is much less than both the Josephson penetration length and the predicted frozen-in correlation length of the Kibble-Zurek phase transition.

Symmetric annular junctions

Most of the Kibble-Zurek measurements in this project have been done using annular Josephson junctions of the symmetric annular overlap type. The production method for these Nb-Al/AlOx-Nb junctions is so stable, that the voltage of zero-field steps associated with trapping of fluxons is very reproducible across different junctions, and even different production batches. In addition, when magnetic shielding and electrical noise is handled appropriately, the shape of the zero-field steps in the IV-curve of the junction is ideal in almost all cases (symmetric around $I = V = 0$, negligible critical current in zero applied field and almost vertical steps). This reproducible shape of the zero-field steps allows for easy automated analysis of obtained data for recognition of fluxon trapping, which is essential due to the large set of data required to test scaling behavior with low critical exponents and low trapping probabilities.

The stable production method also meant that flux trapping in the electrodes and wiring layers going to the junctions was almost non-existent because no pinning sites of appreciable potential depth was available. Even in the case of an Abrikosov vortex trapped because of the Kibble-Zurek mechanism, it will most likely disappear out of the film across the edge, or annihilate with a nearby antivortex. This is important, as the existence of Abrikosov vortices close to, or inside, the junction will change measurable junction parameters such as the critical current[55, 61]. To test if Abrikosov vortices were present, a large dataset of recorded IV-curves after quenches was examined. All the IV-curves with trapping was excluded, and the remaining were analyzed determining the critical current, and a histogram of the measured critical current was made. In case of pinning sites defined by weak spots in the electrodes or other defects, specific values of the critical current should have increased probability. Also, if the distribution had significant width compared to the maximum critical current, the simplest conclusion would be that the influence of the Abrikosov vortices was important. The result of this diagnostic analysis is presented in Fig. 3.15.

As seen, almost all the recorded critical currents lie within about 5% of the maximum for the junction measured. This distribution is similar in shape, but slightly wider than expected, when compared to the litterature[62, 63]. The increased width is not surprising, both because of the fact that the geometry of the junction is significantly different compared to the cited article, but mostly because of the data acquisition method. The data in Fig. 3.15 is obtained from recorded IV-curves in current bias mode using a sweep generator. The setup is not optimised for current noise in the sweep current, so this will widen the distribution. Also, the data recording rate compared to the sweep rate gives a measurement uncertainty on the order of

$$\delta I_c \approx \frac{\frac{dI}{dt}}{f_{DAQ}},$$

where dI/dt is the sweep rate, and f_{DAQ} is the frequency of the data acquisition (points per second). Using the typical numbers of a triangular sweep at 10Hz with an amplitude of 1.5mA, and a data acquisition frequency of 1000 points per second, gives an uncertainty of $\delta I_c \approx 0.06mA$,

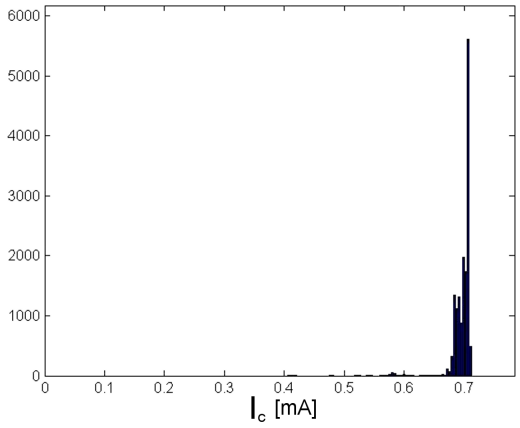

Figure 3.15: Stability testing of the critical current across approximately 18000 quenches. The histogram counts how many times the critical current fell in a range of 1/200th of the maximum measured critical current.

which is very close to the actual width of the distribution seen. Unfortunately, this will tend to mask any other causes, that would make small changes to I_c from quench to quench. However, the effect of Abrikosov vortices pinned in the junction electrodes can be significantly larger than 5% of the critical current, so repeated quenches should reveal this effect as long as the number is large enough.

To be able to distinguish between fluxoids generated because of the electrode superconducting phase transition, and fluxons generated by the Josephson phase transition, two slightly different flavors of the annular overlap junction was created. One of them has a hole through both superconducting electrodes, where the other has only one hole. If the production of fluxons in the Josephson junction is dominated by the electrode-generated fluxoids which is then measured by the junction, the probability of trapping a fluxon should be twice as large in the geometry with two holes compared to the one with a single hole, at least as far as the probability is low, and situations with trapping in both rings independently can be disregarded. The two geometries can be seen in Fig. 3.16.

Asymmetric junctions

The asymmetric annular junctions used in this project were identical in geometry to their symmetric counterparts. The only difference is the substitution of Nb in the counter-electrode (third layer in the tri-layer structure) with NbN, thus leaving an Nb-Al/AlOx-NbN-Nb structure.

The motivation for doing this experiment was twofold. First of all, it is predicted in [24] that asymmetric junctions should have a different scaling exponent than symmetric ones, and it was here proposed to develop significantly asymmetric junctions for this purpose. The scaling exponent for asymmetric junctions were predicted to be $\sigma = 1/7$, but that was based on the original theory for the Kibble-Zurek mechanism in annular Josephson junctions, that has now been proven wrong. In any case, a slower variation of the trapping probability versus quench time was

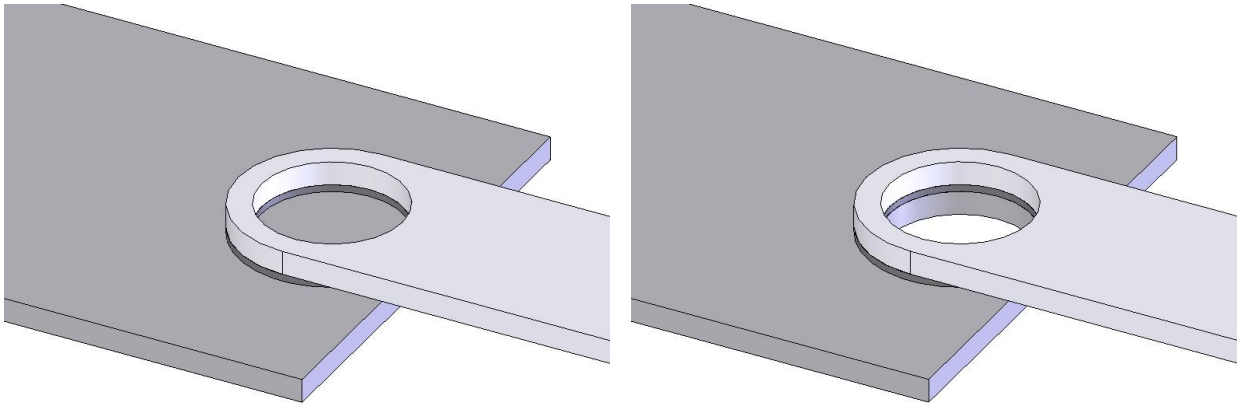

(a) The JJ3 annular overlap geometry with a single hole.

(b) The JJ4 annular overlap geometry with two holes.

Figure 3.16: The two different annular overlap geometries used for discriminating between electrode-driven and Josephson-driven fluxon production.

expected.

Secondly, there were some questions in principle to the understanding of the symmetric Josephson junctions. According to the newest available theoretical work [33, 34], the phenomenon of flux trapping is related to the Josephson phase transition, which is considered isolated from the superconducting phase transition of the two ring electrodes. Essentially, the fluctuations are thought as small Josephson junction domains. But as is described in Sec. 2.4.2, the rings themselves undergo a potentially symmetry breaking phase transition at the same time. The annular Josephson junction could be thought of as simply an experiment on two superconducting rings, in which the difference in number of trapped fluxoids can be read out by detecting the number of fluxons through the layer separating them. To make matters worse, the trapping probability estimates for the two systems are of the same order of magnitude, although they scale differently (rings with $\sigma = 1/4$ and Josephson junctions with $\sigma = 1/2$, see Sec. 2.4). In addition, there is the discussion on whether or not the two rings in such a case could be described as truly uncorrelated, both because of tunneling currents and because of almost perfect magnetic coupling through their mutual inductance. Therefore it is interesting to conduct experiments, that identifies one or the other phase transition, as the dominant one in producing fluxons. By using an asymmetric junction, in which one of the ring electrodes have a critical temperature, that is higher than the other, the system in principle provides a mean of looking at a phase transition in a single ring by heating the system to a temperature T, where $T_{c_1} > T > T_{c_2}$, thus keeping one ring static and the other subject to a phase transition. This sets very strict limits on the thermal cycling parameters, in order to reach a maximum temperature below T_{c_1} and above T_{c_2}, while still varying the quench time significantly. However, the experiment is still interesting, even if the maximum temperature is above T_{c_1} electrodes critical temperature, as this will be a great test of the magnetic coupling between two rings. The ring with the highest critical temperature will certainly become superconducting with no interference from other superconducting films as long as T_{c_1} is significantly different from T_{c_2}, and

the T_{c_2} electrode ring will therefore cool down in whatever field is left from the phase transition at $T = T_{c_1}$ (due to fluxon production or shielding of any magnetic field present).

For these reasons new samples were made, where one of the Nb electrode rings in the junction were replaced by NbN, which has a critical temperature of approximately 4K higher than Nb.

3.3.7 Ring with junctions

A completely different way of measuring Kibble-Zurek generated defects using Josephson junctions have also been designed, but not tested yet, due to fabrication delays. It is based on detecting the screening currents, that must be present in the surface of a superconducting single ring, if it has a fluxoid trapped inside. The method is strongly inspired by the results found investigating the effects of a transverse field on Josephson junctions of various geometries[41].

The idea is that the screening currents screening the bulk of the superconducting ring from the trapped fluxoid must themselves induce a magnetic field in the volume around the ring. By placing a Josephson junction in the area that this field must go through, any trapped fluxoid will result in a modulation of the critical current of the Josephson junction, similar to the effect of an externally applied transverse field. This also allows detection of the number of fluxoids trapped in the ring in a reproducible way, by application of a transverse field to the system, and detecting the field required to cancel the effect of the trapped fluxoid(s).

This system sounds remarkably like the annular junction detection method for detecting fluxons by measuring critical current of the junction as a function of externally applied external field, and the geometry of the junctions is also very similar, with a few key differences. The geometry is shown in Fig. 3.17. The obvious difference is the inclusion of two different junction counter electrodes on top of the base ring electrode. The second change is the removal of a small part of the full annular junction to leave an almost complete annular junction.

The purpose of having two different counter electrodes on the base ring, is that any screening current on the outside of the ring will preferentially affect the outermost counter electrode, and vice versa for the screening current on the inside of the ring. If the interaction of the field from the induced screening currents to the electrodes is large enough, their magnitude can be detected directly by their modulation of the critical current of the respective junctions. In effect, the outermost junction will act like a magnetometer by detecting the induced field, which is proportional to the screening current, in a very DC SQUID-like fashion, when below T_c. The innermost junction should be less effected by external fields, because it is better screened by the ring ground-plane. If the interaction between the induced screening currents and the junctions is not large enough to give a good signal-to-noise ratio directly, it should be possible to do a differential measurement between the two junctions as a function of applied magnetic field to make the equivalent of a SQUID gradiometer. As a magnetometer, the main advantage of this setup is the ability to find the zero of external field, as the maximum critical current is enveloped by a decreasing function of applied field. On the other hand, this effect also limits the dynamic range of the device to typically a few tens of the critical field of the junction.

The purpose of removing a small part of each of the electrodes is to avoid the Josephson phase transition created fluxons. In case they are produced, they will simply disappear out the ends of the junction. This leaves the experiment only sensitive to the fluxoids produced in the phase transition of the single ring. It is also entirely possible that any trapped fluxoids will be localized

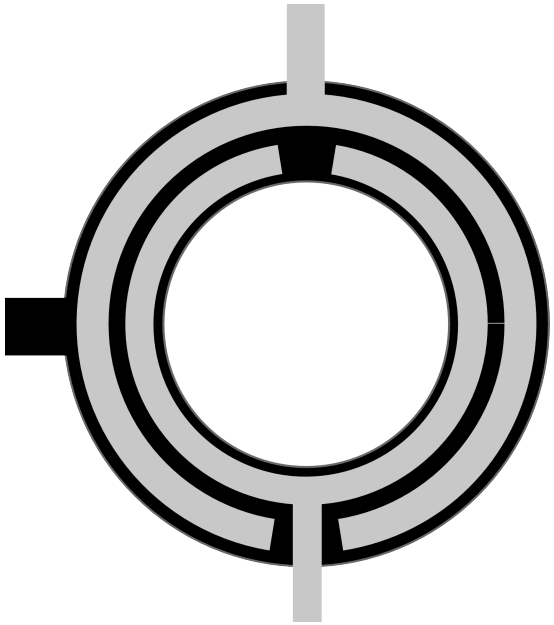

Figure 3.17: Single superconducting ring with partial annular junctions. The bottom electrode is black, and the top is gray.

to the area between the open ends of the junctions for energetic reasons. In this case, the result would most likely be an increase in the critical field of the junction in one direction of a transverse field, and a decrease in the other.

In conclusion, it is hard to predict to which extent this new method of detecting trapped fluxoids, by their near-field magnetic effect on a Josephson junction, will be successful, but experiments in the near future will surely yield interesting results on this matter.

3.3.8 Implemented Josephson junction setup

The measurements done in the annular Josephson junction setup is performed in batches, within which τ_Q is kept constant. Before each batch is started, τ_Q is measured by running the cycle with identical heating/cooling parameters, only with a fixed current bias and connected voltage probes.

The individual measurements in each batch are done according to the following protocol. Starting from a base temperature of approximately 4.2K, the mounted sample is heated using one of the heating systems to a temperature far above T_c. The heat is turned off, and all electrical connections to the sample are physically disconnected using relays built into the electronics box at the top of the cryoprobe. After the cooling is complete, the relays are switched on again, and a full IV characteristic of the annular junction is recorded using a triangle-wave current bias, with a frequency between 1Hz and 10Hz. After this, the process is repeated from the heating pulse for as many times as necessary to obtain approximately 100 successful trapping events.

Each measurement results in a dataset of (I(t),V(t),t) representing the sweep of IV characteris-

tic, which is then analyzed by an automated analysis script, see Sec. 3.5.1. If performing detection by the magnetic field dependence of the critical current, several datasets are recorded at the end of each cycle, with different applied fields, and the detection is done in a similar way, but using a different script.

The implemented Josephson junction setup, which has been used for both Kibble-Zurek measurements and some of the transverse magnetic field experiments is shown in a rendered CAD image in Fig. 3.18(a), and a photo of the finished sample holder with wiring in Fig. 3.18(b). On the photo, the wiring and solid-state Ge thermometer is visible. The Ge thermometer is mounted inside the Cu bulk using thermal grease and the wires to it are thermally anchored to a custom-made Cu screw fixed to the bulk. The end of the sample holder doubles as a coil holder, which fixes the coil centered around the sample with an angular alignment tolerance on the order of a few 1/10ths of a degree to the sample holder axis. When in use, the sample holder is hung sample-side down inside the magnetic shielding, submerged in LHe in a magnetically shielded commercial cryostat. The sample is parallel to the bottom of the can-shaped shields, as any field reaching this area (even though strongly damped), will be parallel to the sample, and thus less likely to influence the phase transition (see Sec. 2.5).

The nomenclature used in the low-temperature physics lab at DTU Physics is explained below.

- **Cryoprobe**: The entire probe with a cold end going into the LHe cryostat and a room temperature end with all of the preamplifiers and control circuits built in. It is approximately 1.5m long.
- **Sample holder**: The part of the cryoprobe mounted inside the magnetic shielding in the cold end of the cryoprobe. It is mostly copper, and encompasses everything drawn in Fig. 3.18(a).
- **Insert**: The PCB board with spring-loaded electrical connections (red in Fig. 3.18(a))
- **Sample**: The silicon chip with superconducting structures on. It is mounted in the sample holder below the insert.
- **Can**: A can is a hollow cylinder closed in one end.

Shielding

The magnetic shielding of the experiment was implemented in several stages. As a general measure, all experiments were conducted in a magnetically shielded cryostat. The cryostat has two separate high-permeability shields built-in. The cryoprobe has a an outer superconducting Pb shield wrapped around the vacuum can. Inside, a high-permeability can shield followed by either a high-T_c YBCO superconducting can shield or another Pb shield is installed, fitting closely around the field coil. According to Sec. 2.6 this reduces the maximum attainable field by a factor of approximately 10, but since very low magnetic fields are needed, this is not a problem. Additionally, this could be fixed by inserting a sheet of high-permeability metal between the coil and the inner superconducting shield.

The shield ordering is important as it both sets the order of cooling, and the order of magnetic shielding. The cryostat's dual high-permeability shields reduce the field seen by the outer Pb

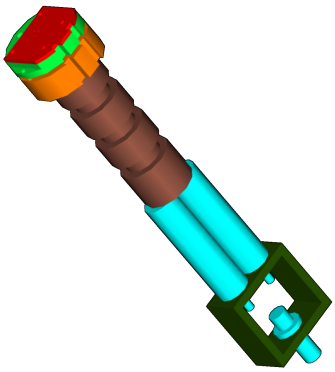

(a) CAD rendering of the cryogenic sample holder.

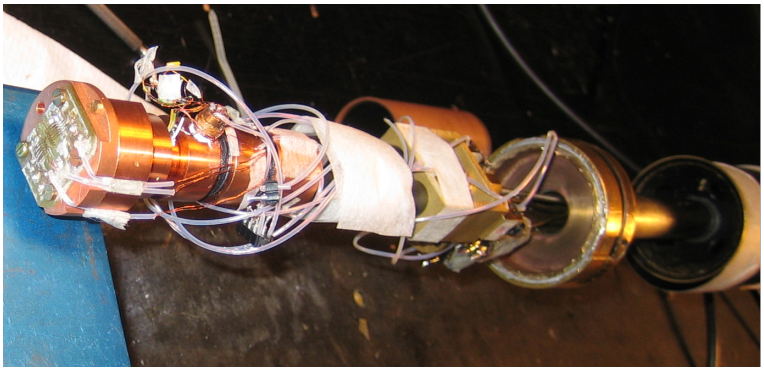

(b) Photograph of the cryogenic sample holder with wiring.

Figure 3.18: The CAD design and a photograph of the finished sample holder for the Josephson junction Kibble-Zurek experiments

shield during its superconducting phase transition. This will minimize the flux trapped here during the transition. Afterwards, the inner high-permeability shield reduces the field further before it reaches the inner superconducting shield. The inner superconducting shield thus cools in a very well-shielded environment, and by its cooling to the superconducting state locks the field configuration at the sample, so that any later changes in external field will be both shielded by the high-permeability shields and locked out because of the superconducting shields. The Pb shields were welded/molded from high-purity Pb sheets 1-2mm in thickness using our in-house workshop facilities.

As a matter of course, no magnetic materials are used inside the magnetic shields. All screws and connectors are checked before mounting with a compass as a crude test of magnetization. Only brass and copper metals are used in the sample holder end of the cryoprobe.

Electrical

To reduce the electrical noise in the system, experiments were performed in an electromagnetically shielded room, which is basically a Faraday cage with a volume of 60m^3. This works as a high-pass filter to electromagnetic radiation and has a cut-off frequency below 100Mhz, so any radiation in the frequencies involved in the experiments are removed. However, to conduct experiments, some electrically powered equipment must be used, including a desktop PC (see App. A.2) and several oscilloscopes are present inside the shielded room, thus contributing to the electrical noise of the system. To minimize these noise sources an additional Faraday cage is built around the experiment, including all of the first stage measurement electronics and the experiment itself - this of course requires a conductive and connected outside of the entire sample holder, including the cryogenic and removable parts. For all leads going into this Faraday cage, there are capacitive filters with a cut-off frequency of approximately 1MHz. Some these leads are additionally filtered with a cut-off of 10KHz for signals, that are not required to have high-modulation frequencies, such as the current input lead. All wires are twisted in pairs corresponding to the signal, the supply/measure in order to minimize the magnetic fields they generate or the induced currents they pick up.

An additional source of noise, that is even more important than measurement noise, is the back-noise of the instrumentation amplifiers connected directly to the junctions, which has a measurable effect on defect production. Actually, it was found, that this very low power noise would invariably result in trappings of Abrikosov vortices in the film of the junction electrodes leaving detection of zero-field steps inconclusive due to asymmetry in the DC IV-curve and erratic magnetic field dependence. In order to avoid this all active electronic components must be physically disconnected from the cryogenic parts of the cryoprobe and all leads left open, from the heat pulse and until the cooling is complete. The electronics compartment of the cryoprobe in the top box is divided into a clean and a noisy part, with a copper wall with filters between them. All active components, such as the amplifiers and relays for switching are placed on the noisy side and only passive components such as resistors are allowed on the other side. The relays are computer-controlled and the software created for the project allows for running identical cycles with or without disconnecting the leads. This is important, as the junction doubles as a thermometer for determining the quench time, which requires the connections to be intact during cool-down for this measurement. This is done once or twice during a batch of a few thousand cycles to make sure the quench time is not changed from start to finish.

The resulting setup has a voltage noise equivalent to approximately 1-2μV error on the junction voltage and, less importantly, around 2μA (where $I_c \approx 1$mA) error on the junction current. The junction current error from noise is less important, as it plays a very little role in fluxon detection, and is overshadowed by data acquisition timing errors.

Mechanical

The sample holder is shown in Fig. 3.18 and the heating system is detailed in Fig. 3.2. The most complicated part of the mechanical setup is the sample mounting itself. The two main problems is reproducible thermal connection between sample holder and sample and stable electrical connections. They are both related to the alignment of the sample to the sample holder.

The sample is placed on top of a pillar with the same cross-section as the chip with a thin layer of thermal grease between. A tight-fitting POM (polyoxymethylene) frame is placed around this pillar and sample, its height equal to the total height of the pillar and sample. As POM has a coefficient of thermal expansion, that is approximately $6\times10^{-5}K^{-1}$ compared to the copper sample holder's $1.6\times10^{-5}K^{-1}$ (both at room temperature), the frame will contract around the pillar during cooling, thus locking the sample in place.

The transverse direction is controlled using finger springs, pushing down on the top of the sample, and these double as electrical connections. The springs are mounted onto a PCB board, where the connection wires are soldered using non-superconducting solder. The PCB board is mounted on the copper sample holder using screws, thus fixing the sample-facing surface of the PCB board at the height defined by the frame height. The PCB board is drawn in red on Fig. 3.18(a).

When looking at the sample holder in Fig. 3.18(a) it seems to violate the design principle of only one mechanical connection, as described in Sec. 3.1.4. Specifically, there are two cylinders connecting the square frame to the cylindrical end part. There are two reasons for this; (1)they supply improved support for wires over a single cylinder and (2)they fix the rotation of the sample to the rotation of the frame. This allows for testing the magnetic shielding of the sample holder, by attaching a magnetic detector to the bottom of the sample holder and twisting or moving the sample holder up and down. The magnetic detector can be the junctions on the sample themselves or alternatively a DC SQUID magnetometer. In either case, the important parameter is the change in measurement output as the sample holder is moved inside the shield. This is the only way of testing the magnetic shielding directly, and also provides an indication of whether any magnetic components are present in the vicinity of the sample holder. By rotating the entire sample holder, the shielding of external magnetic fields, such as the Earth's magnetic field, can be tested.

Thermal

For thermometry, a combination of the available methods have been used. For very slow quenches, the solid-state Ge thermometer was used, and a fairly large overlap with the measurements using the Josephson thermometer was tested. This was done as a calibration of the Josephson thermometer to show that the measured quench times using the two methods were within measurement tolerances. It was seen, that for all quenches with $\tau_Q \geq 1$s the two measurements coincided within the estimated measurement uncertainty of 10%. For lower quench rates the two does not coincide, as expected, because the Ge thermometer readout is no longer a good indication of the temperature at the sample, which is the one measured by the Josephson thermometer.

For heating, the integrated resistors on the sample were used. The main reason for this, was the ease of use because no optical fibers needed to be drawn into the cryoprobe and vacuum-sealed. The ringing through the coupling to the coil was observed, and the decay time determined. This sets the time interval, the sample needs to stay above the critical temperature after the heating pulse has ended. It was found to be reasonably easy to create heating-cooling cycle parameters that fulfill this.

The thermal system can produce and characterize quenches with a quench time from below 1ms to above 50s. Below 1ms the temperature gradients across the sample will begin to have an effect on defect production (see Sec. 3.2.4), so thermal gradients need to be addressed before the

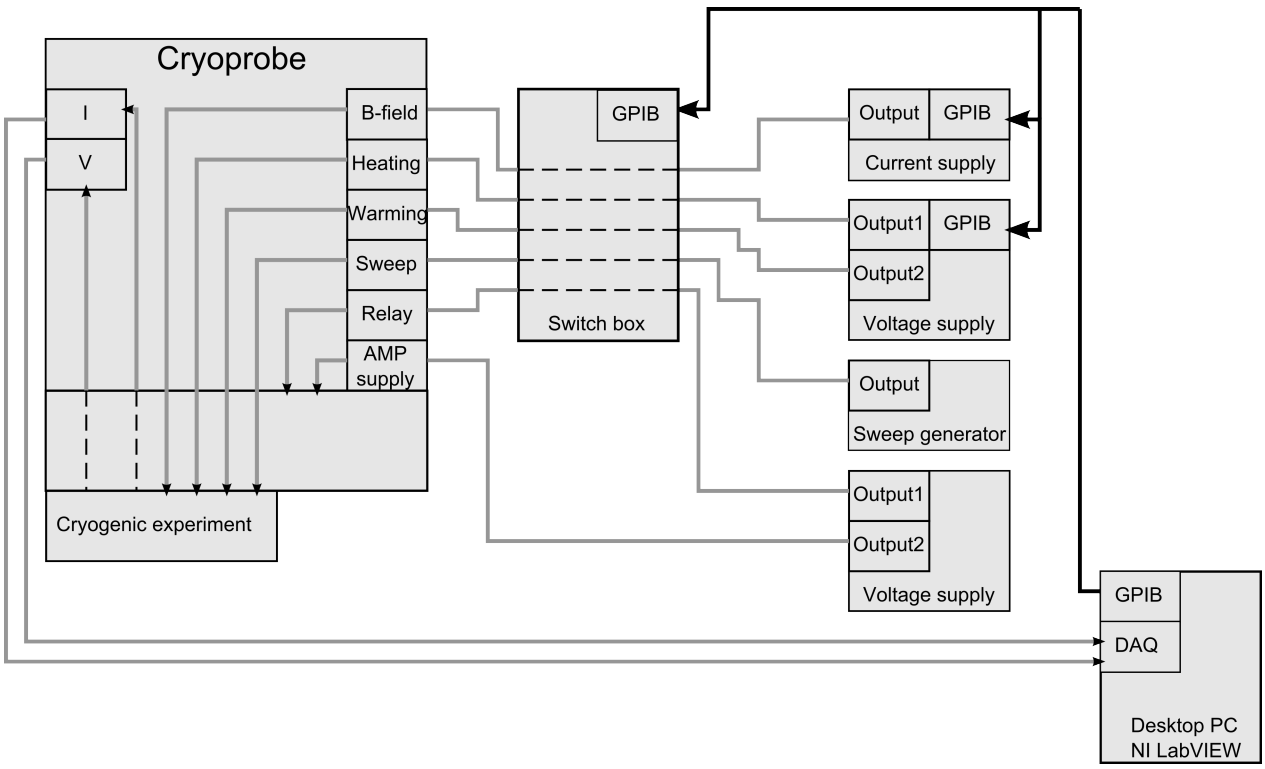

Figure 3.19: The equipment connections used for running annular Josephson junction Kibble-Zurek measurements. The black wires indicate GPIB cables with digital signals, the gray indicate cables carrying analog signals, and the dashed lines are the ones controlled by relays, either in the electronics box of the cryoprobe or the switching unit. External preamplifiers and oscilloscopes not shown, likewise for ground connections.

heating system becomes the limiting factor.

Data acquisition and system control

The final part of the implemented setup is the software, and the interfaces to all the equipment attached for control of the experimental parameters as well as data acquisition and analysis. An overview of the software is given in Sec. 3.5, and the equipment used is listed in App. A.2. All of this is connected through a common GPIB bus to the GPIB card of the lab computer for control (LabVIEW system), and a data acquisition card for data recording and storage. The connected setup is schematically shown in Fig. 3.19.

In addition, a modular amplifier box containing relays, switches, filters, a built-in dummy and a number of preamplifiers was designed, and 4 copies produced. They are each capable of controlling and monitoring one 4-point measurement system, and was used both for annular Josephson junction experiments and the single ring SQUID experiment. The electronic layout of the box interior can be seen in App. G. It fits directly to the standard 25-pin connector found on some of the cryoprobes used in the group at DTU Physics. In particular, one of the cryoprobes has

access for 4 of these boxes at the same time, allowing for thermal gradient measurements while doing Kibble-Zurek measurements on a single ring setup whether it is SQUID or microcantilever based.

Measurement procedure

To run a batch, consisting of a large number (>1000) of heating/cooling cycles, a standard procedure was followed. Starting from a cold (4.2K) system in thermal equilibrium, the wanted heating parameters are selected in the VI. These are the heating pulse height and width as well as cooling time and data acquisition time. In addition, to stabilize any zero-field steps, a warming voltage can be specified, which is supplied across a resistive wire wound around the sample holder neck.

In order to measure τ_Q the VI is run in calibrate mode, which means that all relays are closed during the entire cycle. The sweep generator is replaced by a fixed current source as well, feeding current at a value of about 25% of the total gap current jump. It is now possible to record the voltage response of the junction as a function of time, as described in Sec. 3.2.2. In order to obtain the cooling rate of the actual experiments, the heating/cooling cycle is allowed to run for some time until the temperature at the end of a cycle is constant. This typically takes 10-20 cycles. After this, the $V_g(t)$ data is recorded and τ_Q determined.

After τ_Q has been determined, the VI is switched into measurement mode, which turns on control of the relays. These will be disconnected during the cooling part of the cycle to avoid any interference with the phase transition. In addition, the sweep generator is attached for providing the bias current sweep for recording the IV characteristics. A GPIB controlled coil current supply is also attached, which will be connected to the field coil around the sample during cooling, but disconnected during data acquisition to avoid influencing the IV characteristic.

In measurement mode, for a given τ_Q, the trapping probability of one fluxon, $\bar{f}_1$, is measured as a function of transverse magnetic field. The range of applied magnetic field is approximately $\pm 0.50 \mu T$ corresponding to a few flux quanta through the annulus area in either direction. This data is used for comparison to the theory of Sec. 2.2.5, as well as determination of any residual field that might be present. The system should be fully symmetrical in applied field, so any shift in the point of symmetry is an indication of residual fields from the shields or otherwise. If this was detected, the entire shielding setup should be heated and cooled slowly again. However, this was very rarely the case, and for most cases any asymmetry found was less than 10nT, and thus far below one flux quantum in the ring area. The limit of one flux quantum per ring area is used as an order of magnitude estimation of the field strength that will be unacceptable for 'zero'-field Kibble-Zurek experiments. According to the theory in Sec. 2.2.5 and [18], it should still be possible to do Kibble-Zurek experiments with non-zero fields, but this assumes that the model set forth there is correct, which still has to be experimentally verified. In any case, much of the work done on Kibble-Zurek measurements in annular Josephson junctions were carried out prior to the development of this theory. If necessary, an additional sequence of cycles is run at the symmetry point (in applied magnetic field) to obtain better statistics.

If the batch takes a long time to complete, the calibration procedure is repeated at the end to make sure, that τ_Q has not changed more than the desired tolerance of 10% over the batch measurement time. Typically, measurements can be done over 6-14 hours without appreciable change in τ_Q, depending on the level of liquid helium in the cryostat.

3.4 Superconducting rings

The second main focus of this project was the design and development of an alternative system for Kibble-Zurek measurements. The simplest, most obvious alternative to the annular Josephson junction system is the single ring system. One example of this has already been described in Sec. 3.3.7, although experimentally it is more closely related to the Josephson junction experiment than to the experiment of quenching a single isolated ring.

Several experimental alternatives for detecting any defects produced in the quench of a superconducting ring have been evaluated during this project. The topological defects of a single, isolated superconducting ring are called fluxoids. They are the quantized magnetic field in the ring, trapped by the Meissner effect. As such, the simplest way of detecting the presence of a fluxoid is through its magnetic interaction with some detector. Like the annular Josephson junction, the superconducting ring has the great advantage, when compared to the liquid helium experiments, that the final defects produced are constant over time. Thus, the detection can happen at a much later stage, without the need for modeling decay/annihilation of defects. These experiments are therefore neither limited by either a model for defect decay, which is very hard to test experimentally, nor by a small time-window in which to perform measurements.

It has been argued, that the Josephson setup provides a test of, whether the production of defects is solely determined by the dynamics of the system after the transition[64] or also of dynamics before. The reason is that the Josephson phase transition is only meaningful for $T < T_c$, and has a theoretical critical scaling exponent, $\sigma_{JTJ} = 1/2$, where the superconducting ring phase transition can be understood as a result of the dynamics either before or after the phase transition, and has a theoretical of $\sigma_{SC} = 1/4$. The system is unique in the sense, that it is predicted to have a discontinuity in the critical exponents before and after the phase transition, and is thus not symmetrical. Testing the two approaches to Kibble-Zurek measurements should shed some light on the theoretical discussion, which is unique as they are so similar, yet theory predicts different critical scaling.

It was also important to take away some of the ambiguity of the Josephson experiment. In some ways, some of the elegant features of the Josephson junction experiment also makes it somewhat unclean. The thermometer-function of the junction requires superconducting leads to the ring electrodes, which is hard to model theoretically, and may have an influence on the phase transition dynamics. Even disregarding the question of a non-trivial geometry of the superconductor undergoing the phase transition, there is still the question of electric noise coupling from the wires, even if physically disconnected at their room temperature terminals. Finally, the electrical heating and its coupling to the field coil is a potential problem and should be relieved when building a new setup, particularly if optical fibers are already a part of the setup.

3.4.1 Micromechanical detector

There is a long tradition for using micromechanical systems for detecting very small forces[65, 66], and applications to magnetic domain imaging were one of the first successes of the atomic force microscope[67]. The force resolution of the first generation atomic force microscopes was on the order of 0.1 nN, but has since improved significantly, depending on the detection scheme and operating mode.

Therefore it was reasonable to try to adapt the known and well-tested technology of atomic force microscopes to the problem of detecting the tiny magnetic dipole moment of a superconducting ring with a single fluxoid trapped. The magnetic dipole moment of a single trapped fluxoid is (see App. D.2)

$$\bar{\mu} \approx 1.0 \times 10^{-13} \hat{e}_{\perp} Am^2 \,,$$

where $\hat{e}_{\perp}$ is a normal vector orthogonal to the ring. The challenge to the micromechanical detector setup was to be able to resolve this dipole moment in a reproducible, absolute way. This included determining the absolute number and the sign of the trapped fluxoids.

Thermal control and thermometry

One of the elegant features of the Josephson junction setup was that the temperature of the system undergoing the phase transition could be monitored directly. This is not available in the single ring experiment, as the ring is completely electrically isolated. However, the success of the Josephson thermometer in the annular Josephson setup is undeniable, owing partly to its response time and partly to its small size. It would be a big improvement, if some hard data about the thermal gradients was available as well.

Building again on the success of the annular Josephson setup, the on-sample resistive heating should be included, even if alternatives are available. There are several issues with resistive heating as described in Sec. 3.2, but the range and versatility of this approach easily outweigh any added complication to the setup. A new setup with both laser heating and resistive heating would also be able to determine the magnitude of any errors introduced by the resistive heating, by comparing the results obtained when using the different heating mechanisms. Finally, as laser heating has not been tested in our setup, the addition of an on-chip resistor is an essential backup.

Mechanical setup

When a fluxoid is trapped in the superconducting ring, either from quench-induced Kibble-Zurek trapping or magnetic field induced trapping of the applied field, this dipole moment is frozen in when the phase transition is complete. The only way to release it is by heating the sample above the transition temperature. By applying a magnetic field parallel to the cantilever, the dipole moment fixed to the ring will experience a torque, τ_{dp}, which is then transfered to the cantilever, the ring is attached to. This is shown in Fig. 3.20.

$$\tau_{dp} = \bar{\mu} \cdot \bar{B}_e \,, \tag{3.14}$$

where B_e is the applied field parallel to the cantilever.

A simply made coil can produce a field strength of, say, 3mT on the sample position, which gives a torque of

$$\tau_{dp} \approx 3.1 \times 10^{-16} Nm \,.$$

3mT is significantly below the critical field for the superconducting materials used. The deflection of the free end of a cantilever under an end-moment load is

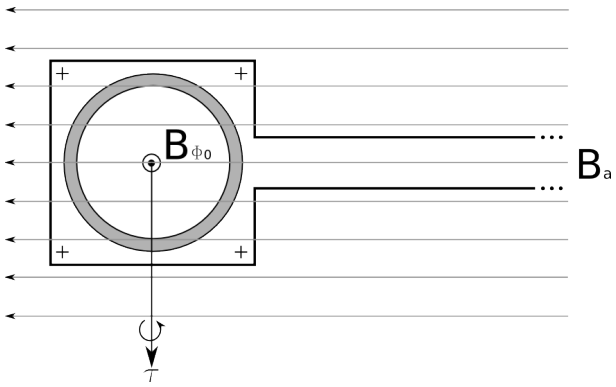

Figure 3.20: The basic principle behind the micromechanical magnetic dipole moment detector. The plus-signs indicate the position of the Josephson cross junction thermometers

$$\Delta z = \frac{\tau l^2}{2EI}\,, \tag{3.15}$$

where l is the length of the cantilever, E is the elastic modulus for the cantilever material, and I is the area moment of inertia of the cross section of the cantilever, which for a rectangular cross section is

$$I = \frac{wt^3}{12}\,, \tag{3.16}$$

where w and t is the width and thickness of the cantilever, respectively [68]. To complete the design, of the micromechanical system, it is necessary to set the detection threshold on Δz. As this has to be done in cryogenic conditions, which complicates things significantly in terms of detection, the design specification detection threshold is set at 1nm, which is at least an order of magnitude higher, than for room temperature systems. Furthermore, for production reasons, the thickness cannot be less than 1μm and the width no less than approximately 50μm. The first is because of the thickness tolerance of a single layer of silicon and the second is because of the required number of electrode leads on the wire to the Josephson thermometers - see Sec. 3.4.1.

From this design specification, assuming a silicon cantilever, it is possible to determine the minimum length of the cantilever, l

$$l > \sqrt{2EI\frac{\Delta z}{\tau_{dp}}} \approx 1.75\text{mm}\,. \tag{3.17}$$

This is about the limit of production technology for floppy cantilevers, the main limitation being fragility of the released cantilever causing failure when exposed to turbulence or viscous drag while etching.

An alternative detection strategy for the cantilever-based measurements would be to actuate the cantilever at its resonant frequency. This could be done by simply applying an AC current to the field coil at a frequency close to the cantilever resonance. If any dipole moment exists, it will

be repeatedly actuated, and the maximum deflection in this case determined by the equilibrium in which dissipation in the vibrating system equals the power input from the magnetic field actuation. It can be characterized by the Q-factor of the resonator, which is defined as the number of oscillation periods it takes for the amplitude to be reduced by a factor of e, when no longer actuated. The higher the Q, the lower the friction with associated higher equilibrium deflection amplitude. More precisely, it is

$$Q = T_m \frac{\pi f_n}{log(x_0/x_m)} ,$$

where T_m is the time it takes for the amplitude, x to decay to the value x_m[69]. Unfortunately, the Q-factor is notoriously hard to predict theoretically, as it depends on knowing the dissipative mechanisms in the cantilever itself, as well as any fluid or gas around it. However, in vacuum, systems similar to this have been found to have Q-factors well in excess of 1×10^3, sometimes as high as 1×10^5. In any case, the resulting amplitude will be significantly increased, but the ability to discriminate between positive and negative fluxoids would be reduced. It is conceivable that it would still be possible to discriminate by looking at the phase difference between the driving signal and the the sensor signal, but to what extent is hard to predict. The option to operate a cantilever, designed for single-fluxoid detection in static deflection mode, in actuated mode is always available, and would increase the signal-to-noise ratio in all cases.

Optical lever detection

The first implementation of the atomic force microscope[65] measured probe deflection by using as position sensitive diode, also known as a split photodiode combined with the optical lever method. The method is well-tested and routinely delivers the required deflection sensitivity required by the design specifications given in the preceding section.

The optical lever method consists of reflecting a laser beam off the cantilever and measuring the deflection of the reflected spot on some surface further away. Simple calculations show[70], that the reflected beam from a bent cantilever will have an angular difference of twice the bending angle at the laser spot to that of a straight cantilever. In addition, because detection can, theoretically, happen arbitrarily far down the beam path, the angle difference can be magnified to arbitrarily large deflections of the spot on the detector. Depending on the space and optics available, the practically attainable total magnification can be up to a factor of 1000[66].

The great success of the split diode detector is a result of several features, but the most important is that the individual parts of the detector are electrically identical, which means that a differential measurement can be made directly. The simplest application of a split photodiode is to amplify the difference in photocurrents of the individual parts. By doing this, the signal goes to zero when the light is centered on the diode.

Unfortunately, cryogenic split photodiodes are not available, so a modification to the standard method is required. The goal of the modification is to have the same differential measurement, while not requiring a cryogenic split photodiode. The simplest solution is to somehow make a position dependent beam splitter, that would split the reflected laser spot between two different paths, which could then be detected separately. This would be done by transferring them to several identical room temperature photodiodes, which are readily available. These could then be

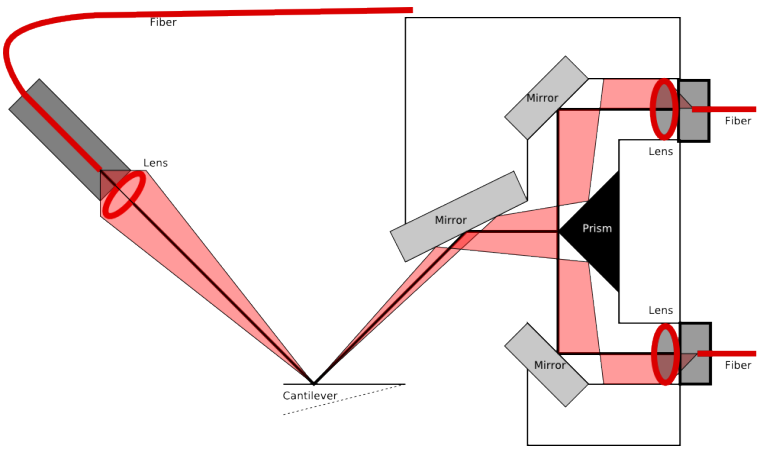

Figure 3.21: An implementation of a cryogenic-electronics free optical lever detector for cantilever deflection.

amplified differentially to provide the required sensitivity. A schematic showing this setup can be seen in Fig. 3.21.

Interferometric detection

Another obvious and well-tested method of detecting small position changes is interferometry. By measuring the phase difference between laser radiation reflected from the cantilever and that reflected from a reference mirror, any cantilever deflection in the direction parallel to the beam path can be monitored.

Applying this approach to a cryogenic setup without optical windows is most easily implemented by building an all-fiber interferometer. This can be done with relatively few optical components: one laser source, one directional fiber-coupler, working as a beam splitter and one photodetector. A simple schematic of this method is show in Fig. 3.22. The two arms of the interferometer consist of the path reflecting from the fiber cleaved end at the cantilever, and the path reflecting off the cantilever itself. Depending on the reflectivity of the cleaved end of the cantilever, it can even be used as a small low-grade optical cavity by which the resolution is enhanced by the multiple reflections between the cantilever and the fiber end. One of the main advantages of this setup is its mechanical stability, as the only free-space part of the beam path is the distance between the fiber end and the cantilever. The stability of the readout can be further improved by using the last output of the directional fiber coupler to monitor temporal variations in the laser intensity and subtracting this from the detector readout.

The sensitivity of this approach has been shown to be better than 0.03Å in static deflection mode (modulation frequency far below the eigenfrequency of the cantilever), and better than 1×10^{-3}Å$/\sqrt{\text{Hz}}$ for higher frequencies[71], although somewhat worse for cryogenic operation. In any case, this is significantly better sensitivity than necessary for detecting the deflection resulting from the magnetic dipole interacting with the magnetic field. In [71], the distance from the cleaved end of the fiber to the cantilever is on the order of a few μm because the light exiting the fiber is not collimated. By adding a small collimation lens at the end of the fiber, this distance

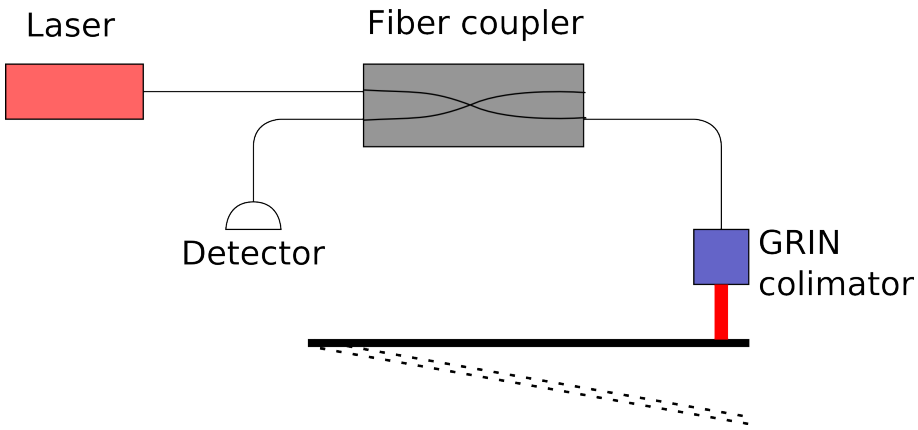

Figure 3.22: An implementation of a cryogenic-electronics free optical lever detector for cantilever deflection.

can be significantly increased without much loss of sensitivity. The limiting factors of sensitivity is laser frequency noise and laser amplitude noise, the latter created by laser radiation reflected back into the laser by the interferometer.

Production

There are many standard ways of creating microcantilevers in silicon. However, the fragility of the designed cantilevers severely limited the options. The simplest way of creating free-standing cantilever structures involves etching entirely through the wafer from the back using a standard wet anisotropic KOH silicon etch, to an already defined structure on the front. This process takes several hours, and therefore the front side of the wafer must be protected by a mask more resistant to etching than simple photoresist. The best choice for this is a hard mask of silicon nitride (SiN), which has to be deposited by chemical vapor deposition (CVD) at approximately 600K to avoid pin-holes. Unfortunately, the Josephson junctions can only handle 475K before breaking down, according to specifications, so this technique was unavailable.

An alternative method, which was eventually the one chosen, is based on a special type of silicon wafer called Silicon-On-Insulator (SOI). This type of silicon wafer is a sandwich structure with a base layer (handle) of single-crystalline silicon, a buried oxide (BOX) layer of silicon dioxide and finally a thin (device) layer of single-crystalline silicon on top. The type used for this process has a handle thickness of 350μm, a BOX thickness of 2.4μm and finally a device layer thickness of 1μm, as this is the desired thickness of the cantilever.

The process is very simple, and requires only a single mask for etching and one more for dicing:

1. HF clean the wafer with superconducting structures on the surface, 10 sec.
2. Spin-coat 1.5μm resist (AZ).
3. Perform photolithography process for negative resist using mask HOLE (defines the trench around the cantilever).

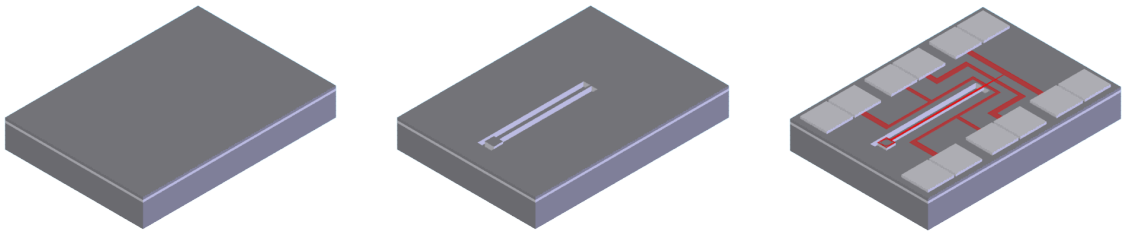

(a) The starting point, an SOI wafer. Crystalline silicon is dark gray and silicon dioxide is light gray.

(b) The sample after a reactive ion etch, that defines the cantilever in the top silicon layer.

(c) The sample after a gas-phase HF etch, that removes the exposed silicon oxide underneath the cantilever. The superconducting circuit is shown in red.

Figure 3.23: A graphical representation of the SOI-based process for creating the microcantilevers used in this project. For clarity, the progress of a single sample has been shown, rather than the whole wafer, and the electronic structure is shown only in (c), although present from the start. The photoresist is not shown at all.

4. RIE silicon etch (OH_POLYA:SF_6 + O_2, 30W, 5min)
5. Gas-phase HF etch (place wafer upside-down on PTFE support above 40% HF bath in fume-hood for 9 hrs)[72]
6. After degassing, plasma ash resist
7. Inspect using SEM
8. Spin-coat 1.5μm resist (AZ).
9. Perform photolithography process for negative resist using mask ALO (defines sample edges for dicing).
10. ICP ASE etch through 325μm Si (RIE dicing)
11. Plasma ash resist
12. Manually separate individual samples by cracking the remaining 25μm.

The process is described graphically in Fig. 3.23. The great advantage of this process is that the cantilevers are never exposed to liquids, which would otherwise make them fuse to the substrate beneath them during drying, and also has a rather high probability of breaking them directly by turbulence. The disadvantage is that the cantilevers only have room to swing approximately 2.4μ down, and gravity itself is enough to drag them that far. As a consequence, the cantilever samples must be stored upside-down, and can only be used for measurements in the vertical position. This is not a big problem, as the sample holder can be designed to conform to this limitation.

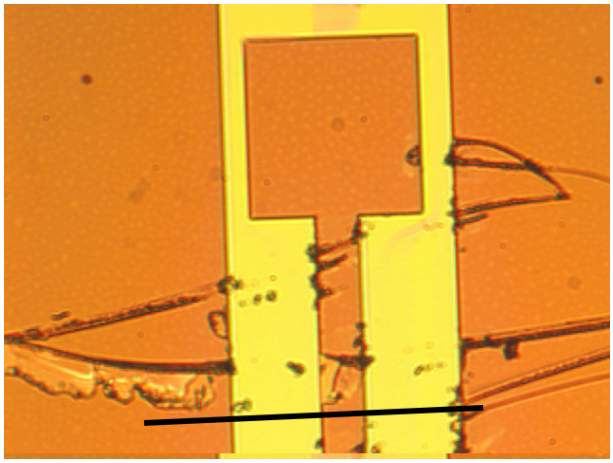

(a) Microphotograph of the cantilever after RIE etching, before gas-phase HF etch. The scratches are a crude destructive test with the purpose to check that the photoresist is present on the cantilever, and removed on the floor of the trench.

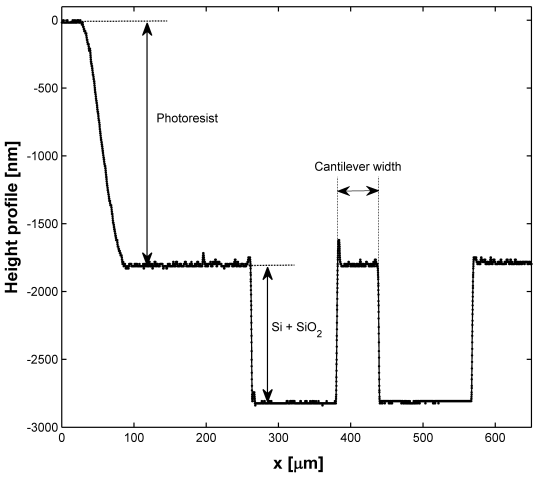

(b) Profilometer scan of across the cantilever and trench. Done on a sample after HF vapor etch, in which some of the photoresist was delaminated around the trench. The scan correspondes to the line in (a), although on a different sample where photoresist was damaged during HF vapor etch.

Figure 3.24: Initial characterization data for test batch samples. The microscope image is from a sample not yet HF vapor etched, and the profilometer scan is after HF vapor etching. It is seen that the oxide thickness is much less than 2μm on the test wafers.

The sample production is not finished, but several test batches has been produced from bare SOI wafers with good results. It has been shown, that the process works, but some technical difficulties were encountered, and these delayed final processing to the extent, that no finished samples were available by the deadline of this dissertation. Initial characterization of the test batch has been done, however. For the test batches a different, cheaper type of wafer was used. These wafers are made in the clean-room by oxidation followed by poly-silicon sputtering. For this process, an buried oxide thickness of 2μm is not easily attainable, and not essential for testing. The initial characterization of the test samples produced can be seen in Fig. 3.24 and the total sample layout when finished can be seen in Fig. 3.14(b) on page 49.

3.4.2 SQUID detector

Another way of detecting fluxoids in superconducting rings, is to use a DC SQUID magnetometer. There are several examples of this in published literature with varying degrees of success. They have typically dealt with either fluxoids pinned in a plane of high-T_c YBCO superconductor[9], or scanning SQUID microscope investigation of rings in a larger array[10]. The limitations of these approaches have largely been in the range of the attainable cooling rates, thermal gradients and, in the case of the YBCO experiment, a very slow scaling with quench time because of the added dimensionality of the system. In the case of the array of superconducting rings, there is some

questions as to the interaction of flux between different rings during the quench.

A theoretically simpler experiment would be to simply place a DC SQUID close to a single superconducting ring undergoing the phase transition. The challenges of this experiment is to put the SQUID close enough to the ring to obtain single-fluxoid resolution while still far enough away to avoid heating the SQUID above its critical temperature. The inductive coupling between the SQUID and the ring could also be an issue if placed too close. The first problem is solved most easily by using a high-T_c SQUID close to a sample with a low-T_c ring on it. Using a high-T_c SQUID at 4.2K will reduce sensitivity significantly, as the modulation depth goes down with increasing critical current densities in the junctions of the SQUID.

This setup has been realized as part of a master's thesis project in the low-temperature physics group at DTU Physics[46], and the data provides a proof-of-principle that the idea works. The noise level of the system is on the order of 20% of the signal change from an added fluxoid in the ring, and the heating cycles have been performed. The signal change due to a single fluxoid trapped has been checked, both by inducing trapping in the ring during cooling by applying a magnetic field, and by spontaneous Kibble-Zurek induced trapping of fluxoids. The results coincide with expected values from calculated flux-density and SQUID calibration using a weak coil. The realized experimental setup is shown in Fig. 3.25.

Resistive heating is used in the currently realized setup, which couples inductively to the SQUID, creating noise in the readout around the transition. This is a result of the large current in the heater and limited bandwidth of the SQUID circuit, and not an indication of an actual magnetic field during cooling. The inductance of the field coil used in this experiment is so low, that the corresponding time constant for field relaxation is low enough that it is undetectable. The field noise from the heating system should be completely eliminated by using laser heating rather than electrical. Without this field noise, it should be possible to check if the slow signal described by Polturak[9] is also present in single superconducting rings. This signal is a bit of a mystery, as it is seen at times around $10^3\tau_Q$ after the transition. The authors speculated, that the cause was thermoelectrical effects in the superconductor.

3.4.3 Designed single ring setup

The design specifications and measurement principles discussed in the previous sections resulted in a combined setup for measuring Kibble-Zurek trapping in single rings. While the design phase is complete, and most of the parts have already been manufactured or obtained, the assembly and calibration of the system has not been completed due to time constraints. The following sections will describe the final design and, to the extent that data is available, the calibrations and tests done on the individual parts of the setup.

The actual measurements will be performed similarly to those in the annular Josephson junction setup. First the thermal gradients and τ_Q will be measured by monitoring and storing, simultaneously, the gap voltage as a function of time and fitting them to exponential decay functions. The four channels should yield the same temperature and cooling rates at the transition temperature, and any deviation from this will be an indication of the thermal gradients present across the superconducting ring during the phase transition.

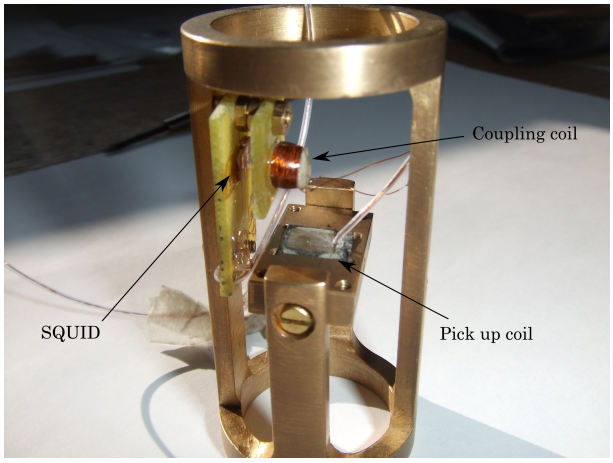

Figure 3.25: Photo of the experimental setup used for the single-ring SQUID-detector setup. The sample with the ring is mounted on the other side of the central brass block, directly beneath the pickup coil. The separation is on the order of 0.5mm[46].

Thermal

The resistive heating of the Josephson setup has been proven simple to use, easy to implement and reliable in creating reproducible quenches. For this reason a single resistive meander line has been included on the new samples. This will serve as a secondary heat source as well as a comparison to the primary heat source, which is a variable power green diode laser. The maximum power is approximately 100mW, which should be more than enough to heat the cantilever and nearest surrounding volume in a very short time. For comparison the resistive heater has a maximum heat load of approximately 8W, although this is never necessary. The laser heating is less powerful as it is only required to heat the cantilever rather than the entire sample, but it is still expected, that the attainable range of cooling rates will be reduced. If the experimental results warrant it, a more powerful laser could be retrofitted to the setup.

Preliminary results on the optical absorption on test cantilevers produced with identical parameters as the samples, showed that the cantilever and 2μm gap below it work as a very good absorber. It is believed that the reason for this is multiple reflections in the 2μm cavity below the cantilever.

When designing the samples for the new setup, priority was given to being able to directly measure thermal gradients, rather than having to rely on numerical simulations. For this reason, 4 small Josephson thermometers have been placed in a square around the ring on the cantilever island, as shown in Fig. 3.26(a). They consist of $3 \times 3\mu$m cross Josephson junctions with a maximum critical current of approximately 200μA. They will be used in the same way as the annular Josephson junction was used as a thermometer. This has already been tested, and data obtained have been shown in Sec. 3.2.2.

As these Josephson junctions are small cross junctions rather than intermediate length annular junctions, the maximum critical current is as high as about 70% of the current jump at the gap voltage. This makes it slightly more complicated to use as a thermometer, as we are interested in

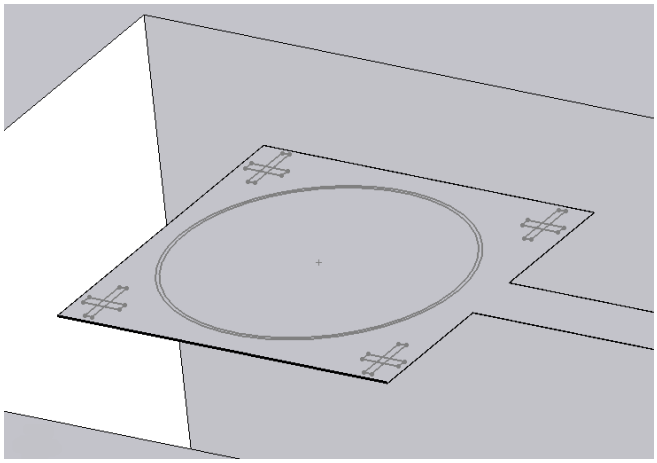

(a) Schematic drawing of the end of the cantilever with 4 thermometry cross Josephson junctions around the ring.

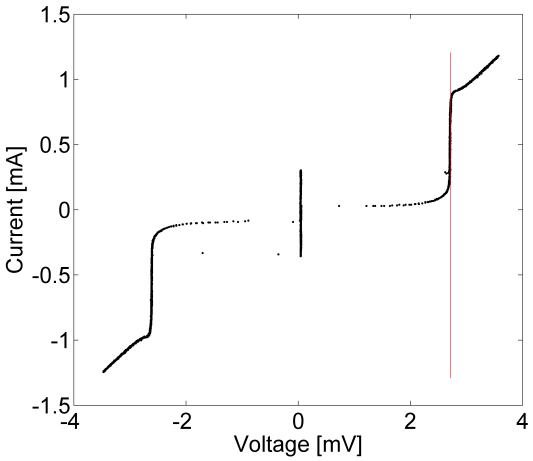

(b) The measured IV characteristic of one of the thermometry cross Josephson junctions. Reproduced from [46] with permission.

Figure 3.26: Thermometry solution in the single ring cantilever samples. This design is also used in the single ring SQUID experiment described in Sec. 3.4.2 and [46]

current biasing the junction at approximately 25% of the current jump at the gap voltage. When there are two possible voltages at this current, the system must be prepared in the gap position, which might not work because the gap disappears above T_c. As a security measure, the setup incorporates a magnetic field coil, which is able to generate the required field strength of 3mT at the junction site. This is the predicted first critical field of the junction. However, the tests show, that this is not necessary as the bias point seems to always stay on the gap curve, rather than the critical current curve. The simplest explanation for this is probably, that the critical current goes to zero at T_c as well as the gap voltage, and does not reach 25% of the current jump until the gap voltage has increased enough to prohibit jumping back to the critical current curve. As an illustration, the IV characteristic of one of the thermometry junctions are shown in Fig. 3.26(b)

Optics

The final design for the sample holder allows the use of both the optical lever and the interferometry detection methods. The interferometer setup has been built, and tested without connecting it to the new sample holder. The test was performed simply as a demonstration of the all-fiber interferometer. For the test, the sample was simulated by a mirror mounted on a piezoelectric stack. However, the resulting data was very noisy and suffered from very bad coupling from a free-space HeNe laser beam to the single-mode fiber reducing the reflected light intensity to 10^{-5} of the initial intensity. Of course, the loss of 75% of the light is unavoidable as the light must pass through the 50/50 directional fiber coupler twice.

The data shows sinusoidal interference modulation as a function of applied voltage to the piezo-controlled mirror, with a periodicity corresponding to half the wavelength of the laser radiation (λ = 632nm) as expected. The modulation depth is only a few times the noise amplitude,

even after filtering. The electrical noise could be improved by proper shielding of the detector, but the main reason for this very poor signal to noise ratio is the low optical power. This should be fairly easily fixed by either using a commercially available pig-tailed diode laser or a proper free-space fiber coupling stage.

The optical lever method has not been tested yet due to time constraints and part availability. There are, however, some design considerations that should be described here. The island at the end of the cantilever, where the ring resides, is a square 200μm across, so the beam width at the cantilever should ideally be no bigger than this to minimize background light. This sets a lower limit of the beam diameter at the beam splitting 90-degree mirror. Another lower limit is imposed by the sharpness of the 90 degree edge of the mirror. This can be crudely modeled as an absorption area in which light disappears. An upper limit is set by the designed specification for deflection detection limit. If the beam becomes too wide at the beam splitting, resolution is lost because movement of the spot introduces a smaller relative change in beam power difference between the two sides.

A final note needs to be made on the diffraction properties of the reflected beam when hitting the 90 degree mirror, as shown in Fig. 3.21. The mode of the beam after the beam is split by the sharp edge is no longer gaussian, and the result is equivalent to edge-diffraction. If the beam path is long enough or the target fiber core small enough, the diffraction fringes of the beam would make placement of the fiber troublesome. However, the beam path length at which this becomes important is significantly larger than the approximately 20mm in the sample holder, and to further increase light coupled into the fiber a large-core multi-mode wide-angle fiber was chosen (400μm core, NA=0.39). This is only acceptable as long as the detection is done purely by power measurements as the phase information is lost by coupling into a multi-mode fiber. This approach to fiber coupling is therefore not available for the interferometer setup, where all fibers have to be single-mode and match the laser source. The multi-mode fiber is also better suited for in-coupling of non-Gaussian beams, as these can generally be more fully accepted by decomposition into the different allowed modes in the fiber.

Mechanical

The mechanical part of the sample holder has several purposes. It needs to provide sample mounting and electrical connections and optical connections. The optics of the sample holder also needs to be very adjustable as well as stable during cooling.

The beam position on the 90 degree mirror edge will change by approximately 50nm when the cantilever bends by 1nm at the point of reflection. Therefore very precise positioning of the 90 degree mirror edge is essential. There are two simple ways to obtain such precision in the positioning of the mirror; (1)mount the mirror on a a piezoelectric stack or (2)use a mechanical alignment system. The piezoelectric stack must be rather large to allow a significant displacement, and was therefore disregarded. A micrometer screw has not, at first glance, the precision needed, but by mounting the mirror with the sharp edge slightly angled away from perpendicular to the designed beam paths towards the two 45 degree mirrors, the precision is increased immensely. By having an angle 3 degrees away from perpendicular, the displacement is decreased by a factor of 20, improving precision by the same factor at the expense of range.

There is also a the matter of which position to choose as reflection point of the laser beam

off the cantilever. The displacement, and in particular the deflection angle, grows as the spot is moved closer to the cantilever free end. On the other hand, mechanical noise also increases when moving toward the free end. They do not do so uniformly, however, as the mechanical noise will tend to introduce resonant modes of the cantilever corresponding to an end-load rather than the end-moment introduced by the torque on the ring. For the interferometer, the displacement is the important factor, and for the optical lever method it is the angle change. The ratio of the effect of an end-moment load of magnitude M, compared to a simple end-load of magnitude P is [68, 47]

$$\frac{u_M(x)}{u_P(x)} = \frac{3M}{PL(3-x/L)} \tag{3.18}$$

$$\frac{\theta_M(x)}{\theta_P(x)} = \frac{2M}{PL(2-x/L)} \tag{3.19}$$

where L is the length of the cantilever, x is the distance from the fixed end of the cantilever and it is assumed, that the load is placed at $x = L$. For both cases, it is seen that the closer to the end of the cantilever the laser is focused, the better signal-to-noise ratio when it comes to mechanical noise. To accommodate all cases, the fiber-holder for the optical lever light input is mounted in a track on the sample holder. It can be moved along the track, which moves the spot along the cantilever length. In the same track, the interferometry fiber is mounted. It is possible to focus the two beams on the same spot or not, independently. The sample and the sample holder is seen in Fig. 3.27.

Samples

The samples made for the single ring experiments are mechanically identical, the microcantilever is 2000μm long, 45μm wide and 1μm thick. At the end of the cantilever is a 200 × 200 μm island where the superconducting system is placed. The system can be either a ring or a square, both having a width of 3μm. Several sizes of the systems are available, with lengths of 125μm, 250μm, 500μm and 756μm. The 3μm × 3μm Josephson cross junction thermometers are placed near the corners of the island. The mechanical eigenfrequency of the cantilever is approximately 500 Hz, estimated from finite-element simulations and analytical expressions, which requires the cantilever to be very well isolated from the surroundings, mechanically. This can be done by suspending the entire cryostat from the ceiling using rubber bands. It will likely also be necessary to acoustically isolate the system as much as possible by having very low exchange gas pressures in the cryoprobe.

3.5 Software

An important part of the work done in this project has been to automate data acquisition analysis. Although technically simple, it was a necessary component for the success of this project. The motivation for this is very simple. An enormous number of required heating/cooling cycles is needed to obtain reliable statistics - during this project several millions of cycles have been performed. Even the simplest analysis of this data will require a few seconds of human processing, yielding

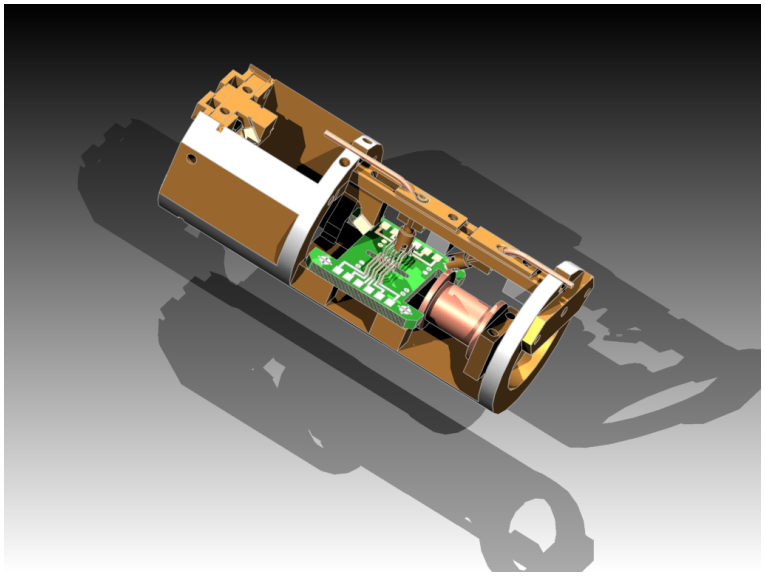

(a) The designed and manufactured sample holder for the single ring setup with optical detection. Both interferometric and optical lever detection methods are implemented. The sample is mounted under the green PCB board and the entire sample holder is suspended vertically with the right end of the cylinder-shape downwards. As a scale reference the diameter of the sample holder is 30mm.

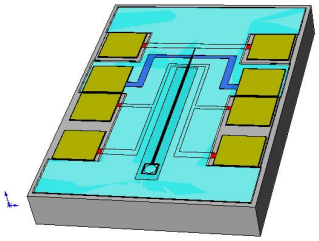

(b) Cantilever sample, rendered from photolithography masks. The integrated resistor is not shown, but is placed across the sample in the far end.

Figure 3.27: The final setup for the microcantilever detector setup.

analysis times in the several month range, even if working 24 hour shifts. Therefore automated analysis is necessary.

Some of the cycles need timing in the millisecond range, and is thus outside the reach of human capability, and even for the slower ones, reproducibility suffers if manual switching is performed (5-8 switches required per cycle, some of which time-critical). Therefore automated data acquisition is necessary. Actually, the very early proof-of-principle Kibble-Zurek measurements on annular Josephson junctions were performed manually by one very dedicated scientist[4], doing several thousand repetitions in a day. The current setup easily goes into several 100.000 cycles per day, depending on the selected quench times.

Finally, and most importantly, by performing the analysis in an automated way without user interaction, any experimentalist bias can be ruled out. This is particularly important for experiments, that are statistical in nature as all batches need to be evaluated using identical measures to obtain reliable statistics.

For these reasons several pieces of software were created to control the cycling, store the data and analyze the results.

[4]The author cannot take credit for this monumental achievement

3.5.1 Algorithms

For the different types of experiments, different algorithms have been produced to detect fluxons and quantify the quality of measurements.

Zero-field step detection

The detection of zero-field steps is done from the stored IV characteristics of the annular Josephson junctions, recorded after each quench. Several measures are calculated from this data to not only assign each IV characteristic to a category (no fluxon trapped, one fluxon trapped, ...), but also a quantification of the quality of the detection.

Ideal zero-field steps are characterized by a very low maximum zero-voltage (critical) current, large amplitude voltage steps at $\pm V_{ZFS_n}$m where n is the number of zero-field steps trapped, and identical height of the steps. The measures calculated are an attempt at producing a single number describing the extent to which the recorded IV characteristic conforms to each of the cases. For each IV characteristic dataset at each predicted zero-field step voltage for $n \leq 3$, the quality measure is calculated. The quality measure is defined as

$$Q_n = \frac{I_{max}(V_{ZFS_n}) - I_{min}(-V_{ZFS_n})}{2I_{max}(0)} \frac{I_{max}(V_{ZFS_n})}{-I_{min}(-V_{ZFS_n})} ,$$

if $\left|I_{max}(V_{ZFS_n})\right| < \left|I_{min}(-V_{ZFS_n})\right|$. Otherwise the last fraction is inverted. The first factor measures the height of the zero-field steps against the maximum zero-voltage current, and the second factor is a measure of the symmetry of the zero-field steps. The quality measures for $n \leq 3$ is saved in a data summary file. It is not necessary to examine $n > 3$, as this has never been observed in experiments. If one of the quality measures are significantly higher than the others the dataset is detected as having n fluxons trapped. The thresholds for the different Q_n are corrected for the overall decline in step height with increasing n. In addition, some post-processing and filtering is done to avoid single points in the dataset to result in trapping detections.

For $n = 0$ the quality is measured by the critical current divided by the maximum critical current found in the last N cycles, where N is large enough to leave insignificant probability of having trapped fluxons in every one. The advantage of normalizing to the last N in stead of the entire dataset is that it takes into account changing base temperatures, and other variations in the setup over long time-scales. Typically $N \approx 25$ which corresponds to 1-5 minutes. These should be taken into account separately to avoid changing measurement conditions across a batch. Of course, by this definition $Q_0 \leq 1$, so it cannot be directly numerically compared to the others. However, in experimental situations, the values are always unambiguous. This means that for all the several millions of quenches performed after the final optimization was performed, extremely few has more than one Q_n significantly different from zero. The Matlab[5] script responsible for this can be found in the Matlab folder on the CD distributed with this dissertation (see back cover).

In order to avoid systematic errors introduced by the analysis, the algorithm has been thoroughly tested against a large user-characterized dataset, and is continually checked by random tests in the datasets obtained. Through these tests, it is estimated, that the error on high quality

[5] See www.mathworks.com

datasets, is significantly smaller than the error introduced by uncertainty and drift in τ_Q (estimated at 10%). In this regard, high quality is defined as datasets in which the user had no ambiguity in identifying them by their number of trapped fluxons. For the data used in publications during this Ph.d project and all of the data shown in this dissertation, it is estimated that the number of ambiguous IV characteristics is less than 1 part in 10.000.

I_c detection

The zero-field step detection algorithm already measures the critical current as part of the quality measure. As the value for the maximum zero-voltage current is also automatically stored in the data summary file for each batch, the same script can be used directly. The only difference in these measurements is the acquisition of several IV characteristics at different values of the applied perpendicular magnetic field in the same quench before heating again. This part of the measurements are controlled by custom LabVIEW VIs - see Sec. 3.5.2.

3.5.2 LabVIEW

The second part of the software necessary for performing Kibble-Zurek measurements was the quench control and data acquisition program. This was been created in LabVIEW[6] for easy access to standardized instrument drivers and GBIP/DAQ cards from National Instruments.

VI for Kibble-Zurek measurements in the Josephson junction setup

For the standard annular Josephson junction Kibble-Zurek experiments, a LabVIEW program (called a Virtual Instrument, or VI), was needed. This controls the heating and cooling times, the height of the heating pulse through control of an external voltage supply and switching all of the relays connecting the junction leads to the amplifiers through an external switch box as well as the magnetic field coil current through an external current supply. The result is a rather complex VI, which is available on the CD distributed with the dissertation. A schematic of the entire setup with connections is shown in Fig. 3.19.

The VI allows the user to select heating, cooling and measurement times as well as heating voltage. It also has a pre-batch mode, where the relays are kept connected through the transition for recording the gap voltage as a function of time to extract information about the quench time, τ_Q. In addition, it allows splitting a batch into a number of sub-batches, each with a different applied perpendicular magnetic field strength. This is used to confirm the expected behavior of trapping as a function of magnetic field (see Sec. 2.2.5). In the latest version of this VI, the Matlab script for detection of zero-field steps is incorporated, allowing real-time analysis of the data after each quench. This also paves the way for further future automation, if so wished.

VI for measurements of junctions in oblique fields

The other main VI developed during this project is significantly simpler than for Kibble-Zurek measurements. The input taken is the range of angles to be measured, the range of magnetic field currents to use and the number of repetitions to be made at each angle and field current.

[6] See www.ni.com/LabView

The VI controls two separate current supplies for two orthogonal field coils mounted in the sample holder around the sample. It also takes the coil factors of the field coils as inputs to allow the use of field coils, that are not identical. This is important, as their geometry is necessarily different and so is their individual placements relative to the magnetic shield (see Sec. 2.6).

3.5.3 Comsol simulations

The commercial finite-element simulation package, Comsol Mutiphysics[7] was used for several simulations during the project. In this section, the different simulations are described.

Field coil enclosed in superconducting shield

For the results described in [44], magnetostatic simulations were conducted. As the problem is axisymmetric about the axis of the coil, the simulations can be reduced to the z-r plane, where the z-axis it along the symmetry axis. The coil was modeled as a region with a constant current density, and the superconducting can shield was implemented with a boundary condition. The boundary condition on the shield surface is simply magnetic insulation, $H = 0$. It was found, that the open top of the superconducting can has insignificant influence on simulation results because of the length of the shield. The simulation is somewhat faster by closing the top of the shield as the volume to be simulated is reduced considerably.

The geometry used is shown schematically in Fig. 3.28. For each geometry, the field in the coil center was determined, and this compared to the case with $R, \Delta h \to \infty$.

Josephson junctions in oblique fields

Comsol Multiphysics was also used for the simulations concerning the effect of out-of-plane magnetic fields on electrically small Josephson junctions. In this case, the system has a reflection symmetry, as all the junctions have at least this symmetry, but the simulations complete in only a few seconds without optimization. For this reason it was thought to be an unnecessary complication to exploit this symmetry, so the model was implemented in a full 3D space.

The model is of Josephson junction with its largest dimension much smaller than λ_J, so it is assumed, that the Josephson junction area is non-magnetic. Therefore, the problem is solved, by simply looking at the field around the superconducting electrode structure, at different field directions. The superconducting electrodes are modeled as perfect diamagnetic areas. Because of memory limitations and the very large aspect ratio of the junction area, the minimum junction thickness, that could be simulated, was $d_{ox} = 1\mu m$. The physical thickness in a real Josephson junction is only a few nanometers, but the magnetic thickness is larger by twice the London penetration depth, λ_L, of the electrodes. For bulk Nb, this is approximately 2×40nm, but for sputtered Nb, it can be as large as 2×200nm, which makes the simulation off by only a factor of two. The magnetic field is set to be in the specified direction on a border approximately 1mm away from the junction.

[7] www.comsol.com

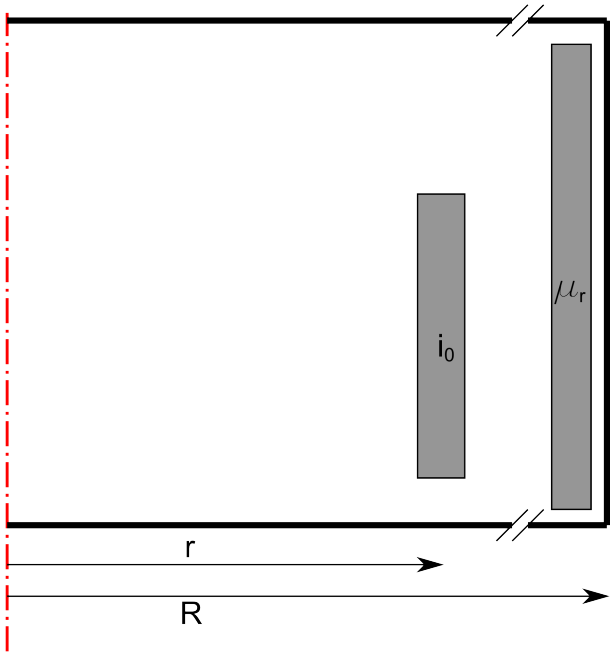

Figure 3.28: The geometry used in the simulation of the confined field coil. The red dash-dotted line is the symmetry axis and the bold black borders signify the magnetic insulation boundary condition. The radius of the shield, R, and the space between the coil and the bottom of the shield, Δh was varied during simulations. For the simulations involving the high-permeability sheet, this was put at a distance one millimeter away from the superconducting shield, with a fixed thickness of 0.5mm.

The simulation solves for the magnetic vector potential as a function of space coordinates and derives all other properties from this solution. An example of the annular overlap geometry simulated in a transverse magnetic field with magnetic field lines plotted, is shown in Fig. 3.29.

3.5.4 Matlab simulation of simple causality

As a crude example of simple causality and the speed of information, a game was thought up for a students' night at DTU Physics, see App. E.2. Based on the success and the simplicity of this example, a similar game was simulated in Matlab.

The simulation consists of dividing space into discrete regions and assign each box a color from a set. From here on, information transfer is modeled by making each box change color in a democratic way. This means, that each box changes to the color, that the majority of its neighbors has. In case of a tie, the result is chosen at random between the ones with most votes.

Regardless of the number of members in the color set, N_c, the equilibrium state is the single-color state. It is N_c-fold degenerate, as there is no bias towards any of the states, insofar as the initial distribution is uniformly random. This is the basis of the similarity, although extremely simplified, to the Kibble-Zurek symmetry-breaking phase transition. The system will tend to slow down once clear borders between different domains begin to build. Actually, the total number of

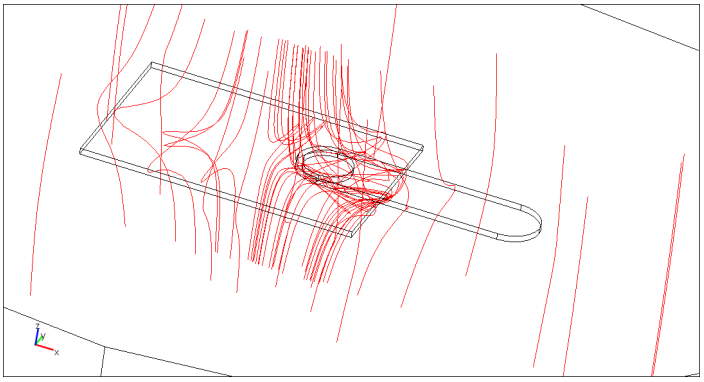

Figure 3.29: An example plot of the field solution to the transverse field problem in an annular overlap junction. The lines are randomly selected magnetic field lines. It is seen how the initially transverse magnetic field lines are converted into field lines going through the junction area directly below the ring electrode. Some of the field lines seem to pass through the electrodes, but this is an artifact of the streamline algorithm for generating the field lines from the magnetic vector potential and the somewhat coarse grid. Evaluating the field strength found inside the electrode volume, it is always zero as set by the boundary conditions on the electrode surfaces.

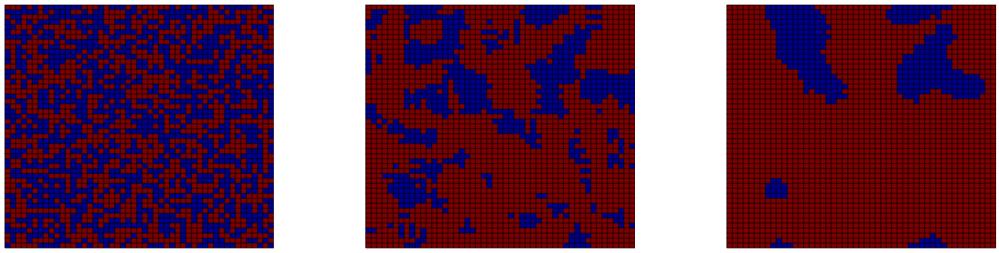

Figure 3.30: The simple simulation of causality effects using two dimensions and a color set with two colors. The grid is 50 by 50, and the times plotted are $t = \{0, 2, 10\}$

color changes in a timestep must be an increasing function of the total length of the borders, as the length is proportional to the number of possible sites for a color change. This is also in qualitative agreement with the Kibble-Zurek scenario, where borders tend to be stable. As this numerical experiment is meant to have, at best, a qualitative similarity to a Kibble-Zurek scenario, no attempts have been made to justify it quantitatively. An example of the time evolution of this system in two dimensions, with $N_c = 2$ is shown in Fig. 3.30.

To compare to the Kibble-Zurek scenario, the average size of domains, $\bar{\xi}$ must be found. It is easy to show, that the mean size of domains is inversely proportional to the total length of boundaries in the system, regardless of the dimensionality of the simulation. The total length of boundaries in the system is computed as the sum over the whole system of faces each discrete box has, where the neighbor is different - divided by 2 as each border is counted twice. To test whether the similarity extended to critical scaling, it is possible to stop the simulation at different cut-off

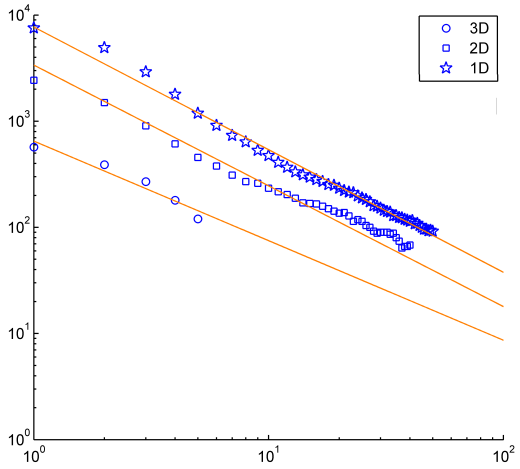

Figure 3.31: Plot of observed scaling in an extremely simplyfied Kibble-Zurek analogue. The data has been cut off when the boundary length of about 100 was reached, as the variation becomes noisy beyond this point. The prefactors are different, because of different dimensionality and different absolute sizes of the systems simulated.

times (similar to $\bar{t}$ in the Kibble-Zurek description). The total boundary length can then be plotted as a function of the number of time steps taken. In general, according to Kibble-Zurek theory, the number of defects produced in a quench is proportional to $\bar{\xi}^{-\sigma}$, where $\sigma \geq 0$. A direct comparison to the simple simulated system can thus be made, by simply plotting the total boundary length as a function of cut-off time. This has been done in Fig. 3.31, and the result is somewhat surprising. Scaling with a scaling exponent, $\sigma_S \approx 1$, is seen for both the 1D, 2D and 3D cases. The result is particular surprising, when considering the features of the simulated system particularly different from the Kibble-Zurek description. While the speed of information, $\bar{c}$ can probably be defined to be simply $\bar{c} = 1$ in this system, the equilibrium domain size cannot be easily defined, as it would simply be infinity for all times. Also, an essential component in the Kibble-Zurek scenario - the fluctuations, thermal or quantum in origin - are not present at all.

In any case, it is important to stress, that this simulation is only an illustration of the effect of the speed of information, and the analogy to a Kibble-Zurek phase transition should not be pushed too far. It is included as an example of how simple a system can be, and still exhibit scaling behavior. For a much more realistic implementation of domain dynamics in systems undergoing first order phase transition by bubble nucleation, see [73].

4 Results

In this section, a representative part of the data from the project is presented. The data is complimented by objective descriptions. For interpretation and conclusions, please refer to chapters 5 and 6.

4.1 Josephson junctions in a magnetic field

4.1.1 Transverse field

It was discovered, that the magnetic field influence of some Josephson junctions was much stronger for transverse fields than for in-plane fields, when doing Kibble-Zurek measurements. The effect was first discovered for the annular overlap geometry, in which the modulation of trapping probability with applied magnetic field was much faster than for an in-plane field. It was speculated, that this might be because of magnetic focusing caused by the electrodes during the transition. For this reason, measurements were done to find the critical field of different Josephson junction geometries in perpendicular fields and compare to the values for standard in-plane fields. One of the initial measurements are shown in Fig. 4.1.

It is seen, that the shape is similar, indicating that the field distribution in the junction area is similar to the distribution for the in-plane field. Additionally, the modulation by the transverse field is seen to be approximately 40 times faster than that of the in-plane field. From the simulation, it is possible to directly plot the magnetic scalar potential (as there are no free currents) as well as the field lines. A plot of this is seen in Fig. 4.2. It is seen, that for most of the width of the junction, the field lines are essentially parallel to the electrodes, as one would see it for an in-

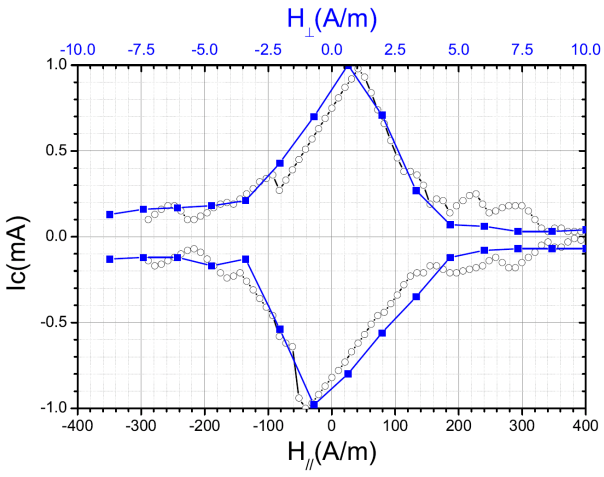

Figure 4.1: Comparison of the response of a simple overlap Josephson junction to magnetic fields applied in the perpendicular direction(blue) and in-plane direction(black). The junction width is 500μm and overlap length is 4μm. Note the difference in magnetic field scales[41].

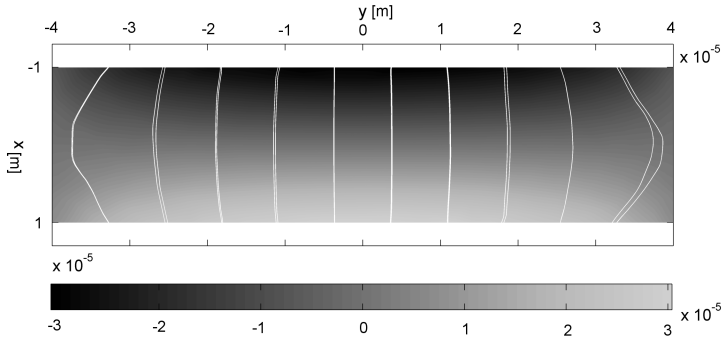

Figure 4.2: The magnetic field lines for a simulation of an overlap Josephson junction with a transverse applied magnetic field. The magnetic scalar potential[a.u.] is plotted on the background. The scalar potential is proportional to the applied field strength. The electrodes are of equal width, W = 80μm and the overlap length is 20μm[41].

plane field perpendicular to the long dimension of the junction. Only the corners are significantly different from the in-plane expectation. This is in good agreement with the conclusion reached from comparing the magnetic patterns of the critical currents. From these results, it is reasonable to expect that for an overlap junction the smaller the aspect ratio, $\beta = L/W$, the more the field induced in the junction from a transverse applied field will be like that of an in-plane field.

The simulations were carried out for overlap, cross, Lyngby and annular overlap junction geometries and analytic approximations were found to the field and resulting Josephson phase. For more information and results from the other geometries, please see [41].

As described in Sec. 3.3.3, this effect can also be used to predict the possibility of discriminating fluxons from antifluxons trapped in annular overlap Josephson junctions. This prediction has later been verified in the laboratory by inducing trapping in a certain direction through the application of an external magnetic field to a junction of the annular overlap JJ3 type. This was done several times in each direction, and the magnetic patterns shown was recorded. In all cases with trapping, the asymmetry was found with the predicted direction. For convenience this is shown in Fig. 4.3, which was also shown in Sec. 3.3.3.

4.1.2 Oblique field

The dependence of a Josephson junction critical current on an in-plane field has been solved analytically for rectangular junctions[29, 54]. Likewise, from Sec. 2.5 and 4.1.1 the effect of a transverse field is known, either through simulations or analytical approximations to their results. The Maxwell equations are linear in the fields, assuming that the material parameters in the system are constant with regard to the fields. In this case, with relatively weak fields, it is safe to assume that this is the case. This means, that from the previously known results and the ones of Sec. 2.5 and 4.1.1 a full characterization of a Josephson junction in an arbitrary field direction can be obtained by simply superpositioning the field solutions obtained individually for the different field directions. The field solution components must be weighed according to the angle of the applied field using standard trigonometry.

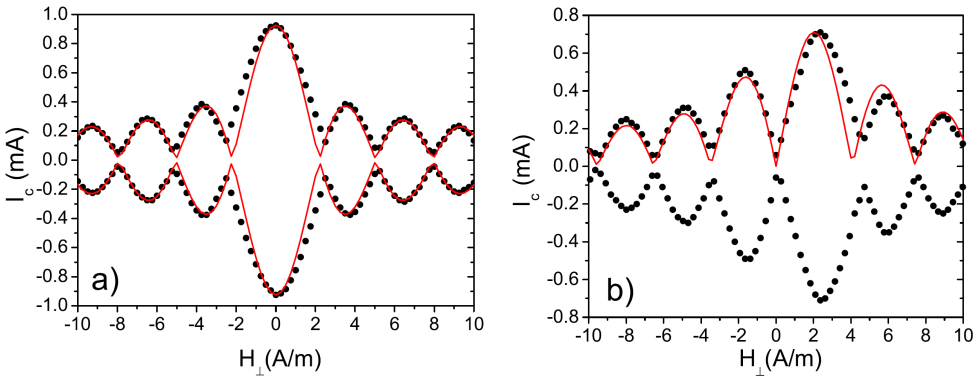

(a) No fluxon trapped (b) One fluxon trapped

Figure 4.3: The predicted and measured $I_c(H_\perp)$ dependence in an annular overlap Josephson junction. The prediction is made from magnetostatic simulations on the annular overlap geometry. The asymmetry is evident when one fluxon is trapped, and in the case of an antifluxon, the picture is simply mirrored around $H_\perp = 0$. Reproduced from [41]

This is done in [42] to obtain the width of the central peak, Δ_R as a function of field direction. The field is applied parallel to the electrodes and at an angle to the junction plane. The width of the central peak, Δ_R, is closely related to the first critical field of the junction, but more generally defined - see Sec. 3.3.4. Different junction geometries were characterized by recording their critical current as a function of applied magnetic field amplitude and direction. A typical example of the recorded data is shown in Fig. 4.4. This is recorded from a square overlap junction, for which a simple Fraunhofer diffraction pattern is expected at parallel fields. The complete characterization of a junction is completed in approximately 30 minutes to avoid any thermal drift in the system affecting the results.

Fig. 4.4 shows that the pattern widens to a maximum width at an angle around 140^o. The definition of α can be seen in Fig. 3.11(b) on page 46. This widening is effectively a measure of reduction of the sensitivity of the junction to magnetic fields. This can be understood as a reduction of the junction field by opposing components due to the in-plane and transverse fields. The degree to which these can compensate is given by the individual field solutions of the different directions. If the field inside the junction resulting from a transverse field is identical to that from a parallel field, complete cancellation should be possible at a certain angle, resulting in a critical current completely unaffected by the application of a magnetic field in this direction. Taking the example from Fig. 4.2, it is obviously similar to the expected in-plane field inside the junction. In this geometry, especially for $\beta \to 0$ where the corners will play a smaller role compared to the center, one would expect almost perfect cancellation. The angle of maximum cancellation can even be predicted either from numerical simulations, or from simple measurements. The measurement approach requires only two measurements to be done, for determining Δ_R at parallel and transverse fields. The ratio of these gives the ratio of the field components necessary to achieve cancellation, which yields the cancellation angle by simple trigonometry (inverse tangent of the ratio). This was done for different overlap, cross and annular geometries and presented in [42]. In

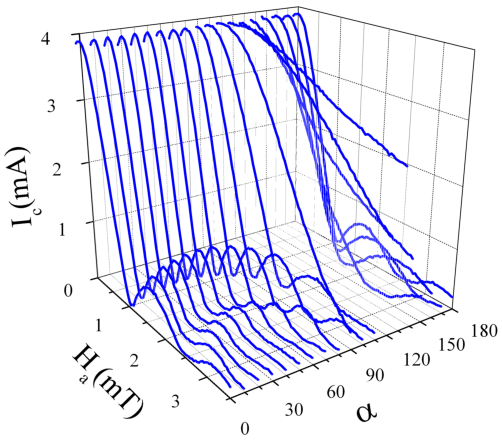

Figure 4.4: The magnetic field dependence of a square overlap junction. The angle to the junction plane is α. For $\alpha = 0$ the expected Fraunhofer pattern is seen[42].

Fig. 4.5(a) the results are shown from both the calculation, the simple theory based on measurements of the in-plane and transverse Δ_R, and recorded data from a Nb-Al/AlOx-Nb Josephson junction. As seen, the simple theory captures almost perfectly the entire dataset, and the calculation based on analytical approximations to the field solutions does slightly better in the area of maximum cancellation. The correspondence at $\beta = 1$ is not quite as good but still much better than qualitative, and even for $\beta = 4$ the angle of the maximum is predicted correctly, although too high by a factor of two.

The technologically important square cross junction ($\beta = 1$) is shown in Fig. 4.5(c). This is interesting, as square cross junctions are commonly used for calibration purposes and is an important component in measuring the magnetic penetration depth, λ_L, for Nb. For $\beta = 0.25$, as seen in Fig. 4.5(d), a maximum of $\Delta_R/\Delta_R^{\parallel} \approx 6$ is exhibited slightly shifted away from the predicted $\alpha = 90^o$. This is surprising as the symmetry of the system dictates symmetry of the magnetic response. This is most likely due to slight misalignment between the junction and the center of the cross defined by the electrodes. The reason, why the cross junctions show significantly less cancellation than the other geometries shown, is that the field solution for a cross junction in a transverse field is very different from that for an in-plane field. In fact, an analytical solution to the problem of a square cross junction in a transverse field was found a long time ago[56]. In [41] a different analytical approximation is found. Here it is shown, that the result in [56] can be obtained by Taylor expanding the analytical approximation found from the simulation data.

Finally, for the annular Lyngby junction geometry, a somewhat surprising result is seen. Strong cancellation is seen, even stronger than for an overlap junction with $\beta = 0.008$. This surprising result comes from the fact, that the radial component of the magnetic field in the junction annulus, varies almost perfectly sinusoidally, as seen in Fig. 3.9 on page 43. The same dependence would be seen for a magnetic field parallel to the electrodes.

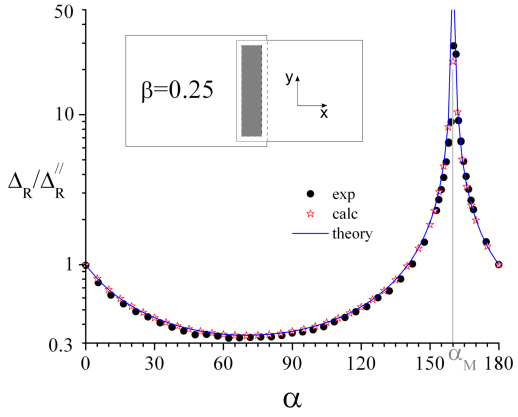

(a) Overlap geometry junction. The cancellation is almost perfect at $\alpha = 165^o$ yielding a junction almost completely insensitive to the magnetic field.

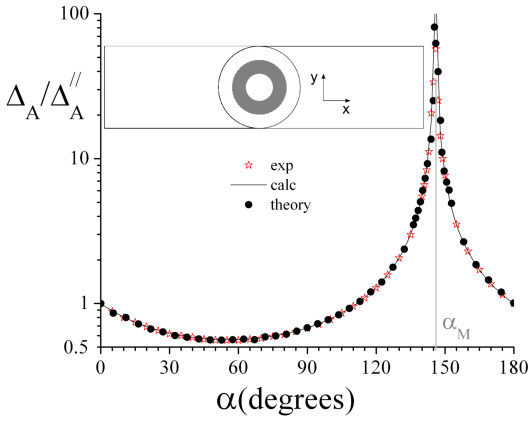

(b) Lyngby geometry junction.

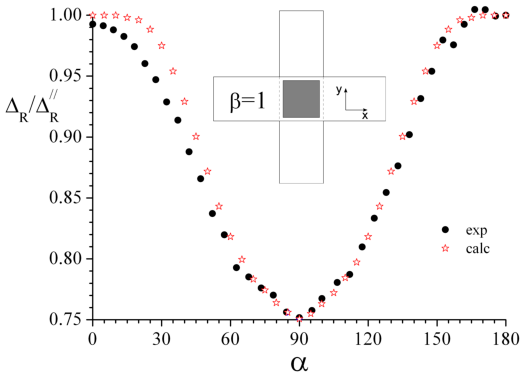

(c) Square cross junction.

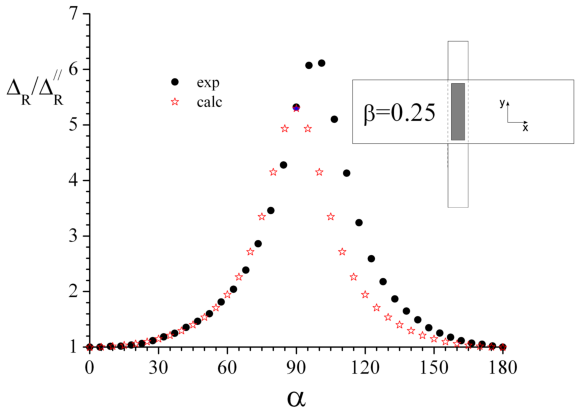

(d) Rectangular cross junction.

Figure 4.5: The angular dependence of the magnetic width, Δ_R, normalized to its in-plane value, for four different junction geometries. The insets show the geometries in question. The predicted values for maximum cancellation from the simple pseudo-analytical calculation is marked by α_M. Note the logarithmic vertical axes on the two top plots. Figures from [42].

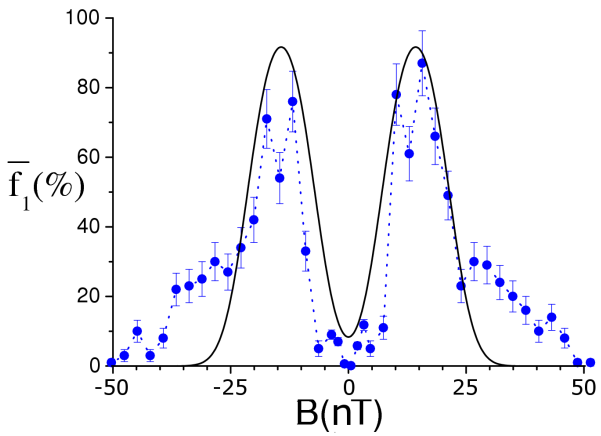

(a) 500μm annular overlap junction after slow quench, τ_Q = 5s. The solid line corresponds to the case $N = 1$

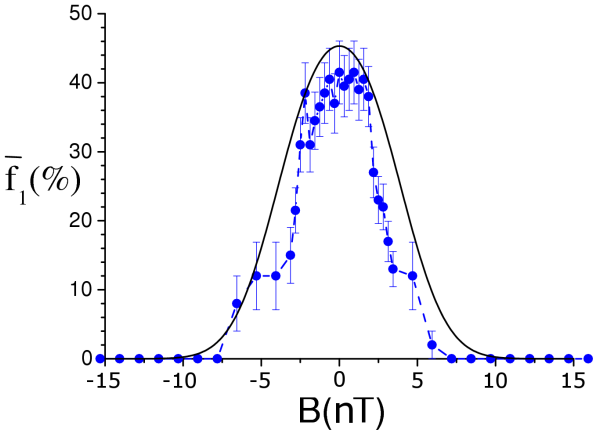

(b) 2000μm annular lyngby geometry junction after a slow quench, τ_Q = 5s. The solid line corresponds to the case $N = 16$.

Figure 4.6: Magnetic characterization of trapping probability in annular Josephson junctions of different lengths. The solid lines correspond to the predictions made in Sec. 2.2.5 and Fig. 2.4(a). The junctions have identical production parameters, and are from the same wafer. The scale of the horizontal axes for the fits is chosen to best fit the experimental data. Figures reproduced from [18], but corrected for the effect of the superconducting shield on the coil.

4.2 Quenched AJTJs

The most important results obtained in this work comes from annular Josephson junctions cycled repeatedly through the phase transition temperature. A total characterization of the system's quench time scaling exponent, σ, requires the determination of the trapping probability at a number of different quench times. A quench time is experimentally set by choosing heating parameters, such as the heating and cooling times and the heating power.

For each quench time, a magnetic characterization of the trapping is performed. It consists of measuring the single-fluxon trapping probability as a function of applied magnetic field transverse to the annular junction in the cooling phase. The results of two typical magnetic characterization experiments are shown in Fig. 4.6 for a 500μm annular overlap junction, and 2000μm Lyngby gemoetry junction.

For each quench, an IV characteristic is recorded using a low-frequency (1-30Hz) bias current sweep. Two typical recorded IV characteristics are shown in Fig. 4.7 with either zero or one trapped fluxon detected.

The recorded IV characteristic datasets are analyzed and classified by their number of trapped fluxons to give the trapping probability f_m as a function of applied field and quench time, τ_Q. Most of the Kibble-Zurek measurements in this project was done on the 500 μm circumference annular overlap Josephson junctions, and for these it was found, that f_2 was insignificant for all quench times and applied magnetic fields. However, for some cases double fluxon trapping might have been overlooked due to decreased data quality for quenches in higher magnetic fields. In all

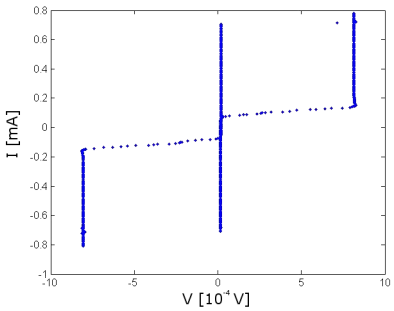

(a) No trapped fluxons detected. The voltage amplifier saturates at a voltage of about 800μV, so the curve is compressed for voltages numerically above this.

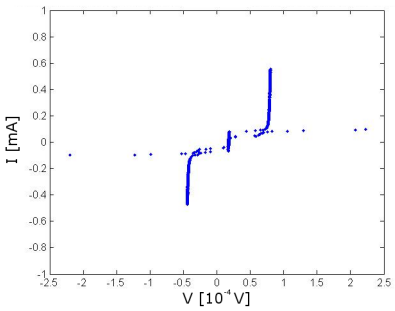

(b) One trapped fluxons detected. The offset in voltage is caused by the voltage preamplifier.

Figure 4.7: Recorded IV characteristics after two different quenches in the same batch. The junction used is an Nb-Al/AlOx-Nb junction, of annular overlap geometry with a junction length of 500μm.

cases, the magnetic field predicted to induce trapping is significantly smaller than the first critical field of the junctions in the transverse direction and orders of magnitude below the critical field of the electrodes.

The single-fluxon trapping probability $f_1(\tau_Q)$ for zero magnetic field in the standard 500μm annular overlap junction geometry is shown in Fig. 4.8. It is seen, that critical scaling of the trapping probability as a function of quench time is robust across 3-4 decades of cooling rates, with a possible saturation beginning in the lower end of the quench time range. Furthermore, no difference is observed between the JJ3 and JJ4 flavors of the annular overlap geometry, nor between samples of identical geometry, thus ruling out sample-specific effects.

To check the scaling with circumference, another series of measurements were performed on a 1500μm annular junction of the Lyngby geometry from the same wafer as the 500μm samples. The results are seen in Fig. 4.9, and shows identical scaling exponents of $\sigma_{AJTJ} = 0.5$ across the entire range of applied cooling rates. However, the prefactor is changed from $0.01 \pm 10\%$ for the 500μm junction data to $0.018 \pm 10\%$ for the 1500μm junction.

4.2.1 Asymmetric junctions

The data obtained from the available Nb-Al/AlOx-NbN-Nb junctions were hard to interpret, mainly because of many voltage steps not being symmetrical or having very low height. This was most likely caused by trapping of flux in the superconducting sandwich structure during quenches, and from the complex interplay possible with three different superconducting rings going through their transition at slightly different times. It was also found to be very difficult to create heating pulses, that would heat the Nb rings above 9.2K and keep the NbN ring below 13.4K, resulting in memory effects of trapping. This can also be caused by the impressive stability of defects, even to heating above T_c as described in [20]. Here, the authors state, that the temper-

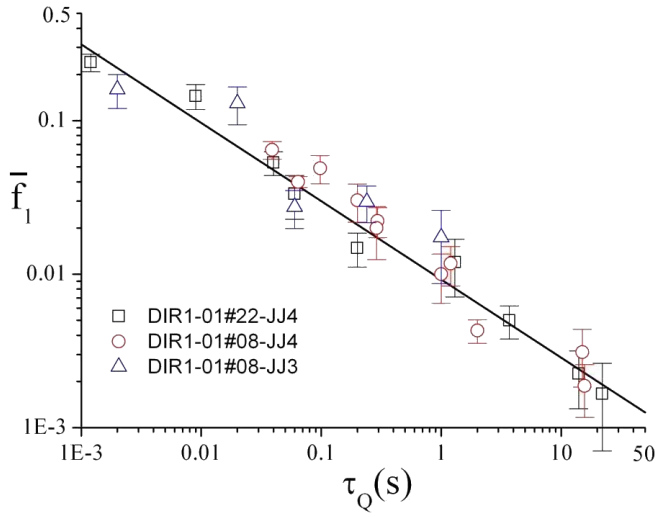

Figure 4.8: The main result of the Kibble-Zurek measurements done on symmetric Nb annular overlap Josephson junctions. It shows the probability of cooling into a single-fluxon state as a function of the quench time, when no external field is present. The scaling exponent of the power-law fit is $\sigma_{AJTJ} = 0.51 \pm 5\%$ and the prefactor is $a = 0.01 \pm 10\%$ [33]. Data from both the JJ3 and JJ4 flavors of the 500μm annular overlap geometry is shown. The statistical uncertainty is shown as errorbars on the markers, and the width of the markers is the apprixmate uncertainty in the determination of τ_Q. Note the logarithmic axes[34].

ature should be raised significantly above T_c to completely erase the topological defects. Whether this is an artifact of the rather unphysical heating scheme used in the simulations or more general physics remains to be seen. It cannot, however, be ruled out as a cause for the failure, so far, of the Nb-Al/AlOx-NbN-Nb junctions to produce reliable data. Finally, the critical current density of the Nb-Al/AlOx-NbN-Nb junctions were almost 2 orders of magnitude larger than the symmetric Nb junctions, making them significantly different, electrically, from the symmetric junctions. This increases the expected number of domains formed in rings of identical circumference by the same factor.

If the data is processed as the data from the Nb junctions, and the detection thresholds reduced to allow more exotic zero-field step shapes, a scaling was observed, however with different sign. This means that for lower values of τ_Q the probability of single-fluxon trapping decreases. For all experiments performed, the trapping probability was significantly higher than for the symmetric Nb junctions. This data should not be trusted too far for the reasons given above.

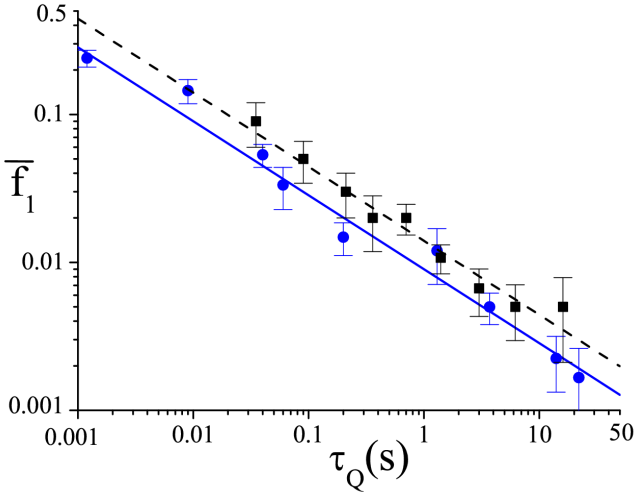

Figure 4.9: Test of the circumference scaling of the trapping of single fluxons in symmetric Nb annular Josephson junctions. The plot shows the probability of cooling into a single-fluxon state as a function of quench time when no external field is present for two different annular junction lengths and geometries. The blue circles are measurements done on a 500μm annular overlap junction and the black squares are results of measurements done on a 1500μm Lyngby geometry junction. The straight lines are power-law fits to either dataset. Note the logarithmic axes[18].

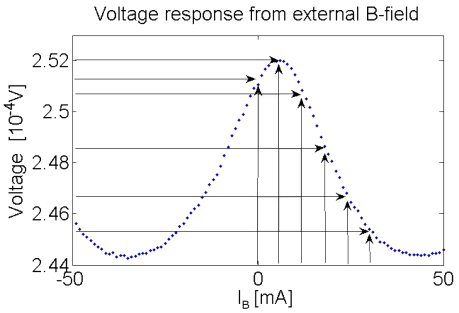

(a) The SQUID response to a weak external magnetic field. The horizontal axis is the coil current supplied to a single loop coil around the sample with a 30mm diameter.

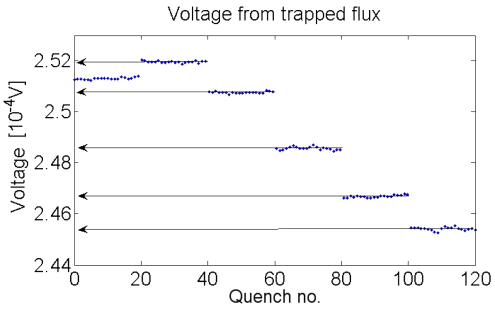

(b) The SQUID signal from several very slow cycles of a single ring with applied magnetic field.

Figure 4.10: Data from the single superconducting ring SQUID experiment. The data in (b) shows the signal measured from slow cooling experiments, with applied magnetic field corresponding to integer numbers of flux quanta per ring area[46].

4.3 Single superconducting ring with SQUID readout

Although the experiment on the single superconducting ring is still mostly a proof-of-principle experiment, some initial data was measured to show that the system is truly capable of detecting single fluxoids trapped in the superconducting ring. The result of a calibration experiment can be seen in Fig. 4.10. The calibration consists of running batches of 20 cooling cycles with different applied magnetic fields transverse to the ring. The cycles are very slow, to reduce Kibble-Zurek trapping events and only allow induced trapping to occur. The applied magnetic field strengths were selected to match approximately the field corresponding to integer numbers of flux quanta in the ring. When recording the SQUID signal, the applied magnetic field was turned off, so only the remaining field from superconducting ring was measured.

As is seen, the SQUID noise is significantly smaller than the separation of individual fluxoid state plateaus. This shows, that the SQUID setup is sensitive enough to measure single fluxoids trapped in the ring. The induced trapping mechanism seems to be very stable as well, as no fluctuations in the signal are seen. This is an indication, that the SQUID itself is quite stable, and that the Kibble-Zurek trapping of fluxoids is reduced to significantly less than $1/20$.

The range of the SQUID setup, as currently realized, is approximately ± 3 fluxoids. For changes in trapped fluxoid number larger than this, the periodicity of the SQUID signal reduces the ability to distinguish different trapping numbers. This will, eventually, lead to a lower limit of τ_Q, that can be reliably measured using the current setup. By improving the SQUID noise level, a weaker coupling could be accepted, and this range could be increased. For now, this is not the limitation of the system.

The equal spacing of the detected magnetic fields in the SQUID is a good indication, that an integer number of fluxoids were trapped in the superconducting ring in each experiment. The spacing of the single-fluxoid levels in the SQUID compared to the full period of the SQUID gives

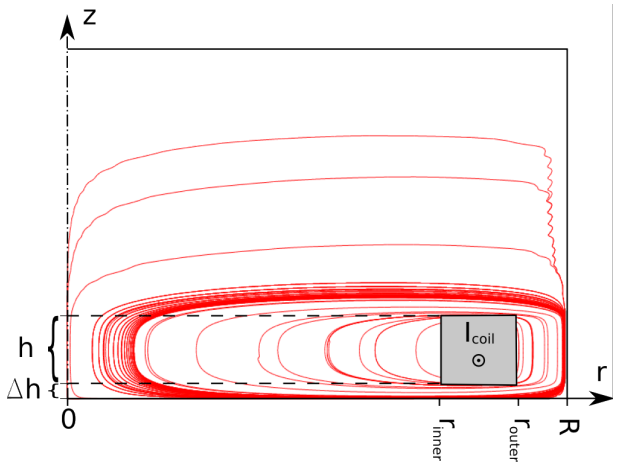

Figure 4.11: The result of a simulation of the central magnetic field of a field coil in a close-fitting superconducting shield. The plot shows magnetic fieldlines to illustrate the compression of the magnetic field. Note that the axes are not to scale. For this simulation, Δh = 5mm and Δr = 2mm.

a flux coupling coefficient of approximately 1/12 from the ring to the SQUID in the current setup.

It is seen from Fig. 4.10(a), that the magnetic field in the sample holder is not quite zero, as the curve is slightly shifted towards the right. In this particular case, it seems that the shift corresponds to the SQUID signal of approximately one fluxoid in the ring, which is equivalent to

$$B_0 \approx \frac{\frac{h}{2e}}{12A_{SQUID}} = 6.6 \times 10^{-9} T \,,$$

where the factor of 12 comes from the flux coupling coefficient between the ring and the SQUID. Theoretically, it might also be, that the field is offset by this value plus an integer number times the field period of the SQUID. Fortunately, according to the theory of Sec. 2.2.5 and [18], this does not in itself render Kibble-Zurek measurements unfeasible. However, this is only true for static B-fields in general, and even more so for this experiment, as the field is assumed constant across extended batches of cooling cycles, meaning that even very slow changes in ambient magnetic field would be a problem.

4.4 Coil in a shield

Many different geometries of the superconducting shield surrounding the field coil was simulated. Each geometry is defined by the set of values (Δh, Δr). The geometry of the field coil is identical for all simulations, with h = 50mm, r_{inner} = 15mm and r_{outer} = 18mm. For each of the simulated geometries, a total field solution is found. An example of this can be seen in Fig. 4.11. The oscillating lines in the top right quadrant are the result of the coarse mesh in this area.

The field lines illustrate, that very little field is present in the far end of the shield, which verifies that closing off this end as well has negligible effect on the field solution. It is also seen,

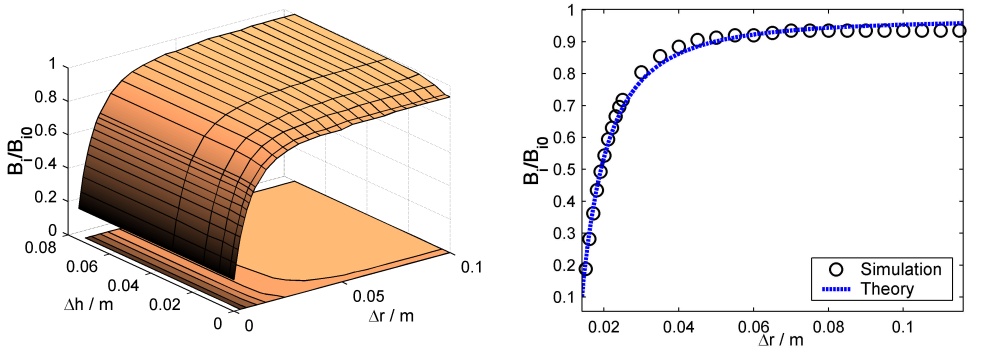

(a) The simulated dependence of the magnetic field in the center of the field coil as a function of axial distance to bottom of can, Δh and radial distance to can, Δr. All results are normalized to the simulated value when no shield is present, B_{i0}.

(b) Comparison of the radial distance dependence of the field coil magnetic field for Δh = 25mm, to the theory developed for an infinite solenoid in a superconducting cylinder.

Figure 4.12: The simulation results from the field coil in a superconducting shield simulation. The simulated field coil has a height of 50mm, an inner radius of 15mm and an outer radius of 18mm[44].

that the field is strongly compressed in the area close to the superconducting shield outside the field coil.

The simulation results of the finite field coil in a superconducting shield are shown in Fig. 4.12. The simulated coil is of the same geometry as the coil used in the annular Josephson junction experiments.

For the geometry used in the Josephson junction experiments - both the Kibble-Zurek measurements and the oblique magnetic field measurements - $\Delta r \approx 2$mm and $\Delta h \approx 1mm$. Using the simulation results, it is estimated, that the field is reduced by a factor of 10 in the cryoprobe as compared to the coil in free space. This illustrates the necessity of either using simulations or in situ calibration of field coils, when using superconducting magnetic shields. The superconducting shield might have an even more important effect, through distortion of the magnetic field direction as well as its magnitude, when the sample is not inside the volume enclosed by the coil. As seen in Sec. 4.1.2, a slight change in the direction of the magnetic field can have order of magnitude effects on the measured parameters of some systems.

5 Discussion

Here the results of the previous section will be discussed and evaluated against theoretical predictions. Furthermore the errors introduced by statistics as well as non-ideal measurements will be discussed and their sizes estimated.

5.1 General

5.1.1 First or second order transition

A question of principle is whether the phase transition happening is of first or higher order. This is important for several reasons. First order transitions generally proceed by bubble-nucleation of the new stable phase in the unstable phase. Second order phase transitions are characterized by the unstable growth of fluctuations, which is what Zurek describes in [5]. While it is possible to handle Kibble-Zurek phase transitions theoretically[73] it requires a different framework from the one described by Zurek, and the formulation in terms of correlation lengths breaks down. Experimentally, the problem with first order phase transitions is that these generally have a finite energy difference between the different phases at the transition temperature. This means that there exists a finite latent heat of transition, which results in heat transfer. This heat transfer can easily become the limiting factor in the phase transition, rather than the phase ordering velocity, and poses a risk of causing thermal gradients. This is the case of the water-ice experiments described in App. E.1.

The problem is even more complicated for a multiply connected geometry, as trapping of a flux quantum in a hole through a superconductor requires the generation of shielding currents around the hole. This circulating current has a non-zero inductive and kinetic energy, that must be taken into account when comparing energy scales. This means, that at the time of transition, $\bar{t}$, it must be energetically favorable to go from a normal-state ring to a superconducting ring with a flux quantum trapped. Equivalently, the energy difference at $t = \bar{t} > 0$ between the superconducting and normal state must be greater than the energy penalty of generating the screening currents. On the other hand, for the generation of flux to be of Kibble-Zurek origin, the thermal energy available must be smaller than the the energy of a flux quantum to avoid thermal excitation of trapping.

The energy of a fluxoid trapped in a superconducting Nb ring close to the transition temperature is

$$E_{\Phi_0} = \frac{\Phi_0^2}{2L} = 6.3 \times 10^{-21} J \,,$$

where the normal-state inductance of a metal ring, L, has been used, as the superconducting part of the inductance goes to zero very close to T_c. The difference is about 20%. The energy available through thermal fluctuations at T_c are

$$E_T = \frac{1}{2} k_B T_c \approx 1.27 \times 10^{-22} J \,.$$

The transition into the superconducting state with a fluxoid trapped is thus shielded from thermal activation. The other condition can be evaluated directly by solving the equation

$$V\Delta g_0(T) = \frac{\Phi_0^2}{2L}\,, \tag{5.1}$$

for the temperature, where $\Delta g_0 = \frac{1}{2\mu_0}H_c(T) = H_c(0)(1-\left(\frac{T}{T_c}\right)\Big)^2)$[54], and V is the volume of the superconducting ring. The result is

$$\Delta T = T_c - T \approx 375\mu K\,,$$

where the positive solution below T_c has been used, and the analytical solutions are too long to present here. The deciding factor is whether this temperature is reached before or after $\bar{t}$, when the phase transition takes place. The cooling rate is characterized by τ_Q, and the inequality

$$\Delta t = \frac{\tau_Q}{T_c}\Delta T < \bar{t} = \sqrt{\tau_0\tau_Q}\,, \tag{5.2}$$

can now be solved. Here Δt is the time it takes for the system to cool by ΔT as defined above. The solution is

$$\tau_Q > \frac{T_c^2\tau_0}{\Delta T^2} \approx 1\text{ms}\,.$$

For τ_Q below this limit, the flux production is expected to be suppressed by lack of available energy to generate the necessary screening currents. This calculation is certainly only a crude approximation, but it does give an indication of a lower limit in τ_Q, that can be realized while keeping the Kibble-Zurek picture intact. The fastest quenches used in this project are on this order, and looking at the results in Fig. 4.8, there does seem to be some saturation, although data is very limited, and other limiting factors also exist in this region.

This calculation is performed for a single superconducting Nb ring, and as such do not directly correspond to the experiments on annular Josephson junctions. The main problem in translating this to fluxons in annular Josephson junctions lies in the estimation of the energy related to a fluxon and its dependence on temperature - as opposed to a fluxoid in a ring, where this is rather easily obtained from existing theory. A similar relation must exist for fluxons, although the inductance L is probably different. The thermal activation threshold is likely larger than the above, as any flux must still pass through the electrode ring to get to the Josephson boundary.

5.1.2 Thermal gradients

Thermal gradients were investigated in two different types of simulations in Sec. 3.2.4. The simplest one, which attempts to find the thermal equilibration time for the silicon sample itself, sets the limit that

$$\tau_Q \gg \tau_{eq} \approx 5\mu s\,.$$

The second, more realistic looks at the thermal gradients on the surface of the sample while it is undergoing a full heating cycle and is mounted to a copper support of the same geometry as

the actual sample holder. Exchange gas cooling is ignored as it is rather complicated to include, and has only a small effect on cooling rates, as seen in the experimental data in Fig. 3.4. In this system, the thermal coupling between the sample and the sample holder was tuned to obtain realistic thermal responses of the sample to typical heating pulses. The response was evaluated against experimental data for these heat pulses, and the quench time was compared. No fine-tuning was performed of the coupling constant, except to obtain approximate agreement. In these simulations, the thermal gradients can be directly extracted for heating cycles comparable to those in the actual experiments.

The results obtained in this experiment show that the the limit of acceptable thermal gradients are reached for

$$\tau_Q \approx 10ms\,,$$

depending on the model for the phase transition. For the annular Josephson junction phase transition using the approach in [34], this limit can be pushed down by at least an order of magnitude.

Some evidence of this can be seen in the $\bar{f_1}(\tau_Q)$ data for $\tau_Q < 10$ms in Fig. 4.8, although the data is too limited for any conclusions to be drawn. Also, the heating system is pushed to its limits in this τ_Q range, and reproducibility of the pulses as well as their inductive coupling to the magnetic field coil is problematic for $\tau_Q < 10$ms, as this is on the timescale of both the pulse width and the decay time of the oscillations in the field coil circuit.

5.2 Kibble-Zurek measurements

While the success in proving the existence of scaling of fluxon production with quench time is inarguable, there are still a lot of open questions relating to the formulation of Kibble-Zurek theory for annular Josephson junctions and the experimental conditions.

5.2.1 Josephson or superconducting phase transition

From the beginning, it was suggested that the phase transition in an annular Josephson junction should be described using the junction parameters, by identifying $\xi\ \lambda_J$ and $d\xi/dt\ \bar{c}$ when applying the fundamental Kibble-Zurek theory to the specific case of Josephson junctions[22]. However, the reasoning for this is somewhat vague, as it is hard to predict which will be the governing phase transition *a priori*; the superconducting phase transition of the rings or the Josephson phase transition of the full system. Luckily the predictions of scaling exponent, σ is different in the two cases, as described in Sec. 2.4, and so available for experimental testing. The results obtained in very detailed measurements of the scaling of defect production with quench time show clearly, that the scaling is incommensurate with the single superconducting ring prediction. The scaling exponent found is $\sigma_{AJTJ} = 0.51 \pm 5\%$, which seems to clearly rule out the superconducting phase transition as the origin of the produced flux, as this predicts $\sigma_{SC} = \frac{1}{4}$[5]. Looking beyond the difference in scaling exponent, another strong argument against the superconducting transition of the ring electrodes being the origin of the fluxons, comes from the identical results obtained for annular overlap junctions with one or two rings - the so-called JJ3 and JJ4 flavors. Within the uncertainty on the determination of the prefactor, a, in the scaling law $\bar{f_1} = a\tau_Q^{-sigma}$ there is no

difference between the two geometries. The statistical uncertainty on a is approximately 10%. If the origin of the fluxons was the superconducting phase transition in the ring electrodes, a clear difference between the two should be seen, as two identical rings should have twice the probability of generating a fluxon as a single ring. For large probabilities, multiple trappings might cancel, but at low probabilities this effect is insignificant, and a difference by a factor of two in a should be seen. All of these argue strongly against the superconducting phase transition as the origin of a fluxon production. With the Hindmarsh-Rajantie mechanism[25] and thermal gradient-induced production of fluxons[74] not applicable to annular metallic Josephson junctions, this leaves the Josephson transition as the only remaining origin. The Hindmarsh-Rajantie mechanism only applies to single superconducting rings and the thermal gradient-induced fluxon production is only possible in non-isotropic superconductors possesing d-wave symmetry.

The model for the Josephson phase transition giving a scaling exponent of $\sigma_{AJTJ} = \frac{1}{2}$ is somewhat weakly founded, and certainly the result of the experimental findings[34, 33]. For now it should be accepted as the best model, although a significant amount of work is necessary to test the assumptions of the model. The most important assumptions to be tested is the critical current density dependence on temperature close to T_c[35] and the Swihart velocity close to T_c[30]. Both of these assumptions are critical to the model giving the quoted scaling exponent, and should be given more experimental attention in the future. There is no reason to expect the assumptions to be invalid, but experimental evidence for them in the samples used for this work is scarce.

Insofar as one accepts the assumptions, the range in temperature across which the Swihart velocity is constant seems to be larger than the range probed by the $T(\bar{t})$ attained in this experiment. Otherwise, a change in slope is expected for small values of τ_Q.

5.2.2 Magnetic shielding

The best test of the magnetic shielding used in the setup comes from the single-ring SQUID experiment. In the SQUID experiment, the outer three layers of shielding (2 high-permeability shields and a Pb superconducting shield) were not present, but the inner shielding was identical. The offset from zero magnetic field was measured to be approximately 5nT, which corresponds to about $\Phi_0/3$ through a 500μm annulus. Comparing to the theory of Sec. 2.2.5 and the results in Fig. 4.6(a) Sec. 4.2, this can certainly cause a measurable change in the observed trapping probability in the standard 500μm ring experiment, and will have a large influence on rings of larger circumference. This is somewhat taken care of by using the trapping probability measured in the point of symmetry in the $\bar{f}_1(B)$ curve, which equivalent to measuring at point where the applied field cancels the transverse component of any fields close to the sample. The symmetry point offset measured using this method is of similar magnitude to the one reported in the SQUID experiments or smaller.

The in-plane field is assumed to be insignificant in relation to the production of defects. The offset measured in the SQUID setup varies between different coolings of the shields and the rotation with respect to their surroundings, but the variation is significantly smaller than the period of the SQUID signal. Therefore it is reasonable to expect, that the offset is less than Φ_0/A_{SQUID}.

In any case, the shielding used in the annular Josephson experiments is significantly better than the one measured in the SQUID experiment, because of the addition of another 3 shields. This indicates, that the residual (unshielded) magnetic field in the annular Josephson junction

experiment was small enough to be disregarded, at least when coupled with active compensation by application of a weak magnetic field transverse to the ring.

5.2.3 Magnetic field dependence of trapping

Two characteristic dependencies of single-flux trapping on applied transverse magnetic field during cooling have been predicted theoretically. One is for $N \to 1$, where N is the number of domains in the annulus. This results in a double-peak behavior with a minimum close to zero at zero field, and the maxima close to 100% at $B_1 = \pm\Phi_0/A_{ring}$. This is equivalent to what would be seen in an experiment investigating induced flux trapping by cooling a superconducting ring slowly through its phase transition temperature. This is exemplified very nicely by measurements shown in Fig. 4.6(a). The peak maxima are placed at approximately at $B = \pm 15$nT, which corresponds very well with the prediction of $B_1 = 15.7$nT for a 500μm ring as used in the measurements, which were done with $\tau_Q = 5$s.

The second type of characteristic dependence on transverse magnetic field is a single peak centered at zero applied field. The height of the maximum is always less than 50%. This is what is expected when the number of domains in the ring becomes large, which happens for fast quenches, $\tau_Q \to 0$ or large rings $C \gg \xi(\bar{t})$. An example of this behavior is seen in Fig. 4.6(b), which is superimposed with the theoretical curve for $N = 16$. The data is collected after quenches of $\tau_Q = 5$s on a 2000μm junction, which has the same electrical parameters as the 500μm junction used in the other example. For $N = 16$, the trapping probability should go to zero at approximately $\bar{n} = 4$, which corresponds to a field of $B_4 = \pm 4\Phi_0/A_{ring} \approx 4$nT, where the area of a ring with a circumference of 2000μm is used. This seems to be too low by a factor of approximately two, when comparing to the data.

According to the theory, the number of domains should be linearly dependent on circumference. Therefore, the change from $N = 1$ for a 500μm junction to $N = 16$ for a 2000μm junction is surprising. While it might be possible to find acceptable fits with the theoretical curves where N is somewhat less than 16, it is certainly larger than 4, as the curve for $N = 4$ has a clearly expressed minimum at zero field (see Fig. 2.4(a)). For N slightly smaller, the correspondence with the predicted width of the single peak would also be improved. None the less, the scaling with circumference in the magnetic field dependence of single-fluxon trapping seems to indicate, that the number of domains increases proportionally to C^2 rather than C. It is also worth noting, that for $N > 12$, increasing the number of domains actually reduces the probability of single fluxon trapping, as shown in Fig. 2.3. This is caused by an increase in probability of trapping more than one fluxon, which at $N = 16$ is already at approximately 8%.

5.2.4 Scaling with junction circumference

The only data on the scaling of fluxon production with circumference is the comparison of the 500μm junction data with that of the 1500μm. The τ_Q scaling is identical, but the prefactor, a, which contains the C dependence is higher for the 1500μm junction. Since all other parameters of the experiment are kept the same, the change in prefactor must be caused by the geometry change. The predicted change in a is an increase by a factor of three. However, the increase is only seen to be by a factor of $1.7 \pm 10\%$. From this single datapoint, it seems, that the scaling

with circumference is only approximately $\sqrt{C}$, which is clearly opposite to the C^2 indication of the B-field dependence.

However, single-fluxon production is only expected to scale linearly with circumference in the low-N limit. This can be seen in Fig. 2.3 on page 11. After the linear regime, the single-fluxon probability tops and then goes down again. Linear scaling in N is only predicted for the linear regime of $\bar{f}_1(N)$, $N \lesssim 6$. More measurements are certainly necessary to get a clear picture on the scaling of single-fluxon trapping with circumference and thereby N.

5.2.5 Uncorrelated trapping events

One of the central hypotheses of all Kibble-Zurek experiments is that defect production in one quench is completely uncorrelated to that of the next quench. As discussed by Bettencourt *et al* in [20] the maximum temperature of the system must be significantly above T_c for the memory of defects to be completely eradicated.

Applied to the annular junction measurements of this project, the correlation is between trappings in different quenches. Uncorrelated trapping events are equivalent to describing the trapping events by Poisson statistics. One test of whether the trapping events are well described by Poisson statistics is to examine the statistics of the event spacings, or interevent times. If the trapping events are uncorrelated, the probability of having an interevent time of t_i, $P(t_i = t)$, should follow the exponential dependence

$$P(t_i = t) \propto e^{-t/t_0} ,$$

where t_0 is dependent on the probability of trapping in a single event. Fig. 5.1 shows a typical histogram plot of the detected interevent times during a Kibble-Zurek measurement batch on a 500μm annular overlap Josephson junction. The fit is described in the inset, which results in $t_0 \approx 12.7$. The distribution is seen to be well fitted by an exponential, confirming the assumption of non-correlated trapping events. No batch used in the production of the data for Kibble-Zurek scaling exhibited non-exponental behavior in the interevent time distribution.

5.2.6 Experimental difficulties

The main experimental difficulties of the annular Josephson junction setup was related to shielding - both electrical and magnetic. The weak electrical noise from the input of the preamplifiers was surprisingly potent in disturbing the phase transition of the Josephson junctions. This was most likely caused by currents across the junction barrier, and made worse by the fact that the junction current distribution from an applied bias current is only approximately uniform in the Lyngby geometry[75] and certainly not uniform in the annular overlap geometry. The effect of not mechanically disconnecting the wires between the junction and the preamplifiers was invariably asymmetric voltage steps, significantly increased trapping probabilities and erratic response of the trapping probability to externally applied magnetic fields during the cooling.

The problem of magnetic shielding was also of great importance. It is an experimental fact, that the quality of obtained data in the form of IV curves for the junctions, was increased with each extra layer of shielding, even the fifth layer had noticeable impact. This is a bit surprising, as the initial shielding used was comparable to what is used in many SQUID experiments. The main

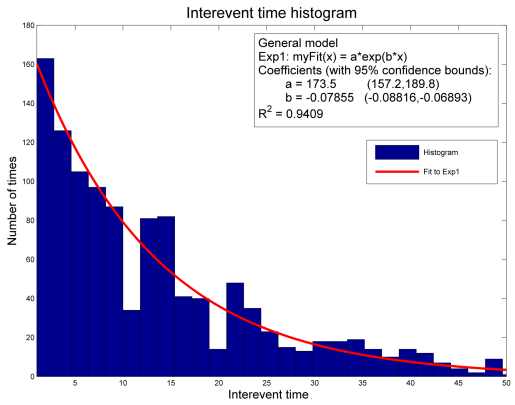

Figure 5.1: The probability of having N_{IE} quenches in a row without trapping plotted as a histogram for an example batch. An exponential decay is a signature that the trapping events follow a Poisson distribution, and therefore are uncorrelated.

reason is probably, that the junctions themselves are quite sensitive to static magnetic fields, and the phase transition is thought to be extremely sensitive to high-frequency magnetic noise. The shielding of static magnetic fields was probably acceptable using only a single high-permeability shield and a high-T_c superconducting shield, but high-frequency magnetic noise shielding is increased immensely by adding extra layers of superconducting shields. These tend to reduce AC magnetic fields even more strongly than static fields, as even the flux trapped in the shield during cool-down will be forced to be static by the superconducting area surrounding the trapped flux lines. Added shielding minimized the percentage of non-ideal voltage steps and the variation in the measured critical current.

Finally, the electrical heating was problematic. At first, simple pulse generators were used for generating the heat pulses, but it was found that replacing these by DC current supplies with mechanical relays increased data quality significantly. The most likely cause is inductive coupling of the magnetic field generated by minute currents in the resistive heaters to the superconducting annulus. These currents originate from the electrical noise in the pulse generator, as it is switched off electrically rather than mechanically. A similar problem was encountered when using the Ge resistive temperature sensor, which had to be mechanically disconnected during measurements. The disadvantage of using mechanical relays was their much slower response time, which limits the minimum pulse width and thereby minimum attainable quench time. This is a very limited problem because both thermal gradients and the change from second- to first-order transition happens just outside the range of quench times available using mechanically switched heating pulses.

5.3 Single ring setup with SQUID readout

The single superconducting ring experiment with SQUID readout is very similar to the experiment done in [10], although using faster quenches. The cited paper is focused mostly on ther-

mally activated fluxoid production, and uses a different superconductor to form the rings, which was chosen exactly for its sensitivity to thermal activation. As the experiments in the paper are also conducted on arrays of rings, the interplay between the rings may play an important role as well as the uncommented issue of thermal gradients. The data from that experiment might, however, be a good test of the Hindmarsh-Rajantie mechanism as it has some degree of spatial correlation information, that could be extracted.

For now, the initial results from the single ring experiment with SQUID readout show great promise. It has been demonstrated theoretically and experimentally verified, that the setup has the resolution necessary to detect single fluxoid production in the ring. Many samples with different ring sizes and even some squares, have been manufactured and awaits only measurements. The different shapes allow for using Zurek's idea that thermally activated and quench-induced flux trapping can be differentiated by looking at superconducting structures with different self-inductances but identical lengths. This is because thermal activation of flux production is dependent on the energy of a fluxoid in the system, which is dependent on the self-inductance. However, the difference in self-inductance between the rings and the squares might not be enough to discriminate.

The applications of the current setup to Kibble-Zurek measurements is limited at this stage, mostly because of unstable magnetic shielding. Moving it to the shielded environment used in the annular Josephson junction setup should improve this significantly. This work is already underway as well as a thorough characterization of the shielded environment by using the SQUID mounted inside. The noise of the SQUID system should also be improved significantly to allow for greater range of measurable fluxoid numbers within the one period of the SQUID, by allowing weaker coupling.

6 Conclusion

6.1 Production of topological defects in phase transitions

The main focus of this project has been on the design and use of new experimental methods for detecting Kibble-Zurek defect production in phase transitions of superconducting systems subjected to rapid cooling.

In the course of the project, a setup for detecting fluxons in annular Josephson junctions were designed and produced. The resulting system was characterized thermally by simulations and experiments and electrically in experiments. This setup has produced the so-far most convincing proof of defect production scaling with quench time in any solid-state experiment, as well as opened some new questions on the scaling of defect production with sample size and the dependence on external causes of symmetry breaking.

The detected single-defect production probability, $\bar{f}_1$, scales with a powerlaw dependence, $\bar{f}_1(\tau_Q) = a\tau_Q^{-\sigma}$, on the quench time, τ_Q. The scaling exponent is $\sigma_{AJTJ} = 0.52 \pm 5\%$ and the prefactor is $a_{500} = 0.01 \pm 10\%$ for 500μm junctions and $a_{1500} = 0.017$ for 1500μm junctions. The scaling is very robust, but the change in prefactor is below the theoretically expected change of a factor of three. It was found, that fluxon production in the 500μm annular overlap Josephson junctions depends on both the transverse and in-plane components with similar dependence, the transverse component being approximately an order of magnitude more potent in modulating the trapping probability.

A new theory extending Kibble-Zurek theory to systems with pre-broken symmetries has been developed, and the predictions tested experimentally. Good qualitative agreement was found, but experiments also indicate that refinement on the theory is necessary. The main questions relate to the scaling of defect production with sample size. This new theory is applicable to many systems, and not just the ones used in this project.

Another experimental setup was designed, produced and partly characterized. It is based on the application of well-known measurement techniques, such as laser interferometry and the optical lever method, to detecting nanometer deflections in a very soft silicon microcantilever. The small deflection of the microcantilever is caused by the magnetic dipole interaction of a magnetic fluxoid trapped in a superconducting ring on the cantilever with a generated magnetic field parallel to the cantilever. This setup should have a single-fluxoid resolution and a very wide range of detectable fluxoid numbers. For very large fluxoid numbers, should they be achieved, the applied actuation magnetic field can be reduced. This increases the range at the expense of resolution.

Finally, an experiment was implemented by a Master's student in the group, based on the samples designed for the microcantilever project, but with a SQUID readout. It was shown to have single-defect resolution and initial Kibble-Zurek measurements have been performed. They show scaling with a scaling exponent of $\sigma = -11$ based on three batches, but this is very likely caused by inadequate shielding and an immature experimental setup. While the Kibble-Zurek data of this experiment is not yet of acceptable quality, the calibration data proves the principle of the measurement setup.

6.2 Josephson junctions in magnetic fields

The other main contribution of this project was in the field of Josephson junctions and their interactions with externally applied magnetic fields. It was shown, that fields transverse to the barrier plane can have a modulating effect orders of magnitude larger than fields applied in the plane of the barrier. This effect was investigated for several different geometries and yielded new insight into an area largely ignored by the Josephson junction community. Because of the large effect of transverse fields, even slight misalignment of the field with the junction plane can generate enormous errors in the actual field present in the junction. Also, the effect of magnetic fields on SQUID Josephson junctions might be non-negligible in some cases, depending on the geometry. In addition to explaining experimental errors, this opens the opportunity to create superconducting circuits in which different parts of the circuit have different sensitivities to magnetic fields.

The effect of fields in directions between transverse and in-plane has been investigated, and for some geometries an almost total cancellation angle exists. At this angle, the effect of the transverse component almost completely cancels the effect of the in-plane field - leaving the junction insensitive to the applied field.

In a related experiment, the transverse magnetic field dependence dependence of the critical current in annular overlap junctions with fluxon(s) trapped was investigated. It was shown experimentally and numerically, that the shape of this dependence can be exploited to distinguish between fluxons and anti-fluxons.

6.3 Outlook

While already very successful the annular Josephson junction experiment still has a lot of interesting measurements available. The two most interesting experiments are (1)a thorough investigation of the dependence of fluxon production on circumference and (2)whether the field cancellation found in the dependence of the cold junction critical field on magnetic field direction exists also in fluxon production. The first experiment is important as the linear dependence of the number of domains, N, on circumference, C, is unanimously accepted. It would be a strong blow to the independent sector model, and indeed the whole Kibble-Zurek scenario if this was not the case. The second experiment is particularly important, as it would shed light on the ordering of the phase transitions. Field cancellation is an effect attributed to the existence of superconducting electrodes, and a similar cancellation effect at the same angle as a cold junction would indicate that the fluxon production happens at a time when the junction electrodes have well-expressed superconductivity. The similar relative strengths of the in-plane and transverse components of the magnetic fields found in modulation of the cold junction critical field and also in fluxon production in external fields certainly pose some interesting questions. An almost constant trapping probability as a function of applied field strength in a certain direction would be a strong indication of the electrodes superconductivity at the time of fluxon production.

The new single ring samples used in both the SQUID measurements and the soon-to-be realized microcantilever experiment allows for direct measurements of the thermal gradients on the sample shortly after the transition, and, by extrapolation, the gradients present during the transition. This makes fine-tuning of the heating parameters possible to minimize the thermal

gradients. However, it also allows testing of the predictions of [27] and [26] for trapping dependence on thermal gradients. The two cited papers do not agree to which extent defect production is suppressed by gradients in the temperature, and the result can be of fundamental importance. This effect has been qualitatively tested in [9], but no hard data has been published. Also, the available range of quench times in that experiment was limited, and statistics quite poor because of the dimensionality of the system.

The new single ring setup using mechanical readout, and to some extent also the SQUID readout experiment, has the potential to solve a lot of the experimental difficulties and ambiguities of the annular Josephson junction experiment. Samples are available in 125μm, 250μm, 500μm and 756μm varieties with both square and ring-geometries. This is ideal for testing defect production as a function of both self-inductance and system size. The electrical connections directly to the system undergoing the phase transition has always been problematic, and only through significant work shielding and mechanically disconnecting it during the transition was reliable data obtained. The new experiment(s) can use all of the gained knowledge in magnetic shielding and is free from problems with electrical connections. Thermal gradients can be directly measured using the Josephson junction thermometry design, that has shown impressive stability and precision in the annular Josephson junction experiments. Finally, it would be very interesting to see if in-plane magnetic fields has any effect at all on the single ring's fluxoid production in quenches.

Bibliography

[1] T.W.B. Kibble. Topology of cosmic domains and strings. *Journal of Physics A (Mathematical and General)*, 9(8):1387–98, 1976.

[2] NASA. Nasa wmap project website, wmap # 060915. http://wmap.gsfc.nasa.gov/, 2008.

[3] T.W.B. Kibble. Some implications of a cosmological phase transition. *Physics Reports*, 67(1):183–99, 1980.

[4] W.H. Zurek. Introduction. cosmology meets condensed matter. *Nature (London)*, 317:505, 1985.

[5] W.H. Zurek. Cosmological experiments in condensed matter systems. *Physics Reports*, 276(4):177–222, 1996.

[6] Isaac Chuang, Ruth Durrer, Neil Turok, and Bernard Yurke. Cosmology in the laboratory: Defect dynamics in liquid crystals. *Science*, 251(4999):1336–1342 and 2875529, 1991.

[7] P.C. Hendry, N.S. Lawson, R.A.M. Lee, P.V.E. McClintock, and C.D.H. Williams. Generation of defects in superfluid 4he as an analogue of the formation of cosmic strings. *Nature*, 368(6469):315–317, 1994.

[8] M.E. Dodd, P.C. Hendry, N.S. Lawson, P.V.E. McClintock, and C.D.H. Williams. Nonappearance of vortices in fast mechanical expansions of liquid 4he through the lambda transition. *Physical Review Letters*, 81(17):3703–3706, 1998.

[9] E. Polturak, A. Maniv, and G. Koren. Spontaneous generation of magnetic flux in superconductors: Testing the model. *Journal of Low Temperature Physics*, 2004.

[10] J R Kirtley, C C Tsuei, F Tafuri, P G Medaglia, P Orgiani, and G Balestrino. Superconducting quantum interference device microscopy of fluxoids in superconducting rings and artificially layered systems. *Superconductor Science and Technology*, 17(5):S217–S223, 2004.

[11] C. Bauerle, Yu.M. Bunkov, S.N. Fisher, H. Godfrin, and G.R. Pickett. Laboratory simulation of cosmic string formation in the early universe using superfluid 3he. *Nature*, 382(6589):332–334, 1996.

[12] V.M.H. Ruutu, V.B. Eltsov, A.J. Gill, T.W.B. Kibble, M. Krusius, Yu.G. Makhlin, B. Placais, G.E. Volovik, and W. Xu. Vortex formation in neutron-irradiated superfluid 3he as an analogue of cosmological defect formation. *Nature*, 382(6589):334–336, 1996.

[13] T.W.B. Kibble. Testing cosmological defect formation in the laboratory. *Physica C*, 369(1-4):87–92, 2002.

[14] G. R. Pickett and T.W.B. Kibble. Introduction. cosmology meets condensed matter. *Phil. Trans. Roy. Soc. A*, 366:2793–2802, 2008.

[15] D. I. Bradley, S. N. Fisher, A. M. Guénault, R. P. Haley, J. Kopu, H. Martin, G. R. Pickett, J. E. Roberts, and V. Tsepelin. Relic topological defects from brane annihilation simulated in superfluid 3he. *Nature Physics*, 4:46–49, 2008.

[16] S. Rudaz and A. M. Srivastava. On the production of flux vortices and magnetic monopoles in phase transitions. *Mod. Phys. Lett. A*, 8:1443, 1993.

[17] Levon Pogosian and Tanmay Vachaspati. Relaxing the geodesic rule in defect formation algorithms. *Physics Letters B*, 423(1-2):45–48, 1998.

[18] R. Monaco, M. Aaroe, R. Rivers, and J. Mygind. Spontaneous fluxon production in annular josephson tunnel junctions in the presence of a magnetic field. *Phys. Rev. B*, 77:054509, 2008.

[19] G. Karra and R. Rivers. Reexamination of quenches in he4 (and he3). *Phys. Rev. Lett.*, 81:3707–3710, 1998.

[20] L.M.A. Bettencourt, N.D. Antunes, and W.H. Zurek. Ginzburg regime and its effects on topological defect formation. *Phys. Rev. D*, 62:065005, 2000.

[21] R. Rivers. Private communication, 2008.

[22] E. Kavoussanaki, R. Monaco, and R.J. Rivers. Testing the kibble-zurek scenario with annular josephson tunnel junctions. *Physical Review Letters*, 85(16):3452–3455, 2000.

[23] R. Monaco, J. Mygind, and R. J. Rivers. Zurek-kibble domain structures: The dynamics of spontaneous vortex formation in annular josephson tunnel junctions. *Phys. Rev. Lett.*, 89(8):080603, Aug 2002.

[24] R. Monaco, J. Mygind, and R. J. Rivers. Spontaneous fluxon formation in annular josephson tunnel junctions. *Phys. Rev. B*, 67(10):104506, Mar 2003.

[25] M. Hindmarsh and A. Rajantie. Defect formation and local gauge invariance. *Phys. Rev. Lett.*, 85(22):4660–4663, Nov 2000.

[26] T.W.B. Kibble and G.E. Volovik. On phase ordering behind the propagating front of a second-order transition. *JETP Letters*, 65(1):102–107, 1997. arXiv:cond-mat/9612075v1.

[27] Jacek Dziarmaga, Pablo Laguna, and Wojciech H. Zurek. Symmetry breaking with a slant: Topological defects after an inhomogeneous quench. *Phys. Rev. Lett.*, 82(24):4749–4752, Jun 1999.

[28] L.P. Gor'kov. Microscopic derivations of the ginzburg-landau equations in the theory of superconductivity. *Zhurnal Eksperimental'noi i Teoreticheskoi Fiziki*, 36:1918–1923, 1959.

[29] M. Tinkham. *Introduction to superconductivity, 2nd Edition*. McGraw-Hill, 1996. ISBN: 0070648786.

[30] J.C. Swihart. Field solution for a thin-film super-conducting strip transmission line. *Journal of Applied Physics*, 32(3), 1961.

[31] M. Weihnacht. Influence of film thickness on d.c. josephson current. *Physica Status Solidi B*, 32:K169–72, 1969.

[32] V. Ambegaokar and A. Baratoff. Tunneling between superconductors. *Phys. Rev. Lett.*, 10(11):456–459, 1963.

[33] R. Monaco, M. Aaroe, J. Mygind, R. J. Rivers, and V. P. Koshelets. Experiments on spontaneous vortex formation in josephson tunnel junctions. *Physical Review B (Condensed Matter and Materials Physics)*, 74(14):144513, 2006.

[34] R. Monaco, J. Mygind, M. Aaroe, R. J. Rivers, and V. P. Koshelets. Zurek-kibble mechanism for the spontaneous vortex formation in nb-al/al[sub ox]/nb josephson tunnel junctions: New theory and experiment. *Physical Review Letters*, 96(18):180604, 2006.

[35] A. A. Golubov, E. P. Houwman, J. G. Gijsbertsen, V. M. Krasnov, J. Flokstra, H. Rogalla, and M. Yu. Kupriyanov. Proximity effect in superconductor-insulator-superconductor josephson tunnel junctions: Theory and experiment. *Phys. Rev. B*, 51(2):1073–1089, Jan 1995.

[36] B. D. JOSEPHSON. Coupled superconductors. *Rev. Mod. Phys.*, 36(1):216–220, Jan 1964.

[37] I. Rosenstein and J.T. Chen. Effect of transverse magnetic fields on dc josephson current. *Phys. Rev. Lett.*, 35(5), 1975.

[38] E.H. Brandt. Superconductors of finite thickness in a perpendicular magnetic field: strips and slabs. *Phys. Rev. B*, 54, 1996.

[39] A.F. Hebard and T.A. Fulton. Josephson junctions in transverse magnetic fields. *Phys. Rev. Lett.*, 35(19), 1975.

[40] R. Monaco, M. Aaroe, J. Mygind, and V.P. Koshelets. Planar josephson tunnel junctions in a transverse magnetic field. *J. Appl. Phys.*, 102(093911), 2007.

[41] R. Monaco, M. Aaroe, J. Mygind, and V.P. Koshelets. Static properties of small josephson tunnel junctions in a transverse magnetic field. *J. Appl. Phys.*, 104(023906), 2008.

[42] R. Monaco, M. Aaroe, V.P. Koshelets, and J. Mygind. Static properties of small josephson tunnel junctions in an oblique magnetic field. Accepted for publication in Phys. Rev. B in Mar. 2009. Available on arXiv in pre-print: http://arxiv.org/PS_cache/arxiv/pdf/0901/0901.2455v1.pdf, 2009.

[43] R.F. Broom. Some temperature-dependent properties of niobium tunnel junctions. *J. Appl. Phys.*, 47(12), 1976.

[44] M. Aaroe, R. Monaco, V. Koshelets, and J. Mygind. The effect of a close-fitting superconducting shield on the effective coil factor of a solenoid. To be submitted to SUperconductor Science and Technology, 2009.

[45] D.J. Thouless. Strong-coupling limit in the theory of superconductivity. *Physical Review*, 117:1256–60, 1960.

[46] Mads Rolf Kjær Jensen. Flux trapping in superconducting rings. Master's thesis, Technical University of Denmark, 2009.

[47] eFunda. Engineering fundamentals website. www.efunda.com, 2009.

[48] Charles Kittel. *Introduction to Solid State Physics, 7th ed.* John Wiley and sons Inc., 1996. ISBN: 0471111813.

[49] J.R. Waldram. The josephson effects in weakly coupled superconductors. *Reports on Progress in Physics*, 1976.

[50] Alwyn C. Scott, Flora Y. F. Chu, and Stanley A. Reible. Magnetic-flux propagation on a josephson transmission line. *Journal of Applied Physics*, 47(7):3272–3286, 1976.

[51] A. Barone and G. Paternó. *Physics and Applications of the Josephson Effect*. John Wiley and sons Inc., 1982. ISBN: 0471014699.

[52] A. Davidson, B. Dueholm, and N.F. Pedersen. Experiments on soliton motion in annular josephson junctions. *Journal of Applied Physics*, 60(4):1447–54, 1986.

[53] C. Nappi, R. Cristiano, and M.P. Lisiskii. Fiske steps in annular josephson junctions with trapped flux quanta. *Phys. Rev. B*, 58, 1998.

[54] T. Van Duzer. *Principles of superconductive circuits and devices*. Prentice Hall, 1998. ISBN: 0521624355.

[55] A.A. Golubov and A.V. Ustinov. Interaction energy of abrikosov and josephson vortices in a long josephson junction. *Physics Letters A*, 162:409–414, 1992.

[56] S.L. Miller, K.R. Biagi, J.R. Clem, and D.K. Finnemore. *Phys. Rev. B*, 31(5), 1985.

[57] M. Gurvitch, M.A. Washington, and H.A. Huggins. High quality refractory josephson tunnel junctions utilizing thin aluminum layers. *Appl. Phys. Lett.*, 42:472–474, 1983.

[58] V.P. Koshelets. Private communication, 2008.

[59] R. Monaco, G. Costabile, and N. Martucciello. Influence of the idle region on the dynamic properties of window josephson tunnel junctions. *J. Appl. Phys.*, 77:2073–2080, 1995.

[60] A. I. Gubin, K. S. Il'in, S. A. Vitusevich, M. Siegel, and N. Klein. Dependence of magnetic penetration depth on the thickness of superconducting nb thin films. *Phys. Rev. B*, 72(6):064503, Aug 2005.

[61] V.N. Gubankov, M.P. Lisitskii, I.L. Serpuchenko, F.N. Sklokin, and M.V. Fistul. Influence of trapped abrikosov vortices on the critical current of the josephson tunnel junction. *Superconductor Science and Technology*, 1992.

[62] T. A. Fulton and L. N. Dunkleberger. Lifetime of the zero-voltage state in josephson tunnel junctions. *Phys. Rev. B*, 9(11):4760–4768, Jun 1974.

[63] Dong Ho Kim, B.Y. Kim, J.H. Kang, and T.S. Hahn. Magnetic field effect on the escape rate in nb/alox/nb josephson junctions. *Cryogenics*, 45(1):35 – 39, 2005. 1st Asian Conference on Applied Superconductivity and Cyrogenics (ASAC 2003).

[64] Nuno D. Antunes, Pedro Gandra, and Ray J. Rivers. Is domain formation decided before or after the transition? *Physical Review D (Particles, Fields, Gravitation, and Cosmology)*, 73(12):125003, 2006.

[65] G. Binnig, C. F. Quate, and Ch. Gerber. Atomic force microscope. *Phys. Rev. Lett.*, 56(9):930–933, Mar 1986.

[66] G. Binnig, Ch. Gerber, E. Stoll, T. R. Albrecht, and C. F. Quate. Atomic resolution with atomic force microscope. *EPL (Europhysics Letters)*, 3(12):1281–1286, 1987.

[67] J. J. Sáenz, N. García, P. Grütter, E. Meyer, H. Heinzelmann, R. Wiesendanger, L. Rosenthaler, H. R. Hidber, and H.-J. Güntherodt. Observation of magnetic forces by the atomic force microscope. *Journal of Applied Physics*, 62(10):p4293 –, 19871115.

[68] Viggo Tvergaard. *Styrkelære: Statik og bjælketeori*. Technical University of Denmark, 1998.

[69] J.P. Gilles, S. Megherbi, G. Raynaud, F. Parrain, H. Mathias, X. Leroux, and A. Bosseboef. Scanning electron microscope for vacuum quality factor measurement of small-size mems resonators. *Sensors and Actuators A*, 145-146:187–193, 2008.

[70] Mads Laursen and Johan Grundtvig. Optical detection of cantilever deflection. Bachelor's thesis, DTU Physics, 2008.

[71] T.R. Albrecht, P. Grütter, D. Rugar, and D.P.E. Smith. Low-temperature force microscope with all-fiber interferometer. *Ultramicroscopy*, 42-44(Part 2):1638 – 1646, 1992.

[72] Y.-I. Lee, K.-H. Park, J. Lee, C.-S. Lee, H.J. Yoo, C.-J. Kim, and Y.-S. Yoon. Dry release for surface micromachining with hf vapor-phase etching. *Microelectromechanical Systems, Journal of*, 6(3):226–233, Sep 1997.

[73] J. Borrill, T.W.B. Kibble, T. Vachaspati, and A. Vilenkin. Defect production in slow first-order phase transitions. *Phys. Rev. D*, 52:1934, 1995.

[74] Ariel Maniv, Emil Polturak, Gad Koren, Yuri Bliokh, Björn Biehler, Bernd-Uwe Runge, Paul Leiderer, Boris Shapiro, and Irena Shapiro. Observation of a new mechanism of spontaneous generation of magnetic flux in a superconductor. *Physical Review Letters*, 94(24):247005, 2005.

[75] M.R. Samuelsen. Bias current distribution in the lyngby josephson junction geometry. Internal reference, DTU Physics, 1990.

List of Figures

A Equipment and maintenance

A.1 Experimental checklist

The complete guide to performing and experiment is given in the Word document Docs/Experiment Checklist.doc on the Data CD. In particular, the different cable connections are listed, and the differences between the *TEST* and *MEASURE* procedures are specified.

A.2 Equipment

This is a complete list of the hardware used in the setup:

```
Function generator: Exact Model 126 VCF/SWEEP GENERATOR
HP Triple output DC power supply: E3631A
HP DAQ/Switch Unit, 34970A
Tektronix analogue Oscilloscope rack 7613 (storage)
  70A22 Differential amplifier
  70A22 Differential amplifier
Tektronix analogue Oscilloscope rack 7603
  70A22 Differential amplifier
  70A22 Differential amplifier
  7B87 Time base
Tektronix TDS 410A Digitizing oscilloscope
  ADA400A Differential Preamplifier
  ADA400A Differential Preamplifier
HP 34401A Multimeter
HAMEG rack
  HM8040-2 Triple power supply
  HM8040-2 Triple power supply
Tektronix TM503A Amplifier Rack
  AM502 Differential Ampl
  AM502 Differential Ampl
  AM502 Differential Ampl
Dell Dimension 4600
  Pentium 4, 2.80GHz
  512 MB RAM
  Microsoft Windows XP Pro SP2
  National Instruments LabVIEW Express 7.0
  NI PCI-GPIB
  NI PCI-6023E DAQ card
  NI PCI-6733 DAQ card
```

In figure A.1 the cryoprobe is seen, and an illustration shows the connectors to the electronics box on top.

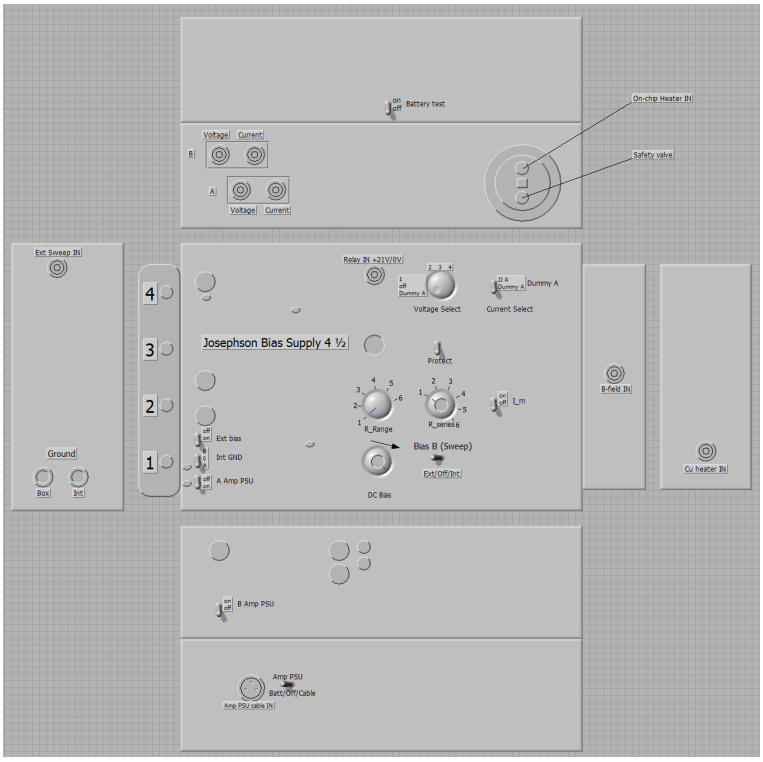

(a) The cryoprobe electronics box connectors.

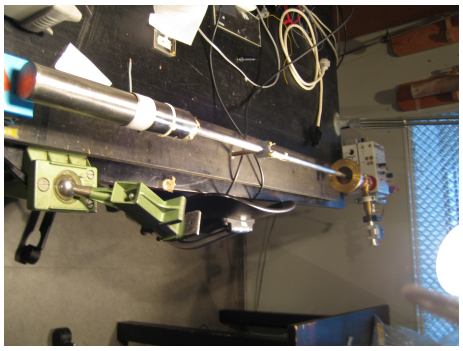

(b) Photo of cryoprobe on its stand.

(c) Closeup of sample holder.

Figure A.1: The cryoprobe with closeup of sample holder and schematic of electronics box connectors and switches

A.3 Workflows/maintenance

A.3.1 Changing sample

In order to change sample, follow these instructions:

- First put the cryoprobe on its horizontal stand, as seen in A.1(b).
- Release the cone by loosening the perpendicular screw fixing it to the cryoprobe tube
- Slide cone towards electronics box to reveal the 3 vacuum shield parallel screws.
- If not already at room temperature, wait until it is. Release vacuum from inside the shield.
- Unfasten the 3 screws, and remove the 3 bronze fasteners on the side.
- **Carefully** rotate the vacuum shield with the Pb shield until it lets go of the top flange.
- Drag it carefully downwards, removing any vacuum grease there might be.
- Remove it completely and put it in a secure place. Take care not to damage wires in the process.
- Remove the free cryoperm shield and the superconducting shield inside it.
- Remove solenoid, by first disconnecting the wires to it, and then sliding it down.
- Disconnect all connectors to the sample holder, and unscrew it from the SMA cable mounting.
- Mount it in an upright position, PCB insert facing up, in a rubber-padded vice.
- Release PCB insert by removing the 4 screws holding it down - store them in a secure place.
- Move it upwards, very carefully to avoid scratching sample surface
- Leave it hanging by the teflon insulators very carefully to avoid wire damage.
- Remove the plastic frame - the sample will usually stick to it.
- Open the sample box from IREE and replace the sample to its proper place.
- Take new sample and put on the small elevated Cu rectangle

When remounting the PCB insert, it is important to visually inspect the positioning of the fingers with respect to the contact pads. When it is time to reattach the vacuum shield, remember to fill the cavity in the top flange with vacuum grease, and to only attach the fasteners and screws tight enough to avoid it falling off. Afterward pump out the vacuum compartment with the vacuum pump to let the vacuum shield slide correctly into place, and then fasten the screws as much as possible without damaging the screws - use small screw-driver to avoid applying too much force.

A.3.2 Replacing wires

When replacing wires, it might be necessary to remove and re-solder all wires in the same teflon tube. If that is the case, prepare the desired number of $80\mu m$ wires of identical length in advance. Before soldering, de-insulate the ends by presoldering with fresh, very hot (350 degrees celsius) solder to the ends, one at a time. Reset soldering iron temperature to 260-300 degrees Celsius, and presolder contact positions as well. Before soldering on to contacts, twist all wires thoroughly (or use pre-twisted wires), and put them through the teflon tube. Be careful only to push, and not pull it through, as this can easily break the wires in the middle, leaving you with the same problem you started out with. When soldering, thermally unload the wire by using flat pliers close to the soldering point. This is to avoid heating the contact positions too much.

For checking connections a low-current multimeter can be used (most multimeters with range setting should be fine, if set to the range $1 - 10k\Omega$), as long as no current is passed through any junction. Make sure you have the right layout of the sample for checking this! Check the connections all the way into the electronics box and verify the color coding still holds according to the diagrams in the following section and figure A.2. After changing wires always test the entire setup by attaching a 10Ω resistance dummy at the end of the cryoprobe.

A.3.3 Connector overview and diagrams

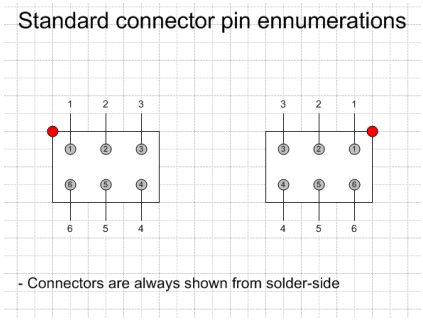

(a) The standard connector numbering scheme.

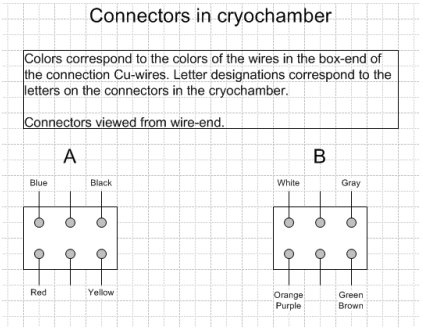

(b) Insert connectors.

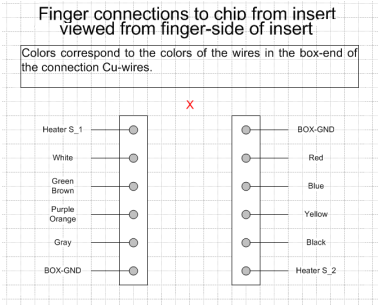

(c) Insert connections

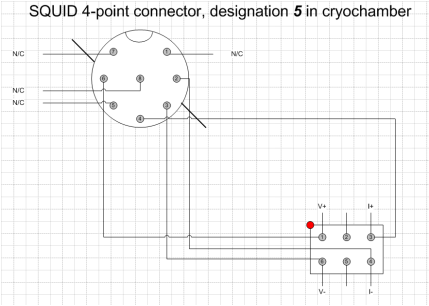

(d) Thermometer/SQUID connector

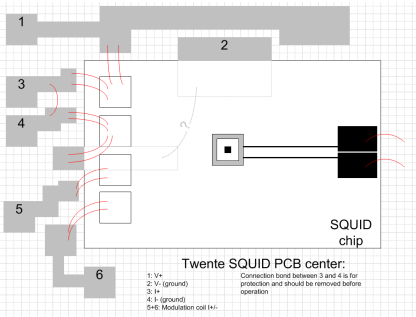

(e) SQUID chip mount layout

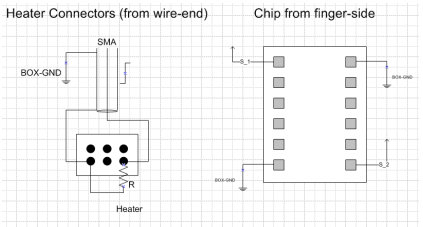

(f) Heater connections

Figure A.2: Overview of connectors in the cryoprobe

Figure B.1 shows the sample layouts used in the Kibble-Zurek part of the project.

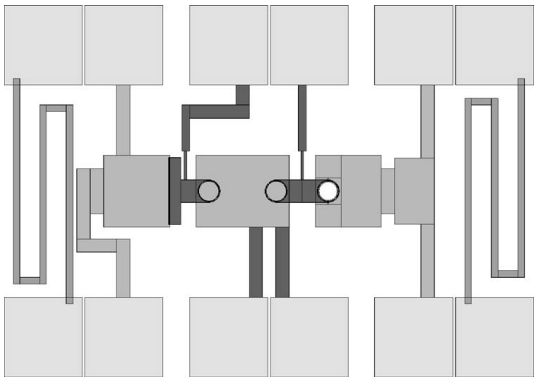

(a) Sample for Kibble-Zurek measurements on annular overlap junctions. From the left to the right, one long linear overlap, two JJ3 and one JJ4 type junctions are seen[33].

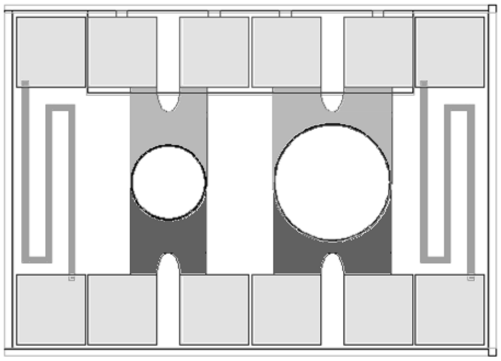

(b) Sample for Kibble-Zurek measurements on Lyngby junctions. 1000μm and 2000μm circumferences.

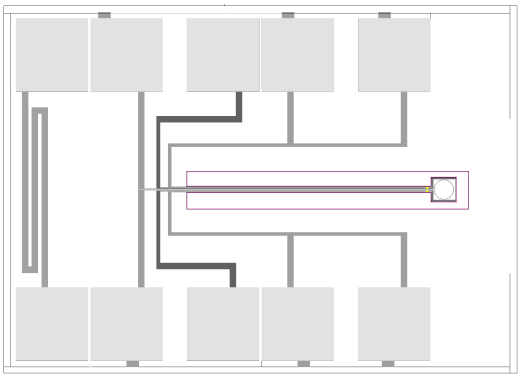

(c) Sample for Kibble-Zurek measurements on single ringe. The four cross junctions used as thermometers are placed on the island around the ring. This sample layout was used for the single ring SQUID measurements.

Figure B.1: The different samples used in the project.

C.1 Matlab analysis files

This appendix contains a list of useful m-scripts and VIs.
Matlab scripts:

- *analyzeFile.m*(file, GainI, GainV) - 'file' is filename of CSV file containing data. Gain* are for scaling.
  Analyzes and plots a single cycle.
- *getTauQQ.m*(file, stopindex, pulsewidth, offset) - 'file' is filename of CSV file containing data from oscilloscope, 'stopindex' is used to crop the end of the file, 'pulsewidth' is the length of the heating pulse in *ms* and 'offset' is the voltage offset in μV.
  Finds τ_Q from gap voltage time series.
- *QofT.m*(list, intervalLength, column) - plots the maximum, the mean and their fraction of 'list'(column), using an interval of *'x ±' intervalLength*'.
  Used to create Q(t) plots.
- *Rob2.m*(startfile, endfile, exclusions, OffsetV) - analyzes files in the interval (['startfile','endfile'] NOT 'exclusions'). The output is of type 'list' used in other m-scripts.
  Used for calculating trapping frequencies.
- *RobHistogramNoTrapping.m*(list, column, divisions) - plots the IcHistogram of list(column) using 'divisions' number of bins.
  Used to create IcHistogram plots.
- *RobPlot.m*(list, plot1st, plot2nd, plot3rd, plotGood) - Plots the desired subgroup of cycles contained in 'list'.
- *timePlot.m*(listfile) - Creates timeplot from listfile.

C.2 LabVIEW VIs

- *cyclemag-copy2.vi* - Controls the setup timing parameters and data acquisition.
- *IcVsB.vi* - Complete system for controlling and plotting the full magnetic field dependence of a particular junction. Each junction is subjected to the full range of available magnetic fields in a plane defined by the two field coils.
- *I-V_scroll.vi* - Used for quick plotting of binary datafiles.

C.3 Experimental report template

The experimental report template is a MS Word document, found in *Docs/Template.doc* on the data CD.

D Detailed derivations

D.1 Standard Kibble-Zurek derivation

This derivation follows the derivation in [3, 22] closely, but elaborates on certain points.

Assume that the equilibrium correlation length diverges at $T = T_c$ as

$$\xi_a(t) = \xi_0 \left| 1 - \frac{T}{T_c} \right|^{-\nu} = \xi_0 \left| \frac{t}{\tau_Q} \right|^{-\nu} , \tag{D.1}$$

and that the relaxation time diverges as

$$\tau(t) = \tau_0 \left| 1 - \frac{T}{T_c} \right|^{-\gamma} = \tau_0 \left| \frac{t}{\tau_Q} \right|^{-\gamma} . \tag{D.2}$$

This is done as an expansion around $T = T_c$, so that $T(t) \approx T_c(1 - \frac{t}{\tau_Q})$, which also defines of τ_Q as

$$\frac{dT}{dt}|_{T=T_c} = -\frac{T_c}{\tau_Q} . \tag{D.3}$$

The phase ordering velocity is approximated as the average velocity for a fluctuation growing from zero to ξ_a

$$\bar{c}(t) = \frac{\xi_a(t)}{\tau(t)} = \frac{\xi_0}{\tau_0} \left| \frac{t}{\tau_Q} \right|^{-\nu+\gamma} . \tag{D.4}$$

From formula D.1 one can find $\dot{\xi}_a(t)$ by standard differentiation and obtain

$$\dot{\xi}_a(t) = \xi_0 \nu \tau_Q^{\nu} |t|^{-\nu-1} . \tag{D.5}$$

Equating this with the expression found in D.4 and solving for t one obtains

$$\bar{t} = \pm (\tau_0 \nu)^{\frac{1}{\gamma+1}} \tau_Q^{\frac{\gamma}{\gamma+1}} , \tag{D.6}$$

where t has been renamed $\bar{t}$ to show, that this is the specific time, at which $\bar{c}(T(t)) = \dot{\xi}_a(T(t))$. By Kibble and Zurek's second assumption, the scale of defect separation will then be

$$\bar{\xi} = \xi_a(\bar{t}) = \xi_0 \left| \nu \tau_0 \tau_Q \right|^{-\frac{\nu}{\gamma+1}} . \tag{D.7}$$

D.2 Torque on superconducting ring with trapped fluxoid subjected to in-plane magnetic field

According to [54](p. 115, Eq. (14)), the inductance of a superconducting thin film loop is

$$L_0 = \mu_0 r\left[\ln\left(\frac{16r}{w}\right) - 2\right] , \tag{D.8}$$

where r is the radius of the loop and w is the width of the wire. The circulating current equivalent to one flux quantum trapped in the ring can be found from

$$I_0 = \frac{\Phi_0}{L_0} = \frac{h}{2e}\frac{1}{\mu_0 r\left[\ln\left(\frac{16r}{w}\right) - 2\right]} \approx 5\mu A . \tag{D.9}$$

The magnetic dipole moment is given by

$$m = I_0 \pi r^2 \approx 1.0 \times 10^{-13}\mathrm{Am}^2 . \tag{D.10}$$

Finally, the torque is given by

$$\tau = m \cdot B_a , \tag{D.11}$$

which for a realistic magnetic field strength of 3mT equals 3.1×10^{-16}Nm. The maximum deflection of a cantilever under an end-moment load, τ, is[68]

$$d_{max} = \frac{\tau l_c^2}{2EI_A} , \tag{D.12}$$

where l_c is the cantilever length, E is the elastic modulus of the cantilever material, and I_A is the area moment of inertia of the cantilever cross section. For a rectangular cross section, this is

$$I_A = \frac{1}{12}\left(w_c t_c^3\right) , \tag{D.13}$$

where w_c and t_c is the width and thickness of the cantilever respectively. For $w_c = 50\mu$m and $t_c = 1\mu$m, the area moment of inertia is $I_A = 4.2 \times 10^{-24}\mathrm{m}^4$. For a silicon cantilever of length 2000μm, the end result is

$$d_{max} = \frac{6\tau l_c^2}{E_{Si}\left(w_c t_c^3\right)} \approx 1.3\mathrm{nm} . \tag{D.14}$$

To find the minimum length required for a maximum deflection of 1nm, Eq. (D.14) can be solved for l_c yielding

$$l_c = \sqrt{\frac{2d_{max}E_{Si}I_A}{\tau}} \approx 1.75\mathrm{mm} . \tag{D.15}$$

Here, the parameters used are the same as for the calculation of d_{max} for a 2000μm cantilever.

E Demonstrations

E.1 Symmetry breaking when freezing water

This is meant as a quick demonstration of the effect of cooling rate on a well-known phase transition, the freezing of water. Although it is an extreme first order phase transition, it will still show some of the qualities expressed by the Kibble-Zurek phase transition.

E.1.1 Equipment needed

- Liquid nitrogen in open styrofoam container
- Metal tube, approximately 3cm in diameter 40cm in length
- Rubber plugs for the tube.
- Freezer or cold weather - a place with a temperature slightly below 0^{o}C
- Deionized/distilled water

E.1.2 Experimental procedure

- On the day before you need it for demonstration almost fill the metal tube with deionized water (leave 10% of the length for expansion) and close it with the rubber plugs.
- Put it in the freezer and leave it over night - the closer to the freezing point it is, the better your results
- On the next day take out the stick of ice from the tube and wrap it in a plastic bag. It should be very transparent. Put it back in the freezer
- Fill the metal tube with deionized water again and close it with the plugs. Make sure they are tight as liquid water in liquid nitrogen is a **BAD** idea!
- Put it vertically 90% into a styrofoam container with liquid nitrogen and wait for 5-10 minutes
- Take out the frozen stick of ice. It should be almost completely opaque and milky white.

E.1.3 Images from an experiment

In Fig. E.1 the result of a slow cooling of deionized water, in a temperature slightly below the freezing point over 15 hours, is shown. The resulting ice is clear except in the center, that probably was the last liquid part in the tube. The reason for the opaqueness here is likely up-concentration of tiny contaminants.

In Fig. E.2 the result of a fast cooling of deionized water in the same metal tube, over af few minutes, is shown. The ice is now completely opaque except for the outer few millimeters, which has been thawn and frozen again during handling.

(a) Slowly cooled ice.

(b) With a different background.

(c) Close-up.

Figure E.1: Photographs of the freezer-cooled sample

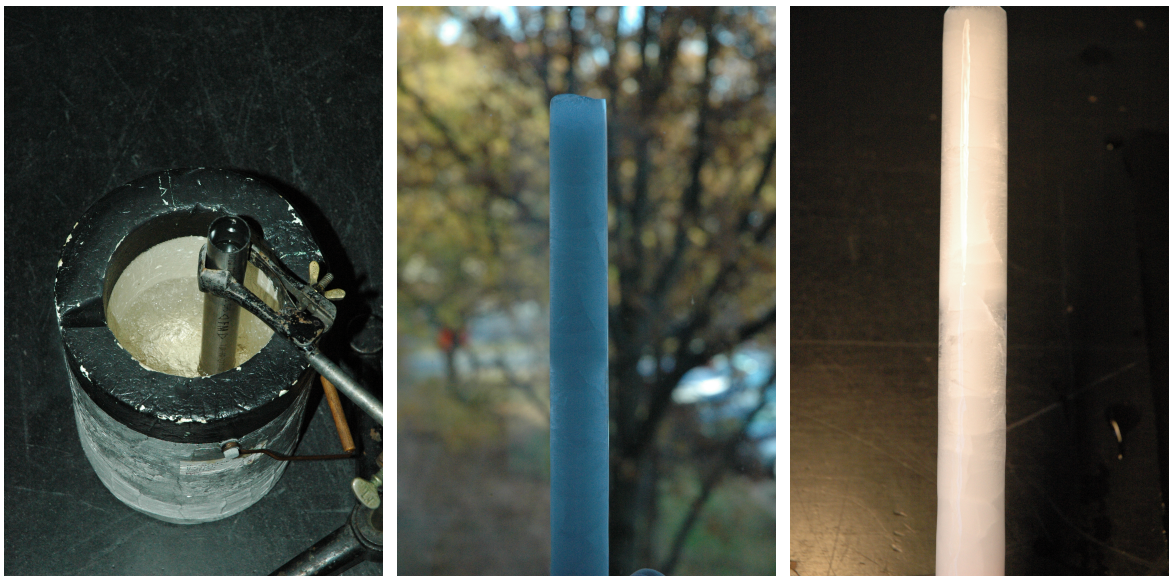

(a) Setup used for cooling in liquid nitrogen

(b) Quickly frozen ice

(c) In a different setting

Figure E.2: Photographs of the LN_2-cooled sample and the setup

E.1.4 Interpretation and analogue to the Kibble-Zurek mechanism

At the heart of the Kibble-Zurek mechanism lies the frustration of the degenerate ground phase caused by the system being unable to equilibrate in the time allowed for the transition. In the freezing of water, something similar happens although the reasons for the limitation is completely different. For the water freezing, the latent heat released in the freezing process must be transferred away from any growing ice crystals. Thereby, the heat transfer limits the growth of the crystals. Even if the heat conductance on the volume borders was infinite, the finite heat conductance of the water itself would limit the growth.

If the freezing is performed very slowly, there is ample time for this heat to be transferred away from the first crystal starting to grow. Therefore it can grow at the speed defined by how much energy is removed from the surface of the water volume. If energy is removed very quickly from the surface of the water volume, the heat transfer away from the single ice crystal is not enough to keep up, and so more crystals form. When the small crystals form they form with random lattice orientations, which means that when they meet, they can't fuse perfectly and lattice defects are created in the fused crystal. In water ice, the lattice defects tend to scatter light, and if enough of them exist, the ice will look opaque.

Although the limitation in the Kibble-Zurek scenario is the speed of information and the equilibrium domain growth velocity, the qualitative behavior is similar. Actually, the first experiments in a Kibble-Zurek context was done on liquid crystals - in a phase transition that was also first order. The heat transfer problem was handled by using a 2D geometry, where the heat could be taken out perpendicularly to the system.

E.2 Speed of information among students

This little demonstration was thought up to illustrate the concept of finite information velocity to students at a students' night at DTU Physics. It is a game with very simple rules.

E.2.1 Rules

- Each student is handed two cards - a red and a yellow one
- The **objective** for the students is to agree on a color as fast as possible
- Students are only allowed to communicate with their neighbors in all directions
- Time is limited by the presenter (me!)
- The game is run at least twice with significantly different times. Students tend to get better the second time around, so this should be factored in
- At the end of the allotted time, the presenter stops everyone and asks them to hold their chosen card in the air

(a) After a 30 second round.

(b) After a 10 second round.

Figure E.3: The students' choice of color after two different rounds of the game

E.2.2 Results

In Fig. E.3 two photographs of the final state of the students are shown. One is for a relatively long time, and one is for a rather short time. The number of students present in the room was approximately 70.

E.2.3 Interpretation

Unsurprisingly, the results show, that the longer the students are allowed to communicate the closer to agreement they get. It is seen that for the shorter time, a few smaller clusters exist, while for the long round time they have disappeared. It is a reasonable assumption, that the students start out with a random distribution of color selections (at least for the first round). Once the round starts, they try to convince their neighbors that their color is the right one. If the majority of their neighbors have another color, they will probably change their mind. Thus smaller clusters of color will tend to be swallowed up by larger ones. When two large clusters meet the boundary will be quite hard to move as nobody knows anything beyond what their neighbors tell them, and for students at the border, it will be approximately 50/50.

This kind of stability and the change with round time is a fairly good qualitative illustration of the limiting factors in a phase transition into two degenerate ground states - a red and a yellow one.

F Superconducting coil in shield

A quantitative investigation of the effect of a close-fitting superconducting shield on the coil-factor of a solenoid

M. Aaroe,[1] R. Monaco,[2] V.P. Koshelets,[3] and J. Mygind[1]

[1]*DTU Physics, B309, Technical University of Denmark, DK-2800 Lyngby, Denmark**
[2]*Istituto di Cibernetica del CNR, 80078, Pozzuoli, Italy and Unità INFM Dipartimento di Fisica, Università di Salerno, 84081 Baronissi, Italy*†
[3]*Institute of Radio Engineering and Electronics, Russian Academy of Science, Mokhovaya 11, B7, 125009, Moscow, Russia*

(Dated: January 22, 2009)

Superconducting shields are commonly used to suppress external magnetic interference. We show, that an error of almost an order of magnitude can occur in the coil-factor in realistic configurations of the solenoid and the shield. The reason is that the coil-factor is determined by not only the geometry of the solenoid, but also the nearby magnetic environment. This has important consequences for many cryogenic experiments involving magnetic fields such as the determination of the parameters of Josephson junctions, as well as other superconducting devices. It is proposed to solve the problem by inserting a thin sheet of high-permeability material, and the result numerically tested.

PACS numbers: 07.55.Nk, 85.25.Cp, 41.20.Gz

Many experiments characterizing superconductors and superconducting devices involve applying a magnetic field. One typical class of such experiments is the characterization of Josephson junctions[1].

Superconducting shields are unsurpassed to prevent extraneous AC and DC magnetic fields, e.g., high frequency magnetic noise and the Earth's magnetic field, from affecting magnetically delicate cryogenic instruments and experiments. However, in order to measure the magnetic properties of specimens in such setups, one has to mount one or more solenoids inside the shield. Often the trade off between demands for homogeneous fields and limited space places the coil in close vicinity of the shield. It is not surprising[2] - but often forgotten - that a shield which is close-fitting around the coil may strongly deform the magnetic field lines and thus change the coil factor, C.

It is common practice to use a Hall probe at room temperature to calibrate coils for magnetic measurements, even when the coils are to be used in a cryogenic environment[3]. From this calibration it is possible to determine the coil factor, C, relating the DC coil current, I_{coil}, to the B-field, B_i in the center of the solenoid

$$B_i = CI_{coil} \ .$$

The problem arises when the coil is subsequentially enclosed in a superconducting magnetic shield. For an ideal high-permeability shield, with $\mu_r \to \infty$, the problem does not arise, as the effect of the magnetically soft shield is to create a virtual, free space for the field lines.

First we consider the case of the infinite solenoid in free space and then compare to an infinite solenoid in an infinite, cylindrical superconducting shield. In free space, the internal field of the solenoid can be determined directly from simple, proven theoretical expressions. If Ampere's Law is integrated along loop number 2 in Fig. 1, it can be seen that the field outside the infinite solenoid, B_{ext}, in free space is everywhere zero, as it must be zero at $r \to \infty$. Similarly, for loop number 1, the field must be constant everywhere inside the volume enclosed by the solenoid.

If we now apply Ampere's Law to loop 3 in the figure, it can be seen that the field inside the solenoid, B_i, is given by

$$B_i = -B_{ext} + \mu_0 \lambda \ , \qquad (1)$$

where λ is the current density (per unit length) of the coil. Equation (1) is valid regardless of the presence of a superconducting shield on the outside.

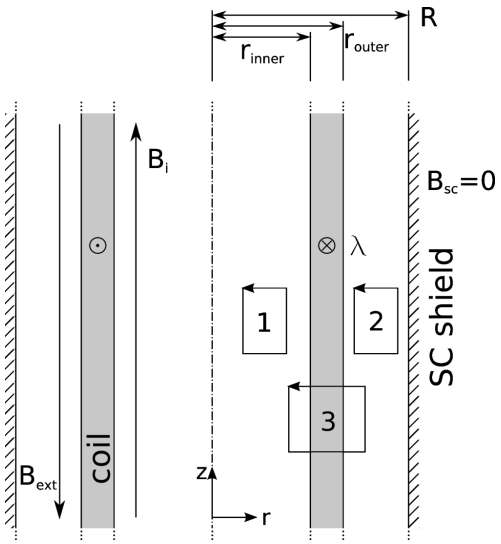

FIG. 1: Illustration for the calculation of magnetic fields for infinite solenoid in an infinite cylindrical superconducting shield.

For the infinite solenoid inside a superconducting shield

we simply note, that $B_{ext} > 0$ for a close-fitting superconducting shield ($\Delta r = R - r_{coil} \ll r_{coil}$), . This is because the field lines must close on themselves, and now have a limited volume in which to do so. Enclosing an infinite solenoid in a close-fitting ideal superconducting shield ($B_{SC} = 0$) increases B_{ext}, while the field inside the solenoid is reduced. Flux conservation gives

$$A_{ext}B_{ext} = A_{int}B_i \ , \tag{2}$$

where the areas A_{ext} and A_{int} are the cross-sectional areas, between the coil and shield and inside the coil, respectively. From Eqs. (1) and (2) we find

$$\frac{B_i}{B_{i0}} = \frac{R^2 - r_{coil}^2}{R^2} = 1 - \left(\frac{r_{coil}}{R}\right)^2 \ , \tag{3}$$

if the width of the coil is negligible. Eq. (3) has been normalized to the free space value, $B_{i0} = \mu_0\lambda$.

Using Comsol Multiphysics[4] finite-element magnetostatic simulations, the effect of enclosing a finite solenoid with a fixed I_{coil} in a superconducting shield has been investigated. The coil has the parameters $(r_{inner}, r_{outer}, h) = (15\text{mm}, 18\text{mm}, 50\text{mm})$, where h is the height (see Fig. 2). The distance between the end of the coil and the bottom of the superconducting shield can is denoted Δh. Furthermore, the current, I_{coil}, is DC, which implies a uniform current density in the coil cross-section.

The problem is axisymmetric, and the boundary conditions are set to magnetic insulation on the boundary of the superconducting shield. In principle, the shield top should be open, but the simulation is faster, and the difference in the result is within the error of the simulation, by setting the top boundary condition to magnetic insulation as well. The reason is, of course, that it is sufficiently far away, that only a negligible portion of the magnetic field lines would go in this area, even if it was open. The meshing was done automatically, and increasing the mesh density did not alter results.

The geometry used in the simulation is shown in Fig. 2. The magnetic field lines are drawn on top of the geometry. The maximum value of the field is located approximately at the same position, regardless of tje coil's position in relation to the shield.

The results of simulations for a large number of geometries are shown in Fig. 3. The plot shows the maximum value of the magnetic field strength inside the coil as a function of the bottom distance, Δh, and the radial distance, $\Delta r = R - r_{outer}$, between the solenoid and the superconducting shield.

The results show a strong influence of the superconducting shield on the generated magnetic field strength. In fact, a radial spacing between the solenoid and the superconducting shield of around $2r_{coil}$ is needed to reach

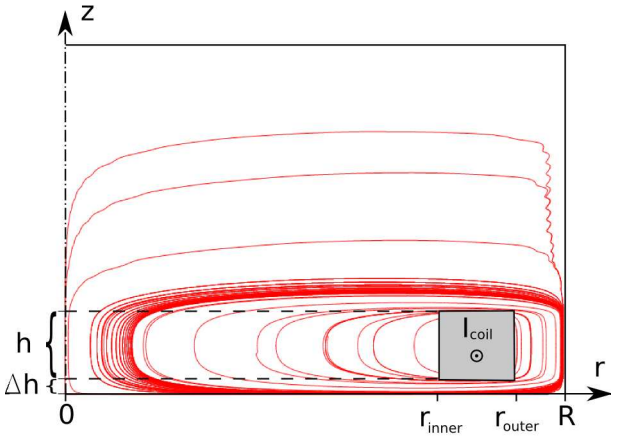

FIG. 2: (Color online) Graphical output of a typical simulation. The magnetic field lines are drawn on top of the geometry. Note that in this figure, the z-scale is very compressed compared to the r-scale ($h = 50$mm, $R = 20$mm). Numerical errors introduced by the fieldline algorithm are the cause of the small-lengthscale oscillations of the fieldlines in the top, far right.

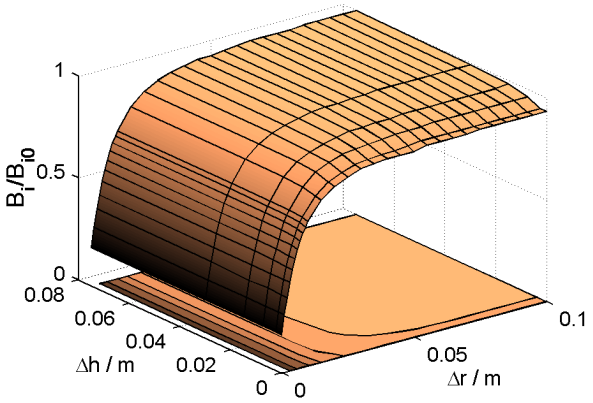

FIG. 3: (Color online) Plot of the magnetic field in the centre of the solenoid normalized to the free space value as a function ofthe distance to the bottom, Δh, and radial distance to the superconducting shield, $\Delta r = R - r_{outer}$. The colored plane below the surface is a filled contourplot, which illustrates the shape. The lines in the countourplot represent the numeric solution to the equation $B_i(\Delta h, \Delta r) = c$ where c is different for each line.

90% of B_{i0}.The deciding factor appears to be the radial distance, Δr, as even a rather large Δh only gives a 10% increase in field. The effect is larger for larger Δr.

The results show a very weak dependence on Δh and thus we should expect good agreement with the theoretical expression in Eq. (3). For fitting purposes, an additional parameter, α, is introduced to deal with the solenoid being finite, and the nearby capped end of the shield:

$$\frac{B_i}{B_0} = \alpha \frac{R^2 - r_{coil}^2}{R^2} \ . \qquad (4)$$

Fig. 4 is a comparison of Eq. (4) and the simulation output for one value of Δh. The fitting parameters are r_{coil} and the value of α, and the best fit is found for $(r_{coil}, \alpha) = (14\text{mm}, 0.94)$. Considering the crudeness of the model the fit is acceptable. It also produces a reasonable value for r_{coil}. The main effect of the cap on the closer end of the shield is to slightly change the limiting value for $R \to \infty$, and thus $\alpha < 1$, as seen in Fig. 3.

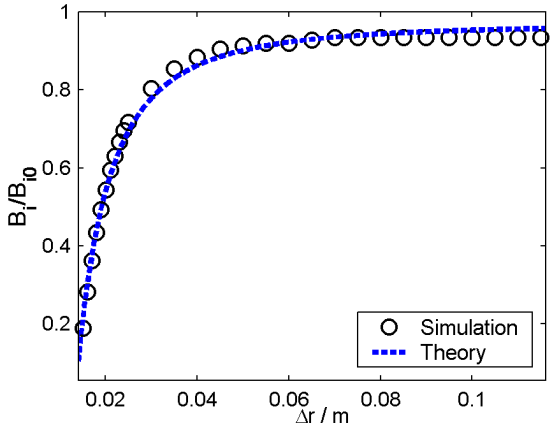

FIG. 4: Comparison between a fit of the theoretical expression Eq. (4) and the simulation output for $\Delta h = 2.5$cm. This fit gives $r_{coil} = 14$mm and $\alpha = 0.94$.

The effect of a high-permeability shield inside the superconducting shield is similar to inserting a large virtual volume of magnetic vacuum. The virtual volume is a factor of μ_r thicker than the actual shielding material, and should thus mediate the effect of confinement by the superconducting shield. The high-permeability sheet has been modeled as a cylinder with $\mu_r = 75000$, which is the stated value for Cryoperm[5] 10® typically used for cryogenic shielding. The result of inserting a 1mm thick cylinder between the solenoid and the superconducting shield is a full recovery of the of the coil factor to the value obtained for $R \gg r_{coil}$. Also, with the cylinder inserted, B_i is insensitive to the value of R. This is reasonable, as 1mm of high-permeability metal with $\mu_r = 75000$ should be roughly equivalent to 75m of vacuum between the solenoid and the superconducting shield.

The field strength outside the solenoid can exceed the field strength inside, when Δr is very small compared to r_{coil}. This means, that the critical field of the superconducting shield might be reached before expected. This may introduce hysteresis into measurements as well as large trapped magnetic fields. This can also be countered by the use of a cryoperm sheet.

In this paper we have presented a commonly overlooked source of systematic error in cryogenic setups involving magnetic fields. It was shown, that systematic errors in the coil factor of at least an order of magitude can be realised in setups with radial shield distance $\Delta r \ll r_{coil}$, when comparing to a simple Hall-probe measurement coil factor or standard free-space formulae. Furthermore, an approximate theoretical expression was derived for estimating the real magnetic field or coil factor inside a solenoid enclosed in a superconducting shield.

The most important parameter is the radial distance between the solenoid and the shield. The dependence on the distance from the coil to the shield in the axial direction is very weak - even to the limit of very small values of Δh. The solution is to either make ample space around the coil inside the superconducting shield or insert a high-permeability metal sheet between the coil and the superconducting shield. The effect of the sheet is effectively to insert a virtual vacuum for the magnetic field lines to close in, thus screening the coil from the effect of confinement. In any case, this shows the importance of calibrating the solenoid *in situ*. *In situ* calibration can be done using a SQUID magnetometer, without a high-permeability metal shield, if the maximum attainable field in the solenoid is not the limiting factor.

* Electronic address: aaroe@fysik.dtu.dk
† Electronic address: roberto@sa.infn.it

[1] R. Broom, J. Appl. Phys. **47** (1976).
[2] S. Pourrahimi, J. Williams, W. Punchard, J. Tuttle, M. DiPirro, E. Canavan, and P. Shirron, Cryogenics **48**, 253 (2008).
[3] J. Rowell, Phys. Rev. Lett. **11** (1963).
[4] www.comsol.com
[5] Manufactured by Vacuumschmelze Gmbh., datasheet at http://www.amuneal.com/pages/pdf/AmunealDataSheet2.pdf

G Amplifierbox layout

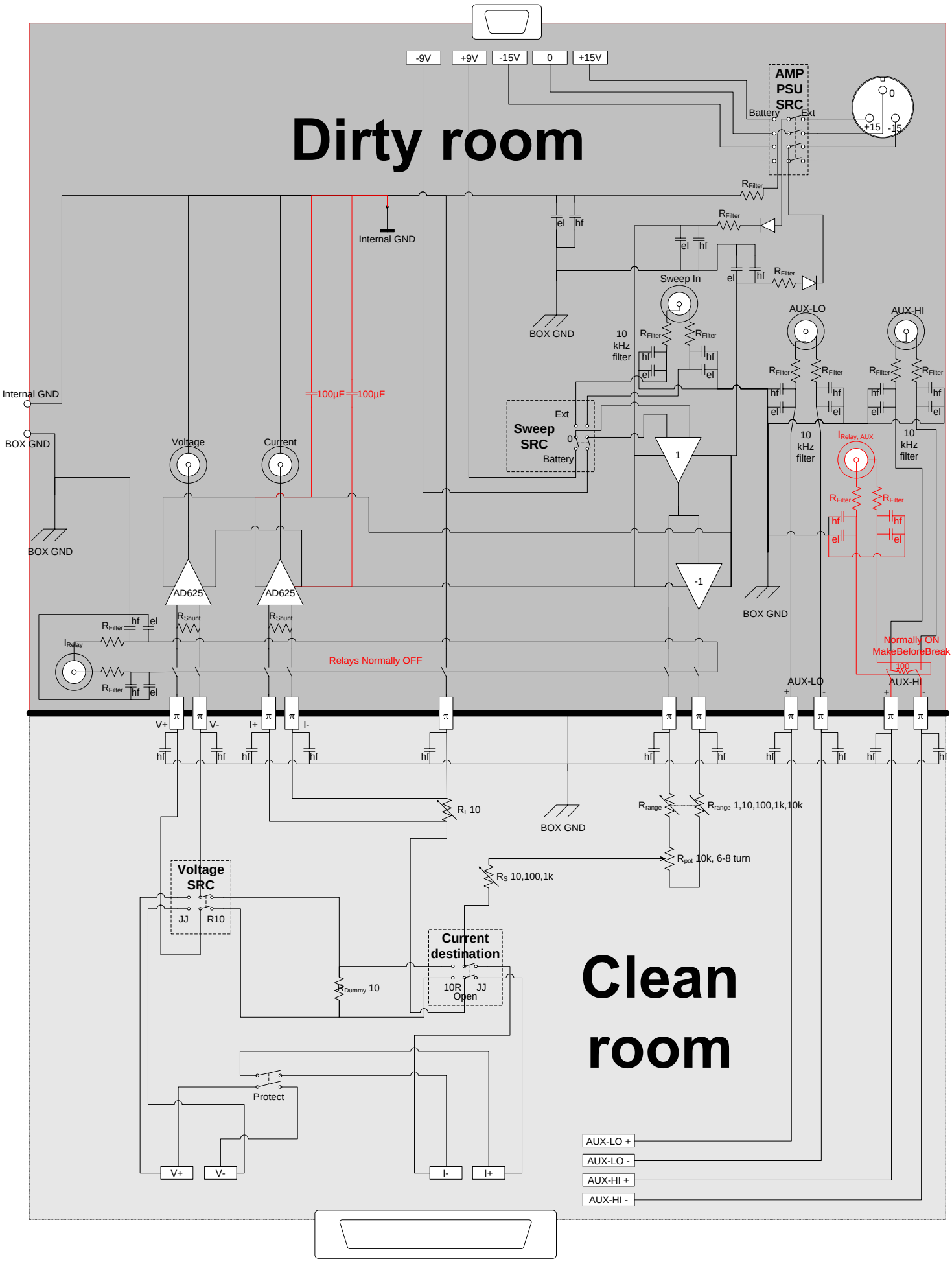
Dirty room
-9V
+9V
-15V
0
+15V
AMP PSU SRC
Battery
Ext
0
+15
-15
Internal GND
BOX GND
100µF
100µF
Voltage
Current
Sweep In
Sweep SRC
Ext
0
Battery
1
-1
AUX-LO
AUX-HI
10 kHz filter
AD625
AD625
Relays Normally OFF
Normally ON
MakeBeforeBreak
100
V+
V-
I+
I-
Ri 10
Rrange 1,10,100,1k,10k
Rpot 10k, 6-8 turn
RS 10,100,1k
Voltage SRC
JJ
R10
Current destination
10R
JJ
Open
RDummy 10
Protect
Clean room
AUX-LO +
AUX-LO -
AUX-HI +
AUX-HI -